

Phase Field Modeling of Fracture: Fatigue and Anisotropic Fracture Resistance

Dem Fachbereich Maschinenbau und Verfahrenstechnik
der Technischen Universität Kaiserslautern
zur Verleihung des akademischen Grades
Doktor-Ingenieur (Dr.-Ing.)
genehmigte Dissertation

von
M.Eng. Christoph Schreiber
aus Kelheim

Hauptreferent: Prof. Dr.-Ing. Ralf Müller
Korreferenten: Prof. Dr.-Ing. Kristin de Payrebrune
Prof. Tarek I. Zohdi
Vorsitzender: Prof. Dr.-Ing. Jan C. Aurich
Dekan: Prof. Dr.-Ing. Tilmann Beck

Tag der Einreichung: 10.05.2021
Tag der mündlichen Prüfung: 05.10.2021

Kaiserslautern, 2021

Herausgeber

Lehrstuhl für Technische Mechanik
Technische Universität Kaiserslautern
Gottlieb-Daimler-Straße
Postfach 3049
67653 Kaiserslautern

© Christoph Schreiber

Ich danke der „Prof. Dr. Hans Georg und Liselotte Hahn Stiftung“ für die finanzielle Unterstützung bei der Drucklegung

Druck

Technische Universität Kaiserslautern
Hauptabteilung 5 – Bau-Technik-Energie
Foto-Repro-Druck

Alle Rechte vorbehalten, auch das des auszugsweisen Nachdrucks, der auszugsweisen oder vollständigen Wiedergabe (Photographie, Mikroskopie), der Speicherung in Datenverarbeitungsanlagen und das der Übersetzung

ISBN 978-3-942695-22-0

Vorwort

Die vorliegende Arbeit entstand während meiner Beschäftigung als wissenschaftlicher Mitarbeiter am Lehrstuhl für Technische Mechanik der Technischen Universität Kaiserslautern.

Mein besonderer Dank gilt Herrn Prof. Dr.-Ing. Ralf Müller für die in jeder Hinsicht hervorragende Betreuung. Vielen Dank für die immer sehr hilfreichen Ratschläge und Einschätzungen, die Motivation neue Wege zu gehen sowie den großen Freiraum um eigene Ideen einzubringen und zu verfolgen.

Herrn Prof. Dr.-Ing. Jan C. Aurich danke ich für die Übernahme des Vorsitzes der Prüfungskommission sowie für die Leitung des DFG Projekts IRTG2057.

Frau Prof. Dr.-Ing. Kristin de Payrebrune danke ich für das Interesse an meiner wissenschaftlichen Arbeit und die Übernahme des Korreferates. Herrn Prof. Tarek I. Zohdi danke ich für die Unterstützung während meines Forschungsaufenthaltes im CMMR Lab der UC Berkely sowie für die Übernahme des Korreferates.

Allen Kolleginnen und Kollegen am LTM danke ich herzlich für die gute Zusammenarbeit, das großartige Lehrstuhlklima und die zahlreichen belebenden Diskussionen in den Pausen. Besonders möchte ich mich bei Frau Dr.-Ing. Charlotte Kuhn bedanken für die vielen konstruktiven fachlichen Diskussionen sowie Ihre Ratschläge bei komplexen Problemstellungen.

Frau Julia Hettesheimer und Herrn Dr.-Ing. Christian Sator danke ich für die stets angenehme personelle Führung und die Unterstützung bei zahlreichen organisatorischen Angelegenheiten. Herrn Tim Ettrich danke ich für seine studentische Arbeit.

Ich danke meiner Ehefrau Sabrina für ihr Verständnis, ihre Geduld und ihre mentale Unterstützung während dieses besonderen Lebensabschnitts.

Pfeffenhausen, Oktober 2021

Christoph Schreiber

Kurzfassung

In dieser Arbeit wird ein Ansatz zur Simulation von Initiierung und Wachstum von Rissen in spröden Materialien, basierend auf diffusen Grenzflächen, um seinen Anwendungsbereich erweitert. Durch die Ergänzung der inneren Energie eines bestehenden Phasenfeldmodells um einen zusätzlichen Anteil wird das Beschreiben von Ermüdungsrisswachstum ermöglicht. Außerdem wird durch das Modifizieren des Gradienten des Phasenfeldparameters in der regularisierten Rissenergie erreicht, dass das entstehende Modell anisotropes Risswachstum abbilden kann.

Einleitend werden die benötigten Grundlagen aus verschiedenen Feldern der Mechanik beschrieben sowie die Phasenfeld Methode zur Simulation von Risswachstum eingeführt. Danach werden die Modifikationen, welche im Rahmen dieser Arbeit eingebracht wurden begründet. Es wird im Weiteren detailliert beschrieben, wie die entsprechenden Erweiterungen eingearbeitet wurden und die Evolutionsgleichungen der neuen Phasenfeldmodelle, in Form von Ginzburg-Landau Gleichungen werden hergeleitet.

Das resultierende gekoppelte Differentialgleichungssystem wurde, unter Verwendung von impliziter Zeitintegration, als ebenes nichtlineares Finite Elemente Problem implementiert. Die starke als auch die schwache Form der beschreibenden Gleichungen des Phasenfeld Modells werden beschrieben.

Verschiedene Test Szenarien wurden simuliert, um zu Untersuchen inwieweit reale Ergebnisse mit dem Modell erzielt werden können. Die Ergebnisse zeigen, dass Brüche in anisotropen Medien beschrieben werden können. Außerdem erzielt das entwickelte Ermüdungsmodell reales Verhalten für wichtige Größen wie die Risswachstumsgeschwindigkeit und Phänomene wie Mittelspannungseinfluss oder Reihenfolge Einflüsse werden korrekt abgebildet. Simulationsergebnisse von beiden Modellen werden mit experimentellen Ergebnissen verglichen, wobei eine gute Übereinstimmung nachgewiesen werden kann.

Abstract

Within this thesis, a diffuse interface approach for the simulation of crack nucleation and growth in brittle materials is enhanced to enlarge its scope. Incorporating an additional energy contribution in the total energy functional of an existing phase field model enables the handling of fatigue crack growth. In another approach, anisotropic brittle fracture is studied by a modification of the spatial gradient in the regularized crack energy.

At first, the necessary basics from different fields of mechanics and also for the phase field method, a method to simulate phase transformations by means of an auxiliary parameter, are provided. Subsequently, the work gives an outline of the basic motivation for the performed modifications. It is described how the new features are incorporated. Appropriate evolution equations in terms of Ginzburg-Landau type equations for the new phase field models are then derived in a detailed way.

The coupled systems of the phase field models are implemented in a nonlinear finite element formulation, where implicit time integration is employed. The strong and also the weak forms of the governing equations corresponding to the developed models are presented.

Several test cases are simulated in order to investigate the accuracy of the developed models. These studies illustrate, that the novel phase field frameworks are able to predict cracking in media that reveal an anisotropic fracture toughness. Furthermore, the fatigue model accurately predicts important quantities like the crack growth speed. Also phenomena like mean stress or sequence effects are fully covered by the formulation. Simulation results from both phase field models are compared with experimental findings and reveal good agreement.

Contents

1	Introduction	1
1.1	Motivation and Background	1
1.2	Objectives and Overview	3
2	Relevant Basics of Mechanics	5
2.1	Continuum Mechanics	5
2.1.1	Kinematics	5
2.1.2	Deformation	6
2.1.3	Stress	7
2.1.4	Force Balance	8
2.1.5	Small Deformations	9
2.1.6	Constitutive Law	10
2.2	Fracture Mechanics	11
2.2.1	Crack Opening Modes	12
2.2.2	Process Zone and K-concept	12
2.2.3	Griffith Theory and J-integral	14
2.3	Fatigue of Materials and Structures	16
2.3.1	General Description of the Phenomenon	16
2.3.2	Total Life Approach	18
2.3.3	Fatigue Crack Growth	19
3	Phase Field Modeling of Fracture	21
3.1	General Remarks on Phase Field Modeling	21
3.1.1	Evolution of Phase Transformations	23
3.1.2	Generalization of Ginzburg-Landau Equation	25
3.2	Free Energy Potential for Fracture	28
3.2.1	The Variational Model of Brittle Fracture	28
3.2.2	Regularization of Free Energy	31
3.3	Phase field Modeling of Brittle Fracture	33
3.3.1	The Kuhn-Müller Phase Field Model	34
3.3.2	Alternative Models and Extensions	38
4	Modifications of the Phase Field Model for Brittle Fracture	41
4.1	Cracking of Materials with Anisotropic Fracture Resistance	42
4.1.1	Characterization of Crack Deflection	42
4.1.2	Basic Modification	44
4.1.3	Analytic Investigation and Parameter Identification	47
4.2	Phase Field Model for Fatigue Crack Growth	52
4.2.1	Review of Phase Field Models for Fatigue	53
4.2.2	Interpretation of Order Parameter	54

4.2.3	Modification of Driving Force Mechanism	55
4.2.4	Characteristic Driving Stress Quantity	61
4.2.5	Cycle Resolved Simulation Scheme	62
4.2.6	Variation of Mean Stress and Stress Ratio	63
5	Finite Element Implementation	65
5.1	Spatial Discretization of Governing Equations	65
5.1.1	Weak Forms	65
5.1.2	Isoparametric Concept	67
5.1.3	Numerical Quadrature	69
5.1.4	Spatial Discretization	69
5.2	Solution of the Nonlinear System and Time Integration	72
5.2.1	General Solution Procedure	72
5.2.2	Derivation of Associated System Matrix	73
5.2.3	Irreversibility Constraint	76
6	Simulation of Complex Fracture Problems	77
6.1	Verification of the Phase Field Model for Anisotropic Fracture Toughness	78
6.1.1	Basic Effects of the Modification	78
6.1.2	Assessment of Crack Deflection	82
6.1.3	Validation by Experimental Results	89
6.2	Verification of the Phase Field Model for Fatigue Crack Growth	93
6.2.1	Characterization of Fatigue Crack Growth Behavior	94
6.2.2	Effect of Load Sequence and Mean Load	102
6.2.3	Mixed mode Loading	104
7	Conclusion and Outlook	109
	Bibliography	113

Chapter 1

Introduction

1.1 Motivation and Background

Materials fail if they are exposed to an arbitrary high load. There is no serious reason to doubt this statement. The term material is in this context not restricted to typical construction materials like metals or synthetic materials. It also includes solids from our natural environment as e.g. minerals, crystals, or bone. However, it is to discuss how exactly this failure appears and how to characterize it. Failure simply means in this context, that an external load can not be transmitted through the material as it is in the initial state since the material has undergone a process of separation. The complete or partial separation of a connected continuum is referred to as fracture. Today our complete life is organized by the reliability of technical structures. Whether it is a toothbrush or a jet plane we use it in confident hope, that it will not break. Therefore, within engineering a major issue is to develop technical components in consideration of potential fractures. In this context it is not solely relevant to avoid cracking under certain loads but it may also be in the focus to precisely model the fracture process. An example may be the fail safe principle in designing, where the design is mainly shaped such that in case of failure the structure reaction causes minimal harm regarding a certain instance as e.g. people or relevant equipment. This illustrates the significance of research within this field. The different properties of fracture need to be understood in order to be properly integrated in development processes.

The basics of the research field, which is today referred to as fracture mechanics is provided by the work of A. A. Griffith, 1921, who proposed an energy consideration of the problem. In the sense of the first principle of thermodynamics, energies associated with the fracture process, as for instance chemical energies or the energy for plastic deformation in the close vicinity of a crack tip, need to be considered. The main approach is to summarize all these energies and express them by means of the crack surface area. Accordingly, Griffith invented a novel crack energy density. Furthermore, he proposed an energetic criterion to predict under which load a crack will propagate. The criterion, which is today referred to as Griffith's theory, basically assumes that a crack will propagate, once the associated increase of the just introduced crack energy will be balanced by the release of potential energy. As elegant such an energy criterion may be, it will be illustrated in chapter 3 that the applicability is strongly restricted. Therefore, the foundations for a more practical approach were laid by G. R. Irwin, 1957. Within this work the stress field near a crack tip is characterized under the assumption of linear elastic material behavior. Furthermore, he showed that the proportionality factors associated with a concrete crack problem can be set in relation to the energy approach from Griffith. This stress based concept is referred

to as K-concept and finds wide application in engineering and even within numerical investigation this concept is integrated.

The basic K-concept is, however, not capable of predicting the direction of crack extension for a combination of several crack opening modes to describe arbitrary load cases. Different approaches were proposed with focus on the prediction of the deflection direction. Most established in this regard are the Maximum Energy Release Rate criterion proposed by Wu, 1978, the Maximum Tangential Stress criterion from Erdogan and Sih, 1963 or the principle of local symmetry established by Goldstein and Salganik, 1974. However, all these approaches lack in the ability to predict crack nucleation.

In order to provide a comprehensive description of the fracture problem, which is capable of handling crack initiation as well as to predict the crack path, Francfort and Marigo, 1998 published a variational formulation. This theory is based on global energy minimization as a well known and commonly applied postulate. In this regard, this framework can be considered a generalization of Griffith's theory. The variational formulation provides a general tool. It lacks, however, in its applicability as the minimization can hardly be performed for arbitrary cases. The formulation from Francfort and Marigo, 1998 however provides the basis for a powerful numerical tool, namely the phase field fracture model. The unique character of this field is not the usage of computational assistance to the fracture problem. This was done numerous times by means of the finite element method, a method to solve partial differential equations as for instance those from a structure mechanical problem, numerically (see e.g. Bathe, 1996; Wriggers, 2001; Zienkiewicz and Taylor, 2001). The outstanding feature of the phase field framework is the incorporation of an additional degree of freedom in order to describe the state of relevant physical phases. A diffuse transition of this so-called phase field parameter eliminates discontinuities of sharp interfaces within the discretization. Accordingly, no mesh disconnection, element deletion or remeshing is necessary. However, a very relevant parameter in this context is the length scale, which determines the width of the transition zone between the phases. The application of the general framework is multiple in physics. Within fracture the different phases are intact material and broken material. A fracture phase field model for quasi static brittle fracture was proposed by Kuhn and Müller, 2010. Interestingly, the so called property of Γ convergence was proven for the free energy potential used within this work. In principle terms, this theory states that if the regularization length parameter goes to zero, the solution of the regularized model is the solution of the real problem. The evolution equation for the phase field parameter is based on a regularization (Bourdin et al., 2000) for the variation formulation from Francfort and Marigo, 1998. This evolution equation is coupled to linear elastic field equations of the structure mechanical problem. Thus the model is able to picture all aspects of brittle fracture. Alternative phase field models for brittle fracture were proposed by Borden et al., 2014 and Miehe et al., 2010b.

Within a large number of practical applications the complexity of specific fracture problems is way beyond the characteristic of quasi static brittle fracture. This applies to the material on one hand and the characteristics of the applied load on the other hand. Thus a variety of different phase field fracture models concerned with specific types of fracture were proposed in the last decade. For a number of materials the simplification of brittle fracture is not accurate as the plastic zone is significant and may not be neglected. Accordingly models for ductile fracture were studied by Borden et al., 2016 Miehe et al., 2016, Kuhn et al., 2016 or Aldakheel et al., 2018a. The phase field model from Schlüter et

al., 2014 considers a dynamic setup as for some applications inertia effects as well influence the fracture process.

1.2 Objectives and Overview

The present work introduces two additional phase field models, that deal with relevant phenomena of fracture, namely the effect of directionality of a material's fracture toughness as well as the extensive field of fatigue crack growth. Both models are extensions of the basic model for brittle fracture from Kuhn and Müller, 2010. The free energy density function is enhanced in order to adequately represent crucial properties from the investigated phenomena. The particular modifications apply to different items of the basic energy functional.

For the model covering the effects of an anisotropic fracture toughness, the critical point is to mimic the cracking behavior if in addition to the critical energy release rate is a function of the crack deflection angle. In order to account for this additional feature, the regularization of the crack energy density is realized. In detail only the non local part of this energy contribution is modified. This contribution is proportional to the spatial gradient of the phase field order parameter. Due to the direction dependence it appears reasonable to weight the gradient components properly.

A completely different modification is necessary in order to account for the complex phenomenon of cyclic fatigue. The difficulty lies in the magnitude of the loads causing a fracture. As the fatigue process initiates at load levels far below the static design limit an additional energy contribution is incorporated within the free energy functional. Another issue of the fatigue phenomenon is the very high numbers of load cycles, which are to be applied before cracking occurs. A straightforward simulation of every cycle is simply nonfunctional as this will blow up the computational effort. The simulation scheme must accordingly be transferred into the cycle domain.

In detail several approaches for the precise modeling of the different characteristics are analyzed in this work. The final model equations are introduced, fully described, and discretized by means of finite elements. The respective finite element implementation is also presented completely. It is the final objective of the present work to illustrate the accuracy of the introduced phase field models in an adequate way. Therefore, several numerical investigations were performed. The respective setups are described and important results are illustrated. In the case of the static anisotropic model it is mainly focused on the resulting crack path, which varies as respective parameters are adjusted. For the fatigue model the relevant crack growth rates are also evaluated as this is a very crucial point in terms of fatigue crack growth.

The present work is divided into seven chapters. The subsequent chapter aims to provide a brief summary of the relevant fundamental laws and concepts in continuum mechanics, fracture mechanics, and also in fatigue of materials.

Chapter 3 outlines the framework of phase field modeling of fracture. It begins with a brief overview of the phase field method from a general perspective. Characteristic benefits of the method are illustrated and a number of applications are introduced. The general

evolution equation for phase transformations, namely the Ginzburg-Landau equation is introduced and by the theory of a micro force balance proposed by Gurtin, 1996 it is illustrated how the equation can be generalized so it may be applied to the fracture problem. Subsequently, as the basic concept for the proposed phase field models the variational formulation of brittle fracture from Francfort and Marigo, 1998 is introduced and it is illustrated how this theory was regularized by Bourdin et al., 2000 in order to provide access for computational usage. Finally, the basic phase field model for brittle fracture from Kuhn and Müller, 2010 is introduced and relevant characteristics are discussed.

The subsequent three chapters deal with the scientific contribution of the present work. Chapter 4 deals with the entire theory regarding the two proposed phase field models of the present work. Relevant contributions from the literature are reviewed and after a clear motivation for the modifications the respective equations are derived and phase field models are explained comprehensively. Different possible concepts are introduced and it is argued why the particular methods were realized. The precise reasons for the variations of the driving force mechanism are discussed and analytic assessments of the modifications are made.

Chapter 5 describes the implementation of the analytic models into a implicit transient finite element scheme starting from the respective weak forms of the governing set of differential equations. The implementation is carried out for a two dimensional model setup. In case of the phase field model for fatigue crack growth the transformation of the implicit time integration into the cycle domain is described.

Chapter 6 illustrates the properties of the new phase field models in terms of the evaluation of a number of finite element simulations. Focus is thereby given on the issue of whether the resulting model behavior is sufficient in accordance with analytic solution and experimental observations from other studies.

Finally, several conclusions from the present work are drawn and an outlook regarding future investigations is given in chapter 7.

Noteworthy are different contributions in respective international journals, namely Schreiber et al., 2017; Schreiber et al., 2019a; Schreiber et al., 2019b; Schreiber et al., 2021; Schreiber et al., 2020a; Schreiber et al., 2020b, which have been published and describe several aspects of the present work. The papers are cited at the appropriate position in the following text. Furthermore, parts of the anisotropic model were supported by a student worker. The associated thesis, Ettrich, 2020 is also cited at the relevant place.

Chapter 2

Relevant Basics of Mechanics

2.1 Continuum Mechanics

The term mechanics is in general referred to as the study of forces and motions. Within continuum mechanics the core issue is to investigate how structures react to forces, that are exerted on them. Those structures may deform or even fail as consequence of the force transmission. Accordingly, one needs to analyze how exactly the forces are transmitted through the different parts of a structure. The main items are discussed within the present section. Comprehensive descriptions of the framework are provided by several textbooks, e.g. Gross and Becker, 2002; Altenbach, 2012; Betten, 2001.

2.1.1 Kinematics

Figure 2.1 illustrates the motion and deformation of a body. The body may be understood as a cloud of points infinitely small and infinitely closed to each other. The function $\varphi = \varphi(\mathbf{X}, t)$ describes the motion of points \mathbf{X} , defined as Lagrangian coordinates, from the reference configuration into the current configuration by a deformation. This can be expressed by

$$\mathbf{x} = \varphi(\mathbf{X}, t). \quad (2.1)$$

Note that in general the function $\varphi(\mathbf{X}, t)$ is nonlinear. In order to describe the deformation of line elements $d\mathbf{X}$ the deformation gradient \mathbf{F} is introduced such that

$$d\mathbf{x} = \mathbf{F}d\mathbf{X}. \quad (2.2)$$

Accordingly, the deformation gradient is defined by the partial derivatives of the current coordinates with respect to the reference configuration

$$\mathbf{F} = \frac{\partial \mathbf{x}}{\partial \mathbf{X}} = \text{Grad } \mathbf{x} = \text{Grad } \varphi(\mathbf{X}, t), \quad (2.3)$$

with $\det \mathbf{F} \neq 0$ in order to ensure uniqueness of the mapping. Furthermore, \mathbf{F}^{-1} exists and the transition is reversible. Also surface and volume elements may be transferred from the reference configuration to the current configuration or vice versa. The formula from Nanson maps surfaces $d\bar{S}$ of the current configuration with surfaces dS of the reference configuration by

$$\mathbf{n}d\bar{S} = J\mathbf{F}^{-T}\mathbf{N}dS, \quad (2.4)$$

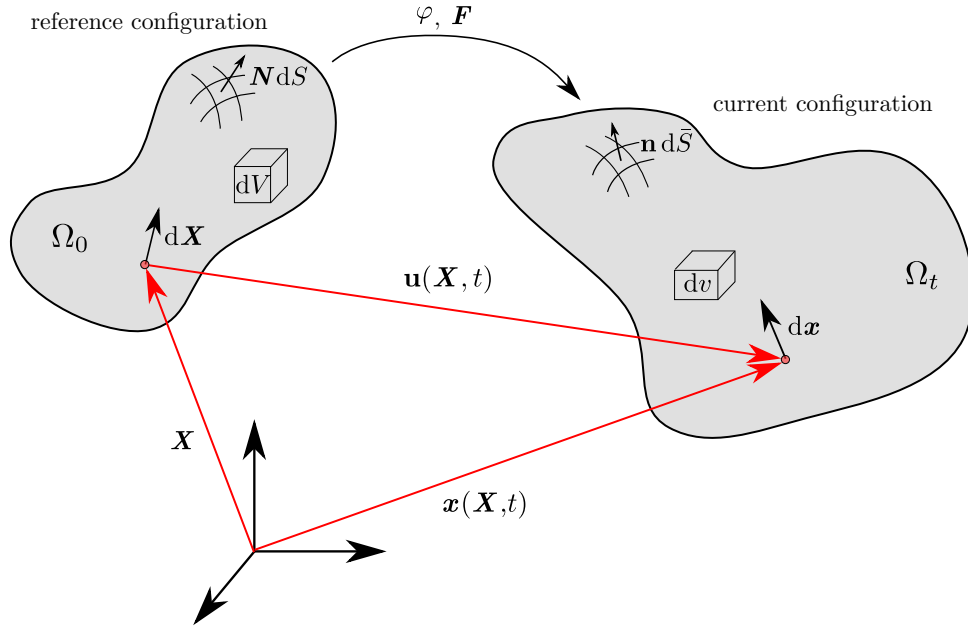


FIGURE 2.1: Schematic illustration of the motion and deformation of a body with indication of relevant quantities.

with the Jacobian $J = \det \mathbf{F}$ and the normal vectors \mathbf{N} as well as \mathbf{n} . Respective volume elements can be transferred by

$$dv = JdV. \quad (2.5)$$

Another important field quantity, which was not mentioned so far is the displacement vector $\mathbf{u}(\mathbf{X}, t)$. These vectors are found as the difference of the position vectors of current and reference configuration

$$\mathbf{u}(\mathbf{X}, t) = \mathbf{x} - \mathbf{X} = \varphi(\mathbf{X}, t) - \mathbf{X}. \quad (2.6)$$

Inserting this relation into (2.3) yields the relation

$$\mathbf{F} = \text{Grad}(\mathbf{X} + \mathbf{u}) = \mathbf{1} + \text{Grad} \mathbf{u}, \quad (2.7)$$

with the second order identity tensor $\mathbf{1}$. The tensor $\text{Grad} \mathbf{u}$ is referred to as the displacement gradient

$$\mathbf{H} = \text{Grad} \mathbf{u} = \frac{\partial \mathbf{u}}{\partial \mathbf{X}}. \quad (2.8)$$

2.1.2 Deformation

The deformation gradient \mathbf{F} contains rigid body motions and is therefore unsuitable as a strain measure. Any arbitrary deformation may be decomposed into a contribution of pure stretch and a contribution of pure rotation. Thus, the deformation gradient can be expressed by

$$\mathbf{F} = \mathbf{R}\mathbf{U} = \mathbf{V}\mathbf{R}, \quad (2.9)$$

with the orthogonal rotation tensor \mathbf{R} , the symmetric and positive definite right stretch tensor \mathbf{U} as well as the symmetric and positive definite left stretch tensor \mathbf{V} . In terms of these tensors the right Cauchy-Green tensor

$$\mathbf{C} = \mathbf{U}^2 = \mathbf{F}^T \mathbf{F} \quad (2.10)$$

as well as the left Cauchy-Green tensor

$$\mathbf{b} = \mathbf{V}^2 = \mathbf{F} \mathbf{F}^T \quad (2.11)$$

are defined. From this, an important strain measure within continuum mechanics, namely the Green-Lagrange deformation tensor

$$\mathbf{E} = \frac{1}{2} (\mathbf{C} - \mathbf{1}), \quad (2.12)$$

is derived, which can be expressed in terms of displacements

$$\mathbf{E} = \frac{1}{2} (\mathbf{H} + \mathbf{H}^T + \mathbf{H}^T \mathbf{H}). \quad (2.13)$$

The general nonlinear character is illustrated by the quadratic contribution $\mathbf{H}^T \mathbf{H}$. Within the current configuration typically the Euler-Almanic deformation tensor

$$\mathbf{e} = \frac{1}{2} (\mathbf{1} - \mathbf{b}^{-1}) \quad (2.14)$$

is applied

2.1.3 Stress

The left illustration in Figure 2.2 shows a body loaded by forces at its outer surface. The motion of several points of the body's surface is restrained causing reaction forces at these locations. The system of all acting forces may further be considered to be in equilibrium. A cut through the body is shown by the right illustration of Figure 2.2. By this cut, the internal forces become visible. The respective internal force dF transmitted across the surface element $d\bar{S}$ is described by

$$dF = \mathbf{t} d\bar{S}, \quad (2.15)$$

with the stress vector \mathbf{t} . Furthermore, the normal stress σ_n , which is parallel to the surface normal vector \mathbf{n} and the shear stress σ_t perpendicular to \mathbf{n} are indicated. The stress state at a certain point within the body is described by a symmetric second order tensor. According to Cauchy, the corresponding stress vector can be determined by this stress tensor and the surface normal vector of the corresponding cut by

$$\mathbf{t} = \boldsymbol{\sigma}^T \mathbf{n}. \quad (2.16)$$

The tensor $\boldsymbol{\sigma}$ is referred to as Cauchy stress tensor. As the body is considered to be in equilibrium, the sum of moments is required to be zero at every point, which renders $\boldsymbol{\sigma}$ a

symmetric tensor with only six independent components. It reads

$$\boldsymbol{\sigma} = \begin{bmatrix} \sigma_{xx} & \sigma_{xy} & \sigma_{xz} \\ \sigma_{yx} & \sigma_{yy} & \sigma_{yz} \\ \sigma_{zx} & \sigma_{zy} & \sigma_{zz} \end{bmatrix} \quad (2.17)$$

in matrix notation for Cartesian coordinates. In detail, this tensor describes the stress state with respect to a surface element in the current configuration. Accordingly, this stress is referred to as the true stress. The counterpart of the stress within the reference configuration is given by the 1. Piola-Kirchhoff stress tensor \mathbf{P} . It describes the current stress with respect to the surface element in the reference configuration. As the deformation gradient \mathbf{F} , the stress tensor \mathbf{P} is also unsymmetric. Analogously, this tensor maps surface vectors \mathbf{N} to corresponding stress vectors \mathbf{t}_0 within the reference configuration. The connection between the two stress tensors

$$\mathbf{P} = J\mathbf{F}^{-T}\boldsymbol{\sigma} \quad (2.18)$$

can be found from (2.4). The third important stress tensor is called the 2. Piola-Kirchhoff stress tensor. It is defined solely within the reference configuration as

$$\mathbf{S} = \mathbf{F}^{-1}\mathbf{P} = J\mathbf{F}^{-1}\boldsymbol{\sigma}\mathbf{F}^{-T}, \quad (2.19)$$

which renders it a symmetric tensor. The 2. Piola-Kirchhoff tensor \mathbf{S} may be interpreted as virtual initial stress related to the surface within the reference configuration.

2.1.4 Force Balance

Newton's second law may be considered for the body in Figure 2.2. With the sum of body forces $\mathbf{b} dm$ and the mass density ρ of a homogeneous body the equation of motion becomes

$$\int_{\Omega} \underbrace{\rho \mathbf{b}_i}_{f_i} dV + \int_{\partial\Omega} t_i(n_i) d\bar{S} = \int_{\Omega} \rho \ddot{u}_j dV \quad (2.20)$$

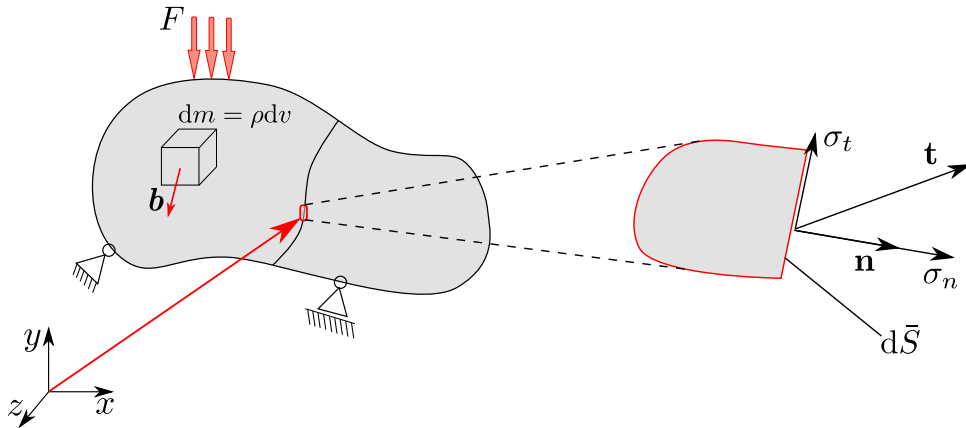


FIGURE 2.2: Schematic illustration of internal force transmission through a body with indication of relevant quantities.

or in tensor notation

$$\int_{\Omega} \rho \mathbf{b} \, dV + \int_{\partial\Omega} \mathbf{t} \, d\bar{\mathbf{S}} = \int_{\Omega} \rho \ddot{\mathbf{u}} \, dV. \quad (2.21)$$

Only the static case may be considered, which renders the right side of this balance zero. The stress vector \mathbf{t} can now be substituted by the stress tensor $\boldsymbol{\sigma}$ applying Cauchy's theorem (2.16). Furthermore, Gauss's theorem can be applied to the surface integral in (2.20), which yields

$$\int_{\Omega} \left(\frac{\partial \sigma_{ij}}{\partial x_i} + \rho b_j \right) dV = 0. \quad (2.22)$$

Since this equation provides a general formulation for the balance of forces of a given body, it is valid for any size of a body, including infinitesimal small bodies. Thus, one can argue that

$$\frac{\partial \sigma_{ij}}{\partial x_i} + \rho b_j = 0 \quad (2.23)$$

must be fulfilled at any arbitrary location. In tensor notation this equation reads

$$\operatorname{div} \boldsymbol{\sigma} + \mathbf{f} = \mathbf{0} \quad (2.24)$$

with $f_i = \rho b_i$. This law is referred to as the local or strong form of the balance of forces. Note that in the present form it is given in the current configuration. By means of the common quantities introduced above, it can however also be formulated for the reference configuration by

$$\operatorname{Div} \mathbf{P} + \mathbf{f}_0 = \mathbf{0}. \quad (2.25)$$

2.1.5 Small Deformations

For the continuum boundary value problem, the approach of small deformations provides a massive reduction in terms of complexity. The term small relates to a characteristic length of the body under consideration and accordingly,

$$\left| \frac{\partial u_i}{\partial X_j} \right| \ll 1. \quad (2.26)$$

The nonlinear part of the Green-Lagrange tensor (2.12)

$$\mathbf{E}^{\text{nonlin}} = \frac{1}{2} \mathbf{H}^T \mathbf{H} \quad (2.27)$$

becomes even smaller and is therefore neglected. The remaining linear part \mathbf{E}^{lin} of (2.12) is referred to as linearized strain tensor

$$\boldsymbol{\varepsilon} = \begin{bmatrix} \varepsilon_{xx} & \varepsilon_{xy} & \varepsilon_{xz} \\ \varepsilon_{yx} & \varepsilon_{yy} & \varepsilon_{yz} \\ \varepsilon_{zx} & \varepsilon_{zy} & \varepsilon_{zz} \end{bmatrix} = \frac{1}{2} \left[\frac{\partial \mathbf{u}}{\partial \mathbf{x}} + \frac{\partial \mathbf{u}^T}{\partial \mathbf{x}} \right]. \quad (2.28)$$

Note the differentiation with respect to \mathbf{x} in this equation, since within the small deformation setting a distinction of derivatives with respect to coordinates in the reference and in the current configuration is no more required. A general deformation consists of a pure volumetric part and a pure deviatoric part, describing the change of the shape for a fixed volume. The corresponding decomposition of the strain tensor is

$$\boldsymbol{\varepsilon} = \underbrace{\boldsymbol{\varepsilon} - \frac{1}{3}(\boldsymbol{\varepsilon} : \mathbf{1})\mathbf{1}}_{\boldsymbol{\varepsilon}^{\text{dev}}} + \underbrace{\frac{1}{3}(\boldsymbol{\varepsilon} : \mathbf{1})\mathbf{1}}_{\boldsymbol{\varepsilon}^{\text{vol}}}, \quad (2.29)$$

where $(\cdot) : (\cdot)$ represents the double contraction of two tensors. For the present case $\boldsymbol{\varepsilon} : \mathbf{1}$ it is also considered the trace operator $\text{tr}(\boldsymbol{\varepsilon}) = \varepsilon_{xx} + \varepsilon_{yy} + \varepsilon_{zz}$.

2.1.6 Constitutive Law

So far, the presented relations for strains and stresses are not sufficient to solve an existing boundary value problem within continuum mechanics. The additional set of equations still needed is called constitutive law. This law in general represents a certain material since it relates the stress state within the material with the applied deformation. The probably simplest constitutive law is

$$\boldsymbol{\sigma} = E\boldsymbol{\varepsilon}, \quad (2.30)$$

which is formally known as the one dimensional Hooke's law, where E is the Young's modulus of a linear elastic material. For the general case in linear elasticity, the constitutive law is derived from an elastic potential (see e.g. Wriggers, 2001). The derivative of the potential ψ with respect to the right Cauchy-Green tensor yields

$$\mathbf{S} = \frac{\partial \psi}{\partial \mathbf{E}}, \quad (2.31)$$

which within a small deformation setup becomes

$$\boldsymbol{\sigma} = \frac{\partial \psi}{\partial \boldsymbol{\varepsilon}}. \quad (2.32)$$

The potential for the linear elastic case is referred to as the linear elastic strain energy density function

$$\psi = \underbrace{\frac{1}{2}\boldsymbol{\varepsilon} : (\mathbb{C}\boldsymbol{\varepsilon})}_{\text{strain energy density } W}. \quad (2.33)$$

With this potential, (2.32) yields the general constitutive law for linear elasticity

$$\boldsymbol{\sigma} = \mathbb{C}\boldsymbol{\varepsilon} \quad (2.34)$$

with the fourth order stiffness tensor $\mathbb{C} = C_{ijkl}$. Due to the symmetry of $\boldsymbol{\sigma}$ and $\boldsymbol{\varepsilon}$ the stiffness tensor reveals the symmetry

$$C_{ijkl} = C_{ijlk} = C_{jikl}. \quad (2.35)$$

Furthermore, the symmetry

$$C_{ijkl} = C_{klij} \quad (2.36)$$

follows from permutability of the sequence for the second derivative of the potential with respect to the strains (Schwarz' theorem). Using these symmetries the number of independent components of \mathbb{C} is reduced from 81 to 21. The number is even more reduced in the case of an isotropic material, which finally can be described by only two so called Lamé constants λ and μ . The constitutive law (2.33) can then be rewritten by

$$\boldsymbol{\sigma} = 2\mu\boldsymbol{\varepsilon} + \lambda\text{tr}(\boldsymbol{\varepsilon})\mathbf{1}. \quad (2.37)$$

For practical reasons, the Lamé constants are often replaced by the parameters E and ν by the relations

$$E = \frac{\mu(3\lambda + 2\mu)}{\lambda + \mu} \quad \text{and} \quad \nu = \frac{\lambda}{2(1 + \nu)}. \quad (2.38)$$

The constitutive law may also be decomposed into volumetric and deviatoric contributions by

$$\boldsymbol{\sigma} = K\boldsymbol{\varepsilon}^{\text{vol}}\mathbf{1} + 2\mu\boldsymbol{\varepsilon}^{\text{dev}}, \quad (2.39)$$

where $K = \lambda + \frac{2}{3}\mu$ is the bulk modulus. For the sake of completeness it must be mentioned, that the underlying system of equations obtained from kinematics, the balance of forces, and the constitutive law is in general overdetermined. In detail the relation for the strain tensor (2.28) reveals six equations for three unknown displacements. In order to ensure that the deformed body still fits together so called compatibility conditions must be fulfilled.

2.2 Fracture Mechanics

The field of fracture mechanics deals with phenomena of the partial or complete separation of bodies. The main questions to be answered are: Do cracks nucleate under a certain load? Does a crack propagate under a certain load? Does the propagation lead to the final failure of a body? The latter includes the question of the crack path and the propagation speed. The issue can be considered on different scales as defects of different magnitude may lead to the final failure. The relevant concepts, which help to predict and describe the fracture behavior are based on macroscopic investigations. The outline in the following gives a short overview of items from relevant textbooks as e.g. Gross and Seelig, 2011 or Kuna, 2010. The description is in general based on quantities from continuum mechanics. However, for an appropriate description of specific crack properties the framework is enhanced by additional measures like stress intensity factors, energy release rate, or the J-integral. The situation at the crack tip is characterized by these items and therefore they are subsequently introduced in detail. The field of fracture mechanics is further classified into linear and nonlinear fracture mechanics. The nonlinear theory must be applied if inelastic material behavior occurs in a larger area around the crack tip and therefore significantly affects the cracking process. This is the case in ductile materials. The linear theory, where plastic material behavior is neglected is no more sufficient in this case. Within this work only linear elastic materials are considered and the extended phase field models are based upon

a model for brittle fracture. Therefore, it is sufficient to focus on the theory of linear elastic fracture mechanics.

2.2.1 Crack Opening Modes

Within a macroscopic characterization, a crack is approximated as a sharp cut within the material. The tip radius is assumed as infinitely small, which is different for a notch. The loading or deformation of the crack is a superposition of three principal so called crack opening modes. These modes are depicted in Figure 2.3. The first two modes are both referred to as in plane loading since the displacement of the crack surface occurs along the perpendicular plane. The mode I is characterized by the symmetric deformation of the opposite crack surfaces as caused by a tensile load. Within the mode II case, the opposite crack surfaces undergo a asymmetric displacement along with the crack tip orientation. This is caused by a shear load in the vicinity of the crack tip. Finally, the mode III induces an out of plane deformation. It describes a separation of the crack surfaces in tangential direction with respect to the crack front in a tearing mode.

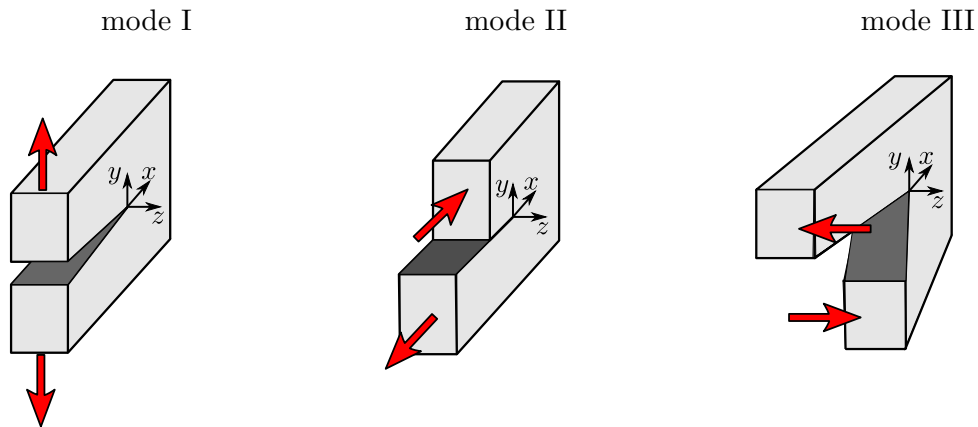


FIGURE 2.3: Schematic illustration of different crack opening modes.

2.2.2 Process Zone and K-concept

The area near the crack tip is referred to as the process zone. Inelastic processes take place within this zone. However, according to the theory of linear elastic fracture mechanics the process zone is considered very small compared to relevant dimensions. Furthermore, the material behavior is considered linear elastic for the rest of the body. The plastic material behavior within the process zone is neglected.

For a straight crack within an infinite two dimensional domain of linear elastic material the stress strain field around the crack tip can be solved analytically by means of complex functions or Airy's stress function. A detailed derivation is provided in e.g. Kuna, 2010.

Here simply the result is presented. The stresses around the crack tip read

$$\begin{bmatrix} \sigma_{xx} \\ \sigma_{yy} \\ \sigma_{xy} \end{bmatrix} = \frac{K_I}{\sqrt{2\pi r}} \cos\left(\frac{\varphi}{2}\right) \begin{bmatrix} 1 - \sin\left(\frac{\varphi}{2}\right) \sin\left(\frac{3\varphi}{2}\right) \\ 1 + \sin\left(\frac{\varphi}{2}\right) \sin\left(\frac{3\varphi}{2}\right) \\ \sin\left(\frac{\varphi}{2}\right) \cos\left(\frac{2\varphi}{2}\right) \end{bmatrix} \quad (2.40)$$

for a pure mode I load,

$$\begin{bmatrix} \sigma_{xx} \\ \sigma_{yy} \\ \sigma_{xy} \end{bmatrix} = \frac{K_{II}}{\sqrt{2\pi r}} \begin{bmatrix} -\sin\left(\frac{\varphi}{2}\right) \left[2 + \cos\left(\frac{\varphi}{2}\right) \cos\left(\frac{3\varphi}{2}\right) \right] \\ \sin\left(\frac{\varphi}{2}\right) \cos\left(\frac{\varphi}{2}\right) \cos\left(\frac{3\varphi}{2}\right) \\ \cos\left(\frac{\varphi}{2}\right) \left[1 - \sin\left(\frac{\varphi}{2}\right) \sin\left(\frac{3\varphi}{2}\right) \right] \end{bmatrix} \quad (2.41)$$

for a pure mode II load, and

$$\begin{bmatrix} \sigma_{xz} \\ \sigma_{yz} \end{bmatrix} = \frac{K_{III}}{\sqrt{2\pi r}} \begin{bmatrix} -\sin\left(\frac{\varphi}{2}\right) \\ \cos\left(\frac{\varphi}{2}\right) \end{bmatrix} \quad (2.42)$$

for mode III. Within this set of equations, r and φ are the respective polar coordinates describing the area around the crack tip, with the crack tip as the origin. Obviously, all stress fields reveal a singularity at the crack tip of the kind $r^{-1/2}$. Apart from the mentioned simplifications, the characteristics of the stress field for all three modes is exactly defined by the equations above. Note however, these solutions lose validity once r goes below a certain limit as the inelastic behavior occurring within this region is not taken into account within the derivation. Furthermore, for a precise estimation the factors K_I , K_{II} and K_{III} are to be determined. These factors are referred to as the stress intensity factors as they define the strength or the intensity of the particular load case. This does not only include the load magnitude but also the geometry of the body as well as the current crack length, which leads to the unit $[\text{MPa}\sqrt{\text{m}}]$ for the stress intensity factors. Formulas for these factors for several cases are given in e.g. Gross and Seelig, 2011.

The stress intensity factors, which are also called K-factors are used as fracture parameters as they describe the load characteristic around the crack tip. According to the so called K-concept onset of crack propagation occurs once the respective stress intensity factor exceeds a critical value. Accordingly,

$$K_I = K_{Ic}, \quad K_{II} = K_{IIc} \quad \text{or} \quad K_{III} = K_{IIIc}, \quad (2.43)$$

defines the critical load state. The quantities $K_{(\cdot)c}$ are referred to as critical stress intensity factor or fracture toughness. The equations (2.43) only hold if the present load case solely consists of the particular crack opening mode. For a general load case, which consists of several modes a generalized fracture criterion

$$f(K_I, K_{II}, K_{III}) = 0 \quad (2.44)$$

needs to be employed. This situation is referred to as mixed mode loading.

2.2.3 Griffith Theory and J-integral

Another way to approach the fracture problem is to consider an energetic description of the cracking process. The idea goes back to A. A. Griffith (see Griffith, 1921), who proposed to associate the change of surface energy Γ of a body with the size of the respective crack surface A . The infinitesimal surface energy is accordingly proposed to be proportional to the crack surface,

$$d\Gamma = \mathcal{G}_c dA. \quad (2.45)$$

The factor \mathcal{G}_c is a material specific quantity and is referred to as critical energy release rate. Furthermore, the change of internal energy is quantified by the energy release rate

$$\mathcal{G} = -\frac{d\Pi}{dA}, \quad (2.46)$$

where Π is the total potential of the body. The energy Γ contributes to the total energy of a body and represents all forms of energy coming along with the micro mechanical processes occurring during cracking. The complete energy balance can then be formulated in terms of the first Principle of Thermodynamics

$$\dot{E} + \dot{\Gamma} = \dot{W}, \quad (2.47)$$

where \dot{E} and $\dot{\Gamma}$ are the rates of inner and surface energy, respectively. The constraint $\dot{\Gamma} \geq 0$ is presumed as cracking is not reversible. The right hand side consists of the work rate caused by external forces \dot{W} . Note that in (2.47) kinetic energy and heat supply are neglected as fracture is considered to happen during a quasi static isothermal process. The complete body including the process zone is considered. Therefore, Γ contains also energies associated with the plastic deformation work at the crack tip. The inner energy E of the body can be expressed by the strain energy density Π^i . It is further assumed, that the external forces are conservative. Accordingly these forces reveal a potential Π^e and $\dot{W} = -\frac{d\Pi^e}{dt}$. Inserting these identities into the first principle (2.47) one finds

$$d\Pi^i + d\Pi^e + d\Gamma = 0 \quad (2.48)$$

and the division of this equation by dA yields Griffith's theory

$$\frac{d\Pi}{dA} + \frac{d\Gamma}{dA} = 0. \quad (2.49)$$

This equation can be interpreted as follows: The propagation of crack growth sets in once the increase of surface energy balances the release of potential energy. Inserting (2.45) and (2.46) in (2.49) yields

$$\mathcal{G} = \mathcal{G}_c. \quad (2.50)$$

Another parameter for quantification of the fracture tendency is the J-integral. This vector valued quantity is defined as the surface integral

$$\mathcal{J} = \int_{\partial\Omega} \boldsymbol{\Sigma} \, d\mathbf{S}, \quad (2.51)$$

where $\boldsymbol{\Sigma}$ represents the Eshelby stress tensor

$$\boldsymbol{\Sigma} = W\mathbf{1} - \nabla\mathbf{u}^T\boldsymbol{\sigma} \quad \text{or} \quad \Sigma_{kj} = W\delta_{jk} - \sigma_{ij}\frac{\partial u_i}{\partial x_k}, \quad (2.52)$$

receptively. Using Gauss's theorem, the surface integral (2.51) can be transferred to a volume integral

$$\mathcal{J}_k = \int_{\Omega} \frac{\partial W}{\partial \varepsilon_{mn}} \frac{\partial \varepsilon_{mn}}{\partial x_j} \delta_{jk} - \left(\frac{\partial \sigma_{ij}}{\partial x_j} \frac{\partial u_i}{\partial x_k} + \sigma_{ij} \frac{\partial u_i}{\partial x_k \partial x_j} \right) \, dV. \quad (2.53)$$

The first term in brackets vanishes due to the balance law (2.23). If further (2.32) and the identity

$$\frac{\partial \varepsilon_{mn}}{\partial x_j} \delta_{jk} = \frac{\partial \varepsilon_{mn}}{\partial x_k}, \quad (2.54)$$

is incorporated one obtains

$$\operatorname{div}\boldsymbol{\Sigma} = \mathbf{0}. \quad (2.55)$$

Accordingly, the J-integral (2.51) vanishes for any volume, which is free of singularities. If however, the material contains crack tips with the corresponding singularities the J-integral is not zero. It can be shown, that the change of the inner energy of a body caused by the translation of material defects as e.g. cracks is proportional to the J-integral. Within a two dimensional setting the surface integral becomes a curve integral and the vector components \mathcal{J}_1 describe the energy release associated with the translation in x_1 direction of the crack tip surrounded by the curve (see Figure 2.4). For the setup in Figure 2.4 the

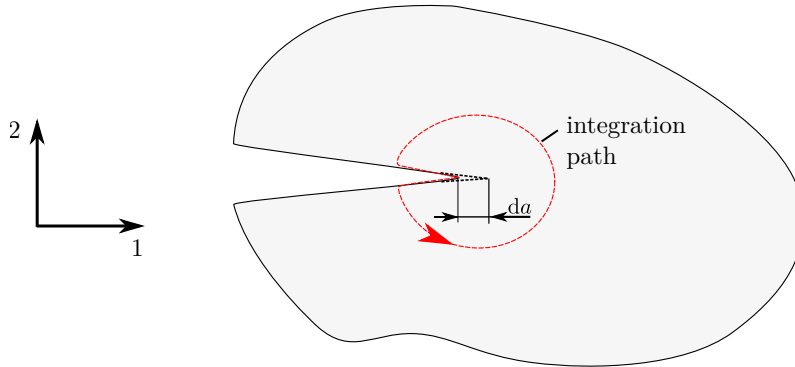


FIGURE 2.4: Schematic illustration of the J-integral for two dimensions.

first component \mathcal{J}_1 is the energy release rate with

$$\mathcal{J}_1 = \mathcal{G} = -\frac{d\Pi}{da} \quad (2.56)$$

and the criterion for crack propagation is therefore

$$\mathcal{J}_1 = \mathcal{J}_c. \quad (2.57)$$

For a straight crack with traction free crack surfaces Rice, 1968 showed that \mathcal{J}_1 is path independent. Additionally, it can be shown that the energy release rate for a crack under arbitrary load can be described as a function of the three crack stress intensity factors of the particular crack opening modes with

$$\mathcal{G} = \mathcal{J}_1 = \frac{1-\nu^2}{E}(K_I^2 + K_{II}^2) + \frac{1}{2\mu}K_{III}^2 \quad (2.58)$$

under the assumption of strains occurring only in plane directions. Accordingly, within linear elastic fracture mechanics, the three presented concepts are equivalent to a certain extent.

2.3 Fatigue of Materials and Structures

The field of mechanical fatigue of materials is concerned with the investigation and description of phenomena causing failure under repeated loading and unloading, where the forces cause small stresses in relation to static thresholds. Fatigue is related to all fields of engineering as a number of catastrophic accidents from the past give a significant reason for the study of the phenomenon. The problem is known since the period of industrialization as failures occurred, which could not be explained by common knowledge. The studies from August Wöhler (see e.g. Wöhler, 1866) are referred to as pioneer work within the field of fatigue failure. Wöhler found that steel shafts could not resist the repetition of loading and unloading by a bending moment even for very small moments. He performed a number of experiments with varying load amplitudes and plotted the number of applied load cycles versus the respective amplitude. This kind of diagram is today widely known as Wöhler curve or S-N curve and provides a basic tool to describe the phenomenon. The reason for the failure under small loads could, however, not be explained at this early stage of the investigation. Nowadays, as material defects and the underlying processes within the material are known the micromechanical processes associated with cyclic fatigue are investigated. Several textbooks as e.g. Schijve, 2009; Haibach, 2006; Dowling, 2013; Suresh, 1992 deal with the phenomenon. The physical basics and the current state of fatigue lifetime estimations are outlined in the following.

2.3.1 General Description of the Phenomenon

Within machines, components or structures are subjected to cyclic loads since vibrations from arbitrary sources are present in the structures. The process of mechanical fatigue generally involves the accumulation of damage caused within the individual load reversals. This leads to the formation of microscopic cracks and with ongoing cycling to the extension of these micro defects to macroscopic cracks. Those are then propagated and finally lead

to fatal failure of the structure. The schematic illustration in Figure 2.5a) summarizes the basic mechanisms responsible for the initiation of microcracks caused by cyclic loading. Suppose the specimen on the left of the illustration is subject to a harmonic load function. In the case of a metallic polycrystalline material there are grains prone for early initiation of dislocation slip. The quantity, which qualifies the grains in this regard, is the lattice orientation with respect to the load direction as this determines the magnitude of the shear stress. A spot where dislocations become active is shown in the zoom of Figure 2.5a). During the first half cycle a slip step is created. The required stress to reverse this slip step is higher due to strain hardening. Accordingly, during the reverse half cycle slip is more likely to occur on a neighbor slip system. This is illustrated by sketch number two. This underlines that the consequences of the cyclic slip are not fully reversible from a micromechanical perspective. The sequence of dislocation gliding on parallel slip planes goes on and on with further cycling to form a so called slip band. Within this slip band the material separates at a point to form a microcrack. The outlined processes essentially occur at free surfaces as less material surrounds the slipping action, which decreases the threshold stress. However, note that in this regard a "free surface" can also be the surface of a defect within the material. The so created microcrack will further extend while it contributes to an even higher risk of dislocation slip due to the stress concentration at the crack tip. On the other hand the propagation is hindered once it penetrates grain boundaries. Accordingly, the nucleation of a micro crack does not always mean that it comes to final failure. This is a question of the sequence and the magnitude of the load cycles. Once the microcrack has grown to an order such that it is visible in optical measurements, it is denoted a macrocrack. The different phases of the complete fatigue life are indicated in Figure 2.5b). It is categorized by two main phases. The contribution in terms of time for

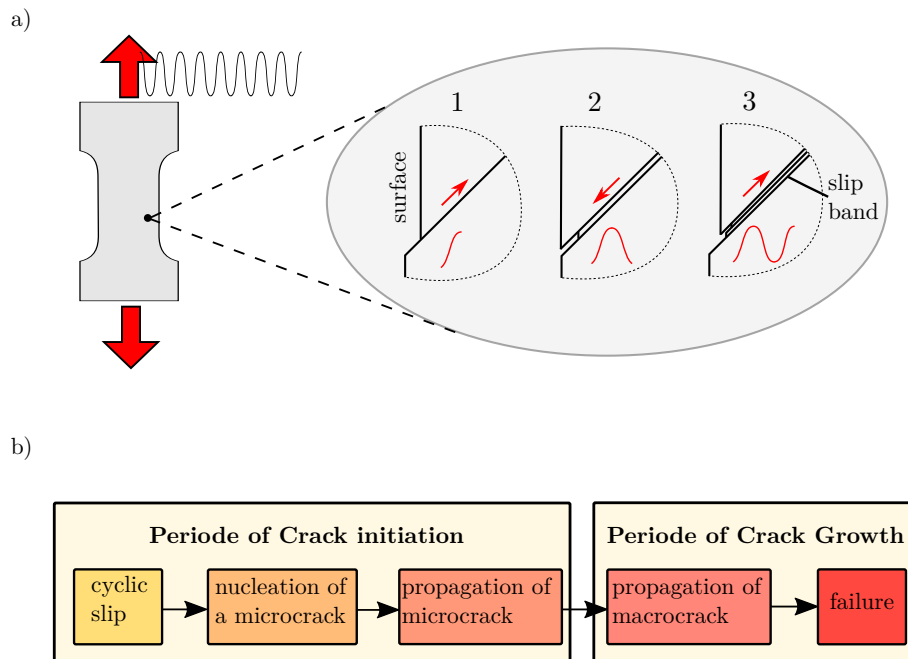


FIGURE 2.5: Description of the fatigue phenomenon: a) schematic illustration of the cyclic dislocation process during the phenomenon of mechanical fatigue, b) different phases.

each of the two phases depends on the material, environmental conditions, and certainly on the load history. Common approaches for the description of the fatigue life of structures are mainly based on empirical studies, due to the complexity of the process.

2.3.2 Total Life Approach

Specific methods for each of the introduced stages of the fatigue life exist. The general concept dealing with the crack initiation phase is referred to as the total life approach. This concept is mainly based on the application of S-N curves. These curves are, in honor of the seminal work of A. Wöhler, also referred to as Wöhler curves. Within Figure 2.6 a S-N curve is shown exemplarily. It is a plot of the specific load amplitude versus the bearable number of load cycles until failure. It was found that for most materials, a linear relation is observed within a double logarithmic diagram. The curves are recorded by means of cyclic experiments with basic round or flat specimens. The load amplitude within a single test is constant. The load is related to the nominal stress obtained by the maximum force with respect to the undeformed cross section of the specimen. Some metals as for instance steel show a distinct fatigue limit. This means that the slope of the S-N curve is zero beyond a certain number of load cycles (infinite life). Denoting this fatigue limit with σ_D the S-N law is

$$N_F = N_D \left(\frac{\sigma_A}{\sigma_D} \right)^{-k} \quad \text{for } \sigma_A \geq \sigma_D, \quad (2.59)$$

with the slope k and the knee point cycle number N_D . Due to the design of the specimens the number of cycles until macro crack initiation covers about 90% of the complete lifetime. Accordingly, it is common to designate the point of macro crack initiation as the point of total failure even if it is not entirely correct. In order to provide statistical significance a number of tests is performed for every load amplitude. A standard defining the procedure to record a S-N curve is provided by DIN50100 (see. DIN, 2016).

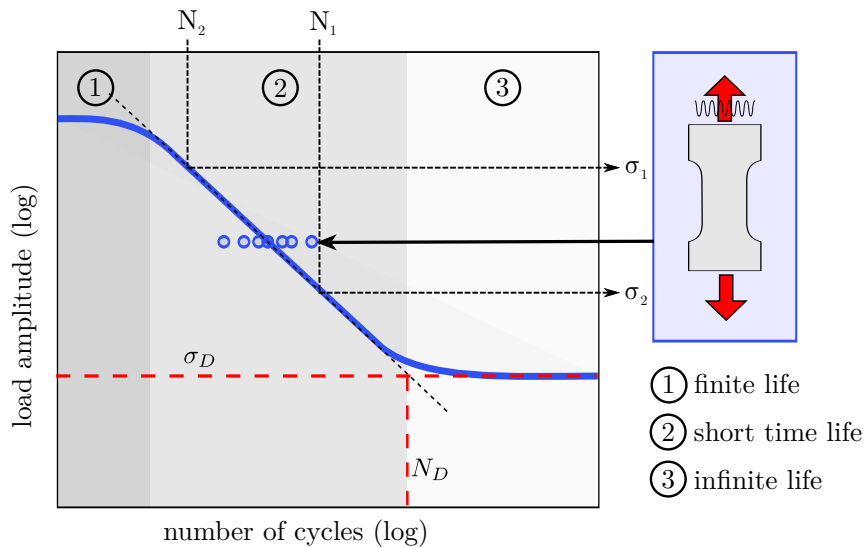


FIGURE 2.6: Schematic illustration of S-N line with explanation of several important quantities.

The general procedure of the total life approach is to count and categorize the particular load cycles from the load time function that is applied to the structure under investigation. Different counting methods were proposed in this regard, where the so called rainflow counting (see Clormann and Seeger, 1986) is most frequently used. The contribution to the fatigue damage of a particular category of load cycles can then be determined by Miner's law (see. Miner, 1945)

$$D = \sum_{i=1}^n \frac{1}{N_{F_i}} \cdot n_i, \quad (2.60)$$

where N_{F_i} is the number of load cycles until failure for a certain amplitude obtained from a respective S-N curve. n_i is the number of cycles applied with this amplitude. Within this concept, failure occurs for $D = 1$.

2.3.3 Fatigue Crack Growth

This approach applies to the description of the second part of the fatigue life, which covers the period from the occurrence of a macro crack to the final failure of a structure. The behavior is called fatigue crack growth and the associated approach is based on fracture mechanical concepts. In section 2.2 it was found that for a static load of cracked members no crack growth occurs as long the threshold K_c is not exceeded. However, as outlined above the crack can be propagated by cyclic loading. Commonly the stress intensity factor range ΔK is used to describe the fatigue crack growth behavior. This quantity is also referred to as the cyclic stress intensity factor and defines the range between the K values associated with minimum and maximum load (see left illustration in Figure 2.7). In the case of a mode I crack

$$\Delta K_I = K_I^{\max} - K_I^{\min}. \quad (2.61)$$

The major contribution to this field was proposed by Paris and Erdogan, 1963, who found, that fatigue crack growth rates da/dN render a power function of the cyclic stress intensity factor within the range of stable crack growth. As illustrated in Figure 2.7 it is useful to

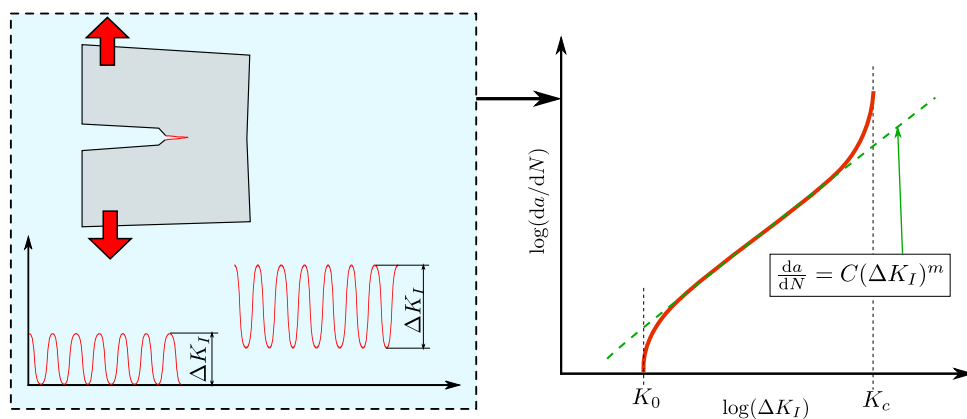


FIGURE 2.7: Schematic illustration of Paris law.

plot the growth rates within logarithmic scales since the relation then becomes a linear

function. This function for the crack speed is described by

$$\frac{da}{dN} = C\Delta K_I^m, \quad (2.62)$$

which is commonly denoted the Paris law. The parameters C and m basically vary for different materials but also depend on environmental properties as well as the stress ratio $R = K_I^{\min}/K_I^{\max}$ and the mean stress of the load range. Similar to the fatigue limit from the total life approach, the threshold K_0 marks the load below which no propagation of the crack takes place. On the other hand, the curve of the crack growth rates becomes steep indicating the threshold K_c , which marks the point where unstable crack growth sets in. If the Paris law is known for a certain material, the prediction of the lifetime for a certain load case described by a respective stress intensity factor can be estimated as (2.62) may be integrated to obtain ΔN .

Chapter 3

Phase Field Modeling of Fracture

The scientific basics from the field of mechanics outlined in the previous sections provide a framework for the phase field fracture model, which is discussed in this chapter. This model is used to investigate and evaluate the cracking behavior under complex loading conditions such as cyclic loading or fatigue crack growth, respectively and the crack propagation in materials that show a directionality of the fracture resistance. The latter implies that the critical energy release rate is a function $\mathcal{G}_c(\theta)$, with θ representing the crack deflection direction. However, before the reader is introduced to developments that enable this kind of investigation, the fundamental works of phase field modeling as applied to a number of physical problems and also in terms of fracture are discussed within this chapter. For this purpose, general remarks will be given, which are concerned with the history of phase field modeling with special focus on basic properties and benefits. Following up on the latter, a detailed description is provided dealing with the main ingredients needed to apply the phase field method to fracture mechanics. It is important to understand the basic linkage of phase field fracture models and fundamental concepts of conventional fracture mechanics, in particular Griffith's theory (Griffith, 1921) of energy balances. As the recent basis for the presented work, the phase field model proposed by Kuhn and Müller, 2010 will be outlined to provide a comprehensive overview.

3.1 General Remarks on Phase Field Modeling

As a matter of fact, interfaces between different microstructures or phases are generated within a large number of physical processes. For the purpose of technical applications, it is very often of high interest to determine how certain interfaces between different phases behave and evolve. The term phase is interpreted in a general way in this context. For example, the kinetics of the martensite to austenite phase transformation controls strength and ductility of stainless steels. For metal casting processes the temporal behavior of solidification is highly decisive for the mechanical properties of the cast and also for the geometrical accuracy. The wetting behavior of a liquid can significantly effect the properties of an adhesive or a solder joint. Of course the cracking behavior, where the two phases of interest are intact and broken material, affects the durability of any technical structure, which experiences loads of any kind. Illustrative examples for spatially separated phases occurring in those processes are for instance different crystal structures, materials of different density, different electric properties like e.g. polarization or even different contributions of structural integrity. The numerical simulation of these interfacial processes via so called sharp interface models is often encountered by obstacles (see e.g. Provas and Elder, 2010; Rajkotwala et al., 2019) concerning the tracking of the interface, which is very problematic

for topologically difficult situations. Furthermore, physical properties must be averaged at interfaces. In terms of fracture, the respective crack surfaces are explicitly mapped to the spatial discretization within sharp interface models. Accordingly, the discretization has to be adapted every time the crack propagates. Speaking in terms of finite elements, remeshing algorithms have to be included within the solution scheme. From a simulation point of view, the solution algorithms become complex and possibly time consuming.

A promising alternative framework to overcome the issues of sharp interface approximations is the phase field modeling paradigm. For the differentiation of relevant phases an auxiliary parameter, often referred to as phase field parameter or order parameter, is introduced in this method. To enable a smooth representation of all fields without problems of jump sets the field of this auxiliary parameter, the phase field in general identified as $\phi(\mathbf{x}, t)$, is continuous in space and time. Certain values of this variable represent certain material phases. The phase field is coupled to the relevant degrees of freedom describing a particular physical problem. The precise value of the order parameter specifies which phase is located at a given point. However, in that concern one generally has to differentiate between two types of interpretations of the order parameter. A first interpretation is that this variable solely differentiates the phases in order to overcome the explicit tracking of the interface or in other words to provide a diffuse approximation of sharp interfaces. This type is resembled by most of the novel models for solidification as in e.g. Kobayashi, 1993 or Wheeler et al., 1993. Within the other type of interpretation, each intermediate value of the phase field has a well defined physical description of a certain state as e.g. order to disorder transition microstructures (see. e.g. Chen and Wang, 1996). Returning to fracture problems, the phase field may indicate the value 1 for intact material and 0 for fractured material or a crack, respectively. However, the intermediate range can also be interpreted as the state of damage, which describes the volume fraction of material flaws. The order parameter therefore is a physical quantity. The phase field method provides benefits in terms of numerical simulation as the interfaces are generally approximated by a diffuse but compact transition region. The first continuum phase field model explicitly using the term phase field was – at least to the best of the authors’ knowledge – proposed by Kobayashi, 1993 for the growth of dendrites occurring within solidification processes. Basically, what was accomplished within this work is to substitute the source term in the diffusion equation of a sharp interface model by the time derivative of an order parameter, which takes the value 0 for liquid phase and 1 for solid phase. The resulting coupling of the temperature field and the evolution of the phase field delivered the very beneficial properties, which since then are very much appreciated by researchers of many different fields. In order to illustrate the wide spread of the phase field method over many areas, Table 3.1 provides a brief overview (not claiming completeness) of different applications and corresponding cites.

The equations describing the temporal evolution of the phase are commonly derived from potentials of free energy, which are mathematically treated as functionals $F[\phi(\mathbf{x}, t)]$. The minimization of the respective free energy functionals yields the temporal evolution of the phase field variable, which is in general governed by nonlinear partial differential equations. Therefore, the continuum equations

Research Field	Corresponding Phase Field Literature
solidification	Kobayashi, 1993, Wheeler et al., 1993, Wang et al., 1993, Nestler and Wheeler, 2002
solid-state phase transformation	McFadden and Wheeler, 2002 Steinbach and Apel, 2006, Schmidt et al., 2017
grain growth and coarsening	Nestler, 1999, Kazaryan et al., 2001, Kim et al., 2014,
fracture	Kuhn and Müller, 2010, Kuhn et al., 2016, Miehe et al., 2010b, Aldakheel et al., 2018a Borden et al., 2016, Schlüter et al., 2014,
dislocation dynamics and interaction	Wang and Li, 2010, Koslowski et al., 2002, Mianroodi and Svendsen, 2015
electromigration, magnetic-ferroelectric fields	Xu. et al., 2010 , Dineva et al., 2011, Bhate et al., 2000
static and dynamic wetting	Wang et al., 2018, Diewald et al., 2020, Badillo, 2015

TABLE 3.1: A selection of various applications of the phase field method with corresponding references.

$$\Lambda \frac{\partial \phi(\mathbf{x}, t)}{\partial t} = - \frac{\delta F}{\delta \phi(\mathbf{x}, t)} \quad (3.1)$$

and

$$\frac{\partial \phi(\mathbf{x}, t)}{\partial t} = L \nabla \cdot \left[\nabla \frac{\delta F}{\delta \phi(\mathbf{x}, t)} \right] \quad (3.2)$$

are commonly employed. The equation (3.1) is referred to as the time dependent Ginzburg-Landau or Allen-Cahn equation and was first applied to first order phase transformations by Chan, 1977. In this equation Λ is a viscous regularization coefficient to account for relaxation effects towards equilibrium. The latter equation is referred to as Chan-Hilliard equation and was specifically derived for the problem of spinodal decomposition. For the model presented in the following chapter the Ginzburg-Landau equation was utilized. Therefore, the following derivations focus on (3.1).

3.1.1 Evolution of Phase Transformations

A combination of a bulk energy and an interface energy is proposed for the free energy of a system with interfaces. The respective functional is

$$F[\phi(\mathbf{x}, t)] = \int_{\Omega} \psi(\phi, \nabla \phi) dV = \int_{\Omega} \left[f(\phi) + \frac{1}{2} \kappa |\nabla \phi|^2 \right] d\Omega, \quad (3.3)$$

where the first term represents the bulk energy density and the second term is a non-local contribution in the form of a gradient term, which accounts for interfacial energy. The

coefficient κ associated with the gradient energy term must be positive to ensure stability for the case of only one present phase. Using the free energy (3.3) and applying the first variation of the functional $F[\phi(\mathbf{x}, t)]$, namely

$$\delta F[\phi(\mathbf{x}, t)] = \int_{\Omega} \delta\phi \left[\frac{\partial\psi}{\partial\phi} - \nabla \cdot \frac{\partial\psi}{\partial\nabla\phi} \right] d\Omega \quad (3.4)$$

with $\delta\phi$ being the virtual distance to a neighbor function of ϕ (see e.g. Betten, 2004), the functional derivative can be formulated by

$$\frac{\delta F}{\delta\phi} = \frac{\partial\psi}{\partial\phi} - \kappa\nabla \cdot \left(\frac{\partial\psi}{\partial\nabla\phi} \right) \quad (3.5)$$

and hence (3.1) yields

$$\Lambda\dot{\phi} = \kappa\nabla \cdot \left(\frac{\partial\psi}{\partial\nabla\phi} \right) - \frac{\partial\psi}{\partial\phi}. \quad (3.6)$$

The state $\delta F/\delta\phi = 0$ is a necessary condition for an extreme value of F and hence the vanishing of this quantity characterizes an energetic equilibrium. Accordingly, (3.6) can be viewed as the description for a relaxation to reach equilibrium governed by the viscosity parameter $\Lambda > 0$. An important ingredient of a phase field model is the energy potential $f(\phi)$, see (3.3). The details of appropriate potentials for fracture phase field models will be discussed in later sections. However, at this point a brief discussion of two commonly applied potentials is outlined. A widely used form of a potential is the so-called double well potential

$$f(\phi) = \gamma\phi^2(1 - \phi)^2 \quad (3.7)$$

with the threshold for activation of $\gamma/16$, which acts as a natural barrier for a phase transformation. A driving force has to induce energy that exceeds this barrier to cause a transformation from one phase to the other. As illustrated in Figure 3.1a) in the basic form of (3.7), the double well potential has two minima $f = 0$ for $\phi = 0$ and $\phi = 1$, respectively. Introducing proper coefficients, these minima can be shifted along the vertical axes in order to account for deviations of quantities related to the two different phases. This form of an energy potential was used in numerous phase field models as e.g in the studies proposed by Kobayashi, 1993 or Karma et al., 2001.

Another often applied free energy potential, that reveals advantages from a computational point of view is the double obstacle potential (see Figure 3.1b)). Similar to the double well potential, the double obstacle potential shows an activation threshold γ . However, its piecewise definition

$$f(\phi) = \gamma(1 - \phi^2) + I(\phi), \quad (3.8)$$

with:

$$I(\phi) = \begin{cases} \infty & \text{for } |\phi| > 1 \\ 0 & \text{for } |\phi| \leq 1 \end{cases}$$

illustrates, that for values of the order variable outside $-1 \leq \phi \leq 1$ the energy is assumed

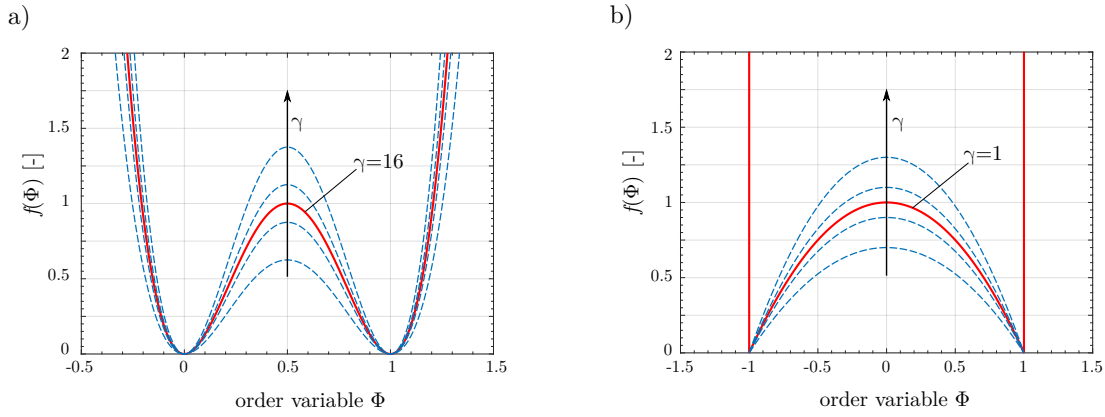


FIGURE 3.1: Commonly used free energy potentials within the phase field modeling paradigm: a) double well potential, b) double obstacle potential.

infinite. Therefore, outside of the interfacial region the order variable will strictly be 1 or -1 according to the respective phase. In contrast for the double well potential (3.7) the phase field will comparatively slowly go to the values representing the non-interface phases. The double obstacle potential is used throughout the complete variety of phase field modeling, as in e.g. in Steinbach and Apel, 2006 or Nestler and Wheeler, 2002. The double obstacle potential requires an explicit approximation, which yields a decoupling of the system of equations in space and is therefore very efficient if run in parallel. However, very small time steps may be required, which counterbalances this benefit with respect to implicit solvers.

3.1.2 Generalization of Ginzburg-Landau Equation

The derivation of the basic evolution equation for the phase field variable (3.6) was formally accomplished by variation of the free energy with respect to the field of the order parameter. The derivation of this approach is rather less illustrative and one barely can find the connection to balance laws as basic characterization for dissipative processes. However, in order to show the compatibility with the second law of thermodynamics, the derivation can be generalized as done by Gurtin, 1996. In this work, a clear separation between balance laws and constitutive equations is ensured by the introduction of a theory based on microforces. This theory was initially proposed in Fried and Gurtin, 1994 and it basically associates the change of an order parameter, i.e. the material configuration, representing a certain phase with the action of a system of microforces, see Figure 3.2. This system is postulated to obey the balance equation

$$0 = \int_{\partial\mathcal{P}} \boldsymbol{\xi} \cdot \mathbf{n} \, dS + \int_{\mathcal{P}} (\pi + \tau) \, dV \quad (3.9)$$

within a region \mathcal{P} . Classical forces such as traction loads act externally and cause deformations of a body \mathcal{B} . The introduced system of microforces acts within the body and is associated with the changes of the material configuration represented by the order parameter. The force balance (3.9) includes contributions of the scalar internal microforce π , representing microstructural tension associated with lattice defects, the scalar external microforce τ , representing externally caused microstructure changes of \mathcal{P} and those from

the microstress vector $\boldsymbol{\xi}$ on $\partial\mathcal{P}$. The vector \mathbf{n} is the outer normal vector of the surface element dS . The work expended by these microforces goes along with changes of the order parameter ϕ . Accordingly, the terms $\pi\dot{\phi}$ and $\tau\dot{\phi}$ are power densities accounting for work expended on atoms by sources, internal and external of the control volume \mathcal{P} , respectively. Power distributed over the surface $\partial\mathcal{P}$ caused by neighboring sources is taken into account by $\dot{\phi}\boldsymbol{\xi} \cdot \mathbf{n}$.

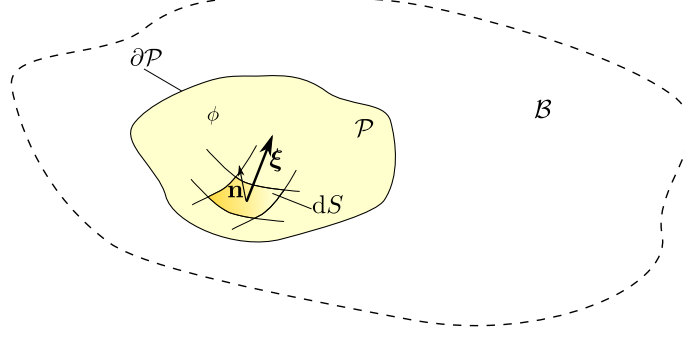


FIGURE 3.2: Illustration of body with phase ϕ governed by acting of microforces.

In order to formulate a dissipation inequality describing the proposed system of microforces, one may start with the first principal of thermodynamics, which is

$$\frac{d}{dt} \int_{\mathcal{P}} u \, dV = - \int_{\partial\mathcal{P}} \dot{\mathbf{q}} \cdot \mathbf{n} \, dS = \dot{W}. \quad (3.10)$$

if heat supplies are neglect. In (3.10) u is the specific inner energy and $\dot{\mathbf{q}}$ represents the heat flux. With the absolute temperature ϑ and under the assumption of no heat supplies, the Clausius-Duhem inequality becomes

$$\frac{d}{dt} \int_{\mathcal{P}} e \, dV \geq - \int_{\partial\mathcal{P}} \frac{\dot{\mathbf{q}}}{\vartheta} \cdot \mathbf{n} \, dS \quad (3.11)$$

with the specific entropy e . Considering the formulation of the Helmholtz free energy $\psi = u - \vartheta e$ together with (3.10) and (3.11) yields a dissipation inequality of the form

$$\frac{d}{dt} \int_{\mathcal{P}} \psi \, dV \leq \int_{\partial\mathcal{P}} \dot{\phi} \boldsymbol{\xi} \cdot \mathbf{n} \, dS + \int_{\mathcal{P}} \tau \dot{\phi} \, dV, \quad (3.12)$$

with the rate \dot{W} for the proposed system being provided solely by microforces, where π has no contribution as it acts at the internal of \mathcal{P} . Utilizing partial integration, the surface integral in (3.12) can be reformulated as

$$\int_{\partial\mathcal{P}} \dot{\phi} \boldsymbol{\xi} \cdot \mathbf{n} \, dS = \int_{\mathcal{P}} \dot{\phi} \operatorname{div} \boldsymbol{\xi} \, dV + \int_{\mathcal{P}} \boldsymbol{\xi} \cdot \nabla \dot{\phi} \, dV, \quad (3.13)$$

and accordingly together with (3.9) the strong form of the dissipation inequality (3.12) can be formulated by

$$0 \geq \dot{\psi} + \pi \dot{\phi} - \boldsymbol{\xi} \cdot \nabla \dot{\phi}. \quad (3.14)$$

In order to relate this inequality with the strong form of the balance law (3.9)

$$0 = \operatorname{div} \boldsymbol{\xi} + \pi + \tau, \quad (3.15)$$

the general constitutive equations

$$\psi = f_\psi(\phi, \dot{\phi}, \nabla \phi), \quad \boldsymbol{\xi} = f_\boldsymbol{\xi}(\phi, \dot{\phi}, \nabla \phi), \quad \pi = f_\pi(\phi, \dot{\phi}, \nabla \phi) \quad (3.16)$$

are considered. These relations are incorporated in (3.14), which yields

$$0 \geq \dot{\phi} \left(\frac{\partial f_\psi}{\partial \phi} + f_\pi \right) + \nabla \dot{\phi} \cdot \left(\frac{\partial f_\psi}{\partial \nabla \phi} - f_\boldsymbol{\xi} \right) + \ddot{\phi} \frac{\partial f_\psi}{\partial \dot{\phi}} \quad (3.17)$$

where the restrictions

$$\frac{\partial f_\psi}{\partial \dot{\phi}} = 0 \quad \text{and} \quad \frac{\partial f_\psi}{\partial \nabla \phi} = f_\boldsymbol{\xi} \quad (3.18)$$

are required in order to ensure the inequality, since the field ϕ does in general not prohibit arbitrary values for its derivatives at a certain location. Gurtin, 1996 showed that the most general solution of (3.17) with restrictions (3.18) is given by

$$\frac{\partial f_\psi}{\partial \phi} + \pi = -\Lambda(\phi, \dot{\phi}, \nabla \phi) \dot{\phi} \quad (3.19)$$

with $\Lambda \geq 0$ being a kinetic modulus. This solution reveals, that the internal microforce depends on a contribution of dissipation and also on a contribution driven by the changes of the free energy with respect to the order parameter. This illustrates the impact of phase transition caused by the acting of microforces. According to these derivations (3.19) yields constitutive functions for ϕ in accordance to the second law represented by (3.14). Inserting (3.19) and (3.18) under consideration of the constitutive laws (3.16) into the force balance (3.15) yields

$$\Lambda(\phi, \dot{\phi}, \nabla \phi) \dot{\phi} = \operatorname{div} \left(\frac{\partial f_\psi}{\partial \nabla \phi} \right) - \frac{\partial f_\psi}{\partial \phi} \quad (3.20)$$

for no action of external sources ($\tau = 0$). As consequence of the first restriction in (3.18) the functions for $\boldsymbol{\xi}$ and ψ do not depend on the time derivative $\dot{\psi}$. In the case of a constant kinetic coefficient and introducing a free energy of the form of (3.3) one obtains the evolution equation of the order parameter (3.6). In other words, the Ginzburg-Landau equation is generalized and an evolution equation is obtained for the order parameter ϕ describing an energy potential that depends on the order parameter and its spatial gradient, which results from a microforce balance.

3.2 Free Energy Potential for Fracture

Within the previous sections it was explained how the evolution equation for a phase field model can be obtained in general. The derivation assumes that a free energy functional, associated with a certain microstructural phenomenon, is available. However, a convenient free energy functional characterizing fracture was not presented so far. In fact, the description of such a functional must be classified as a further key point for reliable phase field models. In that concern, it took a number of meaty studies from different researchers before an appropriate formulation of a total energy was finally proposed. The particular steps from an attempt to generalize Griffith's theory to the regularization of cracks by means of a two phase functional are briefly outlined in the following.

3.2.1 The Variational Model of Brittle Fracture

As outlined within chapter 2.2 the theory of surface energy linkage to cracks proposed by Griffith, 1921 provides a fundamental framework for a macroscopic description of infinitesimal crack extension. The irreversible processes occurring within the formation of cracks are associated with an equivalent surface energy contribution proportional to the crack surface, which is in competition with the change of the elastic energy. During crack propagation the released energy must be equal to the energy consumption due to cracking. This resembles the energetic fracture criterion (2.49). Today Griffith's theory is honored as a key framework of linear fracture mechanics and standard in any textbook on fracture. Nevertheless, this energy theory is subjected to some shortcomings preventing a wide practical application. It can be predicted at which state the total energy of a loaded body will no longer suffer from crack extension. This point is referred to as crack growth instability and specifies the onset of crack growth. However, no general specification about the interval of crack extension is provided. Further, if a crack of length $2a$ in an infinite plate is considered under tensile load of σ_0 , (2.50) becomes (see e.g. Gross and Seelig, 2011)

$$0 = \mathcal{G}_c - \frac{\sigma_0^2 \pi a}{E}, \quad (3.21)$$

for plane stress conditions. Accordingly, the critical stress for crack extension is of the order of $1/\sqrt{a}$, which allows for an infinitely high load once the initial crack length goes to zero. This behavior is inconsistent with the matter of fact that materials fail at a particular threshold loading. In other words, the energy criterion (2.49) does not account for crack initiation. The Griffith's energy criterion also does not give any specifications about the topology of crack evolution, meaning that generally the direction of crack extension or crack branching can not be predicted. In summary, Francfort and Marigo, 1998 motivate the need for their variational model of brittle fracture by maintaining different objections regarding Griffith's theory in terms of the

- ↔ unspecified period of crack growth,
- ↔ the need of an preexisting crack,
- ↔ the unspecified crack evolution.

Their work provides a key ingredient of the phase field model presented in the following sections and its basic content may therefore be reviewed at this point. The fundamental

assumption of this work is the postulate of the global minimum of the total energy of a potentially cracked body. The energy to minimize at every time of an elastic body (see Figure 3.3) represented by a domain with interior Ω , boundary $\partial\Omega$ and potential crack set Γ under the prescribed loading $\hat{\mathbf{u}}$ is defined as

$$E(\Gamma, \hat{\mathbf{u}}) = E_d(\Gamma, \hat{\mathbf{u}}) + E_s(\Gamma). \quad (3.22)$$

The second term in (3.22) refers to the energy of the cracks in the sense of Griffith. This contribution is proportional to the crack length for the two dimensional case and to the crack surface in the case of three dimensions, respectively. Accordingly, the crack energy is formulated by

$$E_s(\Gamma) = \int_{\Gamma} \mathcal{G}_c(\mathbf{x}) \mathcal{H}^{d-1}(\mathbf{x}) \, d\Gamma, \quad (3.23)$$

where the critical energy release rate is a function of the location \mathbf{x} to account for the general case. The crack surface is represented by the $(d-1)$ -dimensional Hausdorff measure $\mathcal{H}^{d-1}(\mathbf{x})$, which is a general measure for hypersurfaces ($d \geq 0$). However, for the present case, it can conveniently be considered as the crack length or surface, respectively. In contrast, the first part of (3.22) represents the elastic energy of the bulk material. Francfort and Marigo, 1998 focus on small deformations and linear elasticity with an elastic energy density W for points within $\Omega \setminus \Gamma$. In order to ensure that at every time a minimum of the total energy is attained, the bulk energy is formulated as the upper lower bound

$$E_d(\Gamma, \hat{\mathbf{u}}) = \inf_{\mathbf{u} \in \mathcal{C}(\Gamma, \hat{\mathbf{u}})} \int_{\Omega_{\Gamma}} W(\boldsymbol{\varepsilon}(\mathbf{u})) \, dV, \quad (3.24)$$

of all displacement fields \mathbf{u} associated with the set of admissible displacement fields \mathcal{C} , which in turn depends on the external loads and also on the current crack pattern. According to these definitions and assuming a prescribed displacement field $\hat{\mathbf{u}}$, the energy E_s will monotonically increase with an evolution of the crack Γ and the bulk energy E_d will monotonously decrease with Γ as the strain energy is released within $\Omega_{\Gamma} = \Omega \setminus \Gamma$. In order to obtain the time evolution $\Gamma(t)$ as a response to a load $\hat{\mathbf{u}}(t)$ the principal of global energy minimization is used. This means that the one state of the displacements $\mathbf{u}(\mathbf{x}, t)$ and the crack set is found among all admissible states, which minimizes the total internal energy

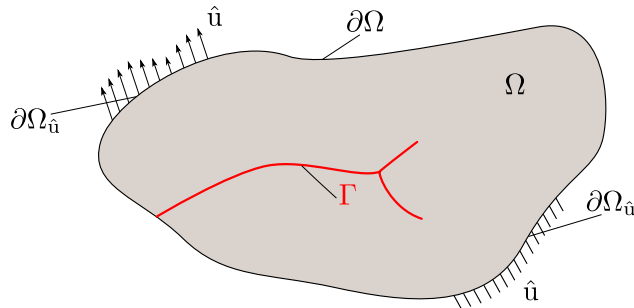


FIGURE 3.3: Illustration of open domain as base for the variational formulation of brittle fracture with interior Ω and boundary $\partial\Omega$.

(3.22). Considering a monotonically increasing load the model demands for

- (i) an increase of $\Gamma(t)$ with time and that $\Gamma(t) = \Gamma_0$ for $t < 0$, where Γ_0 is the initial state, which is also allowed to be zero,
- (ii) $E(\Gamma(t), \hat{u}(t)) \leq E(\Gamma, \hat{u}(t))$, where Γ is a potential alternative crack with $\Gamma \supset \Gamma(t_\lambda)$ with t_λ denoting an arbitrary state previous of t , and also
- (iii) $E(\Gamma(t), \hat{u}(t)) \leq E(\Gamma(t_\lambda), \hat{u}(t))$

to be respected by the crack evolution. The condition (i) prevents cracks from healing, as it requires Γ to increase with time or load, respectively. The actual postulation of the global energy minimum is prescribed by the condition (ii). The latter condition (iii) may in the first place seem rather redundant with respect to (ii). But it is very important as otherwise the solution is not ensured to be unique, or in other words, multiple cracks could be found, which fulfill (ii). With the conditions above, several properties of the variational model can be shown. They are important to discuss due to the connection to Griffith's energy considerations in terms of fracture and also to underline the abilities to go beyond the known restrictions of this theory. In this concern, it is desisted from providing the respective proofs, as these are very extensive and would lead away from the scope of the present work. Instead, the properties are summarized in the following categories.

Comparison to Griffith's theory

The variational model for brittle fracture satisfies Griffith's law. From a consequence of (ii) it can be shown that for a crack $\Gamma(t)$ the condition

$$-\left. \frac{dE_d}{dl} \right|_{l(t)} \leq \mathcal{G}_c \quad (3.25)$$

holds for a general state of the crack length $l(t)$ during crack evolution. Further, no variation of $l(t)$ is possible as long as (3.25) is satisfied in the strong sense ($<$ instead of \leq). A further consequence of the above condition is the conservation of energy during a crack jump. In other words, the release of strain energy with respect to the change in crack length during a crack jump is equal to the critical energy release rate. Accordingly, this property extends Griffith's theory, since crack evolution is described even when the energetic criterion for extension is reached.

Crack initiation and failure

In contrast to Griffith's theory the model includes the initiation of a crack as it can be shown that cracks have to appear within finite time. Furthermore, Γ will extend until the complete release of strain energy, which can be referred to as an incident of failure.

Characteristics of crack propagation

Besides continuous crack growth, which limits the crack growth intervals to infinitesimal time steps the introduced framework also includes the description of so-called brutal crack extension. The latter refers to abrupt jumps of the crack tip front. The authors further formulate a criterion that decides, which crack growth characteristic occurs. In this concern, the character of the bulk energy in terms of convexity is decisive. But also the strength of singularities of the displacement field within $\Omega \setminus \Gamma_0$ at special points like for instance crack tips or at non-smooth points on $\partial\Omega$. For weak singularities, e.g. sharp notches, only brutal

crack growth occurs according to the model. As explained above, Griffith's theory fails in predicting crack initiation.

In conclusion of this section, it can be stated that the variational formulation of brittle fracture proposed in Francfort and Marigo, 1998 provides a largely comprehensive framework for the description of cracking in brittle materials. Its value becomes especially clear when keeping in mind all the characteristics of cracking that are included in this framework, namely crack initiation, prediction of crack growth direction under arbitrary load states, and also rupture. Even if the revolutionary work of Griffith, 1921 provides a very elegant theory connecting irreversible processes associated with the formation of crack surfaces to the principle of energy conservation or the change in elastic strain energy, to handle cracks, additional criteria or paradigms are needed. As such, Leguillon, 2002 illustrates its constraints in predicting crack initiation at a sharp notch. He also points out contradictions regarding the strength criterion, which predicts crack initiation for any load due to the singularity in the stress field. Accordingly, an onset criterion is derived containing both strength and toughness bounds. In contrast, the global minimization of the total energy (3.22) also yields states in favor of crack initiation. A similar statement applies to crack path prediction. Different approaches have been proposed dealing with the issue of crack evolution under arbitrarily mixed mode loading. Famous contributions are the maximum tangential stress criterion proposed by Erdogan and Sih, 1963, the criterion of local symmetry proposed by Goldstein and Salganik, 1974, or the minimum strain energy density criterion, which is also referred to as S-criterion proposed by Sih, 1972. The aim of the introduced variational model for brittle fracture is to find the one crack pattern among all others that for every time ensures a minimum of the total energy. Accordingly, no additional criterion is needed for the determination of crack extension direction under arbitrary load situations. All these elegant features underline the general character of this modeling paradigm. This, however, leads to a crucial disadvantage of the model. It is simply not possible by analytical methods to find the solution of such minimization problems except for a small number of examples. It must further be outlined that the model presumes no force boundary conditions to ensure the above properties. Therefore, the basic model is something considered to be rather theoretical. Nevertheless, the general energy minimization principle is convincing for many applications. The variation formulation calls for a practical and general solution strategy. This provides the basis for the phase field modeling approach as will be outlined in the following sections.

3.2.2 Regularization of Free Energy

The modeling approach illustrated above provides a theoretical basis for the prediction of crack nucleation and extension in brittle materials. However, a brute force search for the optimal crack pattern is almost impossible. This theory misses a reliable framework for its practical application to arbitrary problems. In that concern a necessary basic step is the regularization of the total internal energy (3.22) to avoid jump discontinuities and obtain appropriate fields, that can be employed within numerical solution techniques. Such a formulation is provided by the regularization of (3.22). The number of studies from different researchers to solve this issue very impressively illustrates the general relevance of the question. In this regard one may begin with the approach of Mumford and Shah, 1985 for image segmentation. This field is concerned with the partitioning of a digital image to detect segments. Accordingly, every part of the image may be assigned to an object and

boundaries between different objects can be detected. In that regard, Mumford and Shah, 1985 proposed to transfer the problem of image segmentation to the minimization of the functional

$$\mathcal{G}(f, \Gamma) = \int_{\Omega \setminus \Gamma} \left(l_1(f - g)^2 + |\nabla f|^2 \right) dV + l_2 \mathcal{H}^{d-1}(\Gamma) \quad (3.26)$$

with the image g (set of pixels) in an open bounded domain Ω , the smoothed image f , the $(d-1)$ -dimensional volume of the boundary $\Gamma \subset \Omega$ and the parameters $l_1 > 0$ and $l_2 > 0$ in order to obtain f and Γ . By means of this functional, Ambrosio and Tortorelli, 1990 developed a method for the minimization of the general class of functionals of the type

$$\mathcal{F}(f, \Gamma) = \int_{\Omega \setminus \Gamma} f(\mathbf{x}, f, \nabla f) dV + \int_{\Gamma} \varphi(\mathbf{x}, f^+, f^-, n) d\mathcal{H}^{d-1} \quad (3.27)$$

that suffer from the issue of jump discontinuities. In (3.27), f^+ and f^- are the lines of f on the edges of Γ . Their approach considers the class of so-called special bounded variational functions (see e.g. De Giorgi et al., 1989, Ambrosio, 1990). These functions allow for jump discontinuities in f . Using this functions the functional (3.26) can be transferred to the weak functional

$$G(f) = \int_{\Omega} \left(l_1(f - g)^2 + |\nabla f|^2 \right) dV + l_2 \mathcal{H}^{d-1}(S_f) \quad (3.28)$$

with the set of jump discontinuities S_f of f . It was shown by De Giorgi et al., 1989, that a minimizer f of (3.28) also minimizes (3.26). However, even if the "troublemaker" Γ is removed from (3.26), the computation of minimizers of G is still not free of difficulties as the location of the jump set S_f is a priori unknown. To overcome this issue Ambrosio and Tortorelli, 1990 proposed to approximate the functional G by elliptical functionals G_c , for which Γ -convergence can be shown. This important property, comprehensively described in De Giorgi and Dal Maso, 1983, of a sequence of functionals $G_c(f_c, z_c)$, with a auxiliary variable $z_c \in [0, 1]$ and an regularization parameter c means that

$$\lim_{c \rightarrow 0} G_c(f_c, z_c) = G(f), \quad (3.29)$$

holds. This can briefly be illustrated by:

$$\text{if } (f_c, z_c) \text{ minimize } G_c, \text{ then the limit } f_c \rightarrow f \text{ minimizes } G \quad (3.30)$$

In other words, in the limit, meaning if $c \rightarrow 0$, minimization of G_c is equivalent to the minimization of G . The bridge of this approach to the variational formulation of brittle fracture was initially formed by Bourdin et al., 2000 and further extended in Bourdin, 2007. Within these studies, the internal energy (3.22) for an elastic material is approximated by the functional

$$E_c(\mathbf{u}, z) = \int_{\Omega} (z^2 + \eta) W(\nabla \mathbf{u}) dV + \mathcal{G}_c \int_{\tilde{\Omega} \setminus \partial \Omega_N} \left(\frac{(1-z)^2}{4c} + c |\nabla z|^2 \right) dV, \quad (3.31)$$

where $\partial\Omega_N$ refers to the part of $\partial\Omega$, which is free of boundary conditions and $\tilde{\Omega}$ is an extended domain, which is considered to ensure traction free boundaries (see. Bourdin et al., 2000 for technical details). This formulation is a slight variation of a functional proposed in Ambrosio and Tortorelli, 1990 for the approximation of the Mumford-Shah problem (3.26). For the elastic antiplane shear case, where the strain energy density is described by

$$W = \frac{1}{2}\mu|\nabla\mathbf{u}|^2, \quad (3.32)$$

(3.31) becomes the functional proposed in Ambrosio and Tortorelli, 1990 to treat the Mumford-Shah image segmentation problem for which Γ -convergence was proven. Further, it is proven in Bourdin et al., 2000 that the regularizations for bulk and surface energies of (3.31) converge to particular contributions of the strong functional (3.22). However, in terms of discretization of this total energy it is important to ensure the characteristic length of the discretization of the numerical method to be kept small compared to the regularization parameter c . In Bourdin, 2007 finite elements were used. Even if with (3.31) a regularization is provided, which can be adopted within numerical solution techniques, the practical solution is still not an unproblematic task as E_c reveals a convex character for the set of variables \mathbf{u} and z only separately. The proposed solution scheme in Bourdin, 2007 is a sequence of two one field optimization problems to be solved subsequently. The following procedure describes this so-called Alternate Minimization process for a time step t_i :

1. Initialize \mathbf{u} and z as \mathbf{u}_{i-1} and z_{i-1}
2. Alternate Minimization (iteration)
 - 2a fix z as z^{p-1} and compute \mathbf{u} as
 $\mathbf{u}^p = \operatorname{argmin}(E, \mathbf{u})$
 - 2b fix \mathbf{u} as \mathbf{u}^p and compute z as
 $z^p = \operatorname{argmin}(E, z)$
3. as long as $\|z^p - z^{p-1}\| > \text{error}$, $p = p + 1$ and goto 2., otherwise $\mathbf{u}_i \leftarrow \mathbf{u}^p$ and $z_i \leftarrow z^p$

This algorithm ensures first order optimality conditions for \mathbf{u} and z . However, as shown in Bourdin, 2007, displacement states $(\mathbf{u}(\mathbf{x}, t), z(\mathbf{x}, t))$ that satisfy the optimality conditions may not in general be considered as global minimizers. Accordingly, additional checks are required to ensure that the solution provided by the Alternate Minimization algorithm fulfills second order optimality.

3.3 Phase field Modeling of Brittle Fracture

Up to this point of the current chapter, the very basic ingredients of a phase field model for brittle fracture were introduced. On the one hand, the general characteristics of the phase field modeling philosophy were illustrated and the benefits of field quantities and an order parameter were presented. The derivation of a proper evolution equation (3.6) for this order parameter was described in terms of two different perspectives, one by formal variation and another more tangible motivated by the theory of micro forces in order to generalize the framework. On the other hand, a basic formulation of the free energy functional properly

describing the process of fracture was introduced as the second crucial component for a phase field model dealing with fracture. It is now in the focus of the present section to illustrate the combination of these ingredients, which can be referred to as a basic phase field model for brittle fracture, presented by Kuhn and Müller, 2010. This model is of fundamental character and will therefore be discussed to illustrate the basic concepts, the properties, and also its constraints in order to motivate subsequent modifications, which are in the focus of the present work. Accordingly, this will be in the focus of the subsequent sections. To provide a comprehensive state of the art, several further models dealing with different subtopics such as dynamic fracture and ductile fracture are briefly outlined.

3.3.1 The Kuhn-Müller Phase Field Model

As previously stated, the variational formulation for brittle fracture does not provide a proper approach for practical usage within computational methods. This is simply due to the required minimization with respect to discontinuous fields. The key idea of the phase field model from Kuhn and Müller, 2010 is to use the regularization of the total internal energy introduced above as the free energy of a phase field model. Accordingly, the specific form of the energy functional (3.3) becomes

$$F[\boldsymbol{\varepsilon}(\mathbf{u}, t), s(\mathbf{x}, t)] = \int_{\Omega} \underbrace{(g(s) + \eta) \frac{1}{2} \boldsymbol{\varepsilon} : [\mathbb{C} \boldsymbol{\varepsilon}]}_{\psi_e} + \underbrace{\mathcal{G}_c \left(\frac{(1-s)^2}{4\epsilon} + \epsilon |\nabla s|^2 \right)}_{\psi_c} dV, \quad (3.33)$$

with the specific bulk energy ψ_e and the specific interfacial energy ψ_c representing the contributions of energy consumed by deformation work and crack extension, respectively. The order parameter is designated as $s \in [0, 1]$, with $s = 1$ representing the intact state of the material, and $s = 0$ representing the broken material or crack. The first term, namely ψ_e , in (3.33) is basically the elastic energy density within a small deformation setup, expressed by the linearized strain tensor $\boldsymbol{\varepsilon}$. The tensor \mathbb{C} is the fourth order stiffness tensor. Obviously, the second term, namely ψ_c , is the regularization of the crack set proposed in Bourdin et al., 2000. This part acts as diffuse, or as a smeared representation of cracks within a body. Thus, the discontinuous formulation proposed by Marigo, 1985 is transferred into a diffuse interface energy. Figure 3.4 illustrates the basic approximation scheme of the fracture problem by means of the phase field framework.

The product of the strain energy density with $(g(s) + \eta)$ incorporates a degradation of the stiffness within cracked areas, where $g(s)$ is a degradation function. It may be anticipated at this point, that the parameter η acts as a kind of residual stiffness parameter to ensure numerical stability, where $0 < \eta \ll 1$ is demanded. The term stiffness degradation becomes obvious once the stresses are derived from the potential by

$$\boldsymbol{\sigma} = \frac{\partial \psi}{\partial \boldsymbol{\varepsilon}} = (g(s) + \eta) \mathbb{C} \boldsymbol{\varepsilon}, \quad (3.34)$$

in which hyperelastic material behavior is presumed. Further, as at this point a proper energy potential depicting a potentially fractured body is given, the law for an evolution with respect to the time can be formulated bringing together the general law for phase

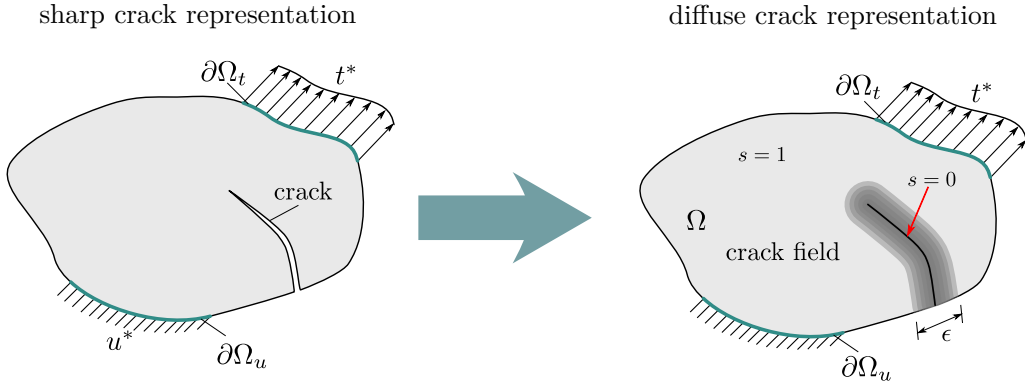


FIGURE 3.4: Schematic illustration of approximation of fracture problem by means of phase field modeling: left, body with real sharp crack; right, diffuse representation of crack introducing a continuous crack field.

transformation of (3.20) and the total energy potential from (3.33) to yield a Ginzburg-Landau type evolution equation

$$\frac{ds}{dt} = -M \frac{\delta}{\delta s} (\psi_e + \psi_c) = -M \left\{ \frac{1}{2} \frac{dg}{ds} \boldsymbol{\varepsilon} : [\mathbb{C}\boldsymbol{\varepsilon}] - \mathcal{G}_c \left(\frac{1-s}{2\epsilon} + 2\epsilon \nabla \cdot \nabla s \right) \right\}, \quad (3.35)$$

where the scalar mobility $M = \frac{1}{\lambda} > 0$ is introduced now as a constant value for the viscosity. With this kinetic control parameter approaching infinity, quasi static conditions are approximated. The stationary limit is specified by a vanishing functional derivative $\delta\psi/\delta s = 0$.

Characteristic functions

As mentioned above, the potential ψ consists of strain energy density representing the bulk potential and the crack energy density representing the interfacial part. The crack potential ψ_c itself consists of two parts. The non-local part characterized by the spatial gradient of s and the local part, characterized by the monotonous function $(1-s)^2$. The non-local contribution ensures smooth phase transitions, whereas the local part has crucial impact on the model properties (see e.g. Kuhn et al., 2015). In contrast to the double well or double obstacle function (see. section 3.1.1), which was applied e.g. in Karma et al., 2001, the local part yields a barrier between two phases and, irreversibility of the fracture process is not generally ensured by this monotonous potential. Nonetheless, there are several benefits provided by this form of a quadratic potential. First of all one has to mention the mathematical property of Γ -convergence, which was proven for the monotonous potential of (3.33). Secondly, as the plot of the monotonous potential in Figure 3.5b) clearly shows, the opposite phases $s = 1$ and $s = 0$ reveal unique states of the corresponding potential of intact and broken material.

In contrast, the double well potential yields equal values for the opposite phases (see Figure 3.1a)). Therefore it occurs, that the crack field simply becomes wider, or in other words the crack grows "fat" due to an energetic equivalence. The function $(1-s)^2$ reveals a minimum for $s = 1$. This is a quite accommodating property, as it consequently yields a

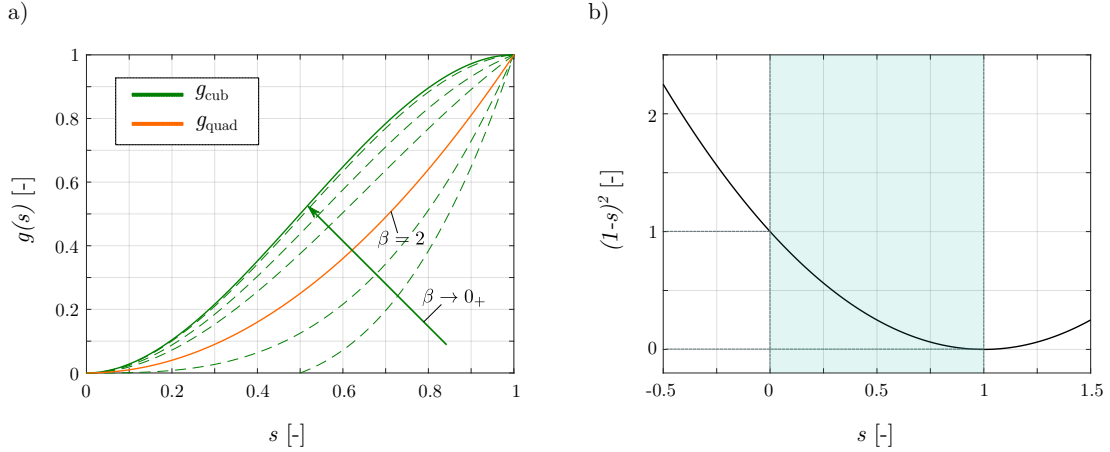


FIGURE 3.5: Illustration of important functions characterizing the fracture phase field model behavior: a) different degradation functions; b) monotonous non-local crack potential.

minimum for the total energy for the unloaded state, or at unloaded regions, respectively. Accordingly, this property constitutes a natural constraint $s \leq 1$ for the phase field, which for an application of the double obstacle potential would have to be integrated explicitly.

The second characterizing function in terms of the mechanical behavior of the phase field fracture model is, as mentioned above, the function $g(s)$ that describes the degradation of the stiffness within fractured or fracturing regions. Within the initial model Kuhn and Müller, 2010 the quadratic degradation function

$$g_{\text{quad}}(s) = s^2 \quad (3.36)$$

is utilized. Besides the quadratic approach, a variety of different degradation functions have been proposed. These approaches differ mainly in the polynomial degree. As such e.g. cubic and quartic functions were investigated in Kuhn et al., 2015. Additionally, parameterized functions with single parameters as e.g. in Borden et al., 2016, or multiple parameters as e.g. in Sargado et al., 2018 have since then been applied to fracture phase field models, as through the parameterization a family of degradation functions is provided. Further, polynomials of up to even fifth degree were proposed within a study of phase field models for solidification conducted by Wang et al., 1993. In Voyiadjis and Mozaffari, 2013 these functions were utilized as degradation function for a phase field model for damage evolution. All the mentioned proposals for the modeling of the phase transition, or the stiffness decrease in case of fracture, respectively, reveal different properties. Some of them will be briefly outlined. The quadratic approach (3.36) was also proposed within Ambrosio and Tortorelli, 1990; Bourdin et al., 2000 and Bourdin, 2007. This function, as the respective line plot of Figure 3.5a) illustrates, satisfies the minimal set of requirements, which are

$$g(0) = 0, \quad g(1) = 1, \quad \text{and} \quad g'(0) = 0. \quad (3.37)$$

In addition, monotony and continuous differentiability are required. The first two requirements are obvious and simply ensure the complete release of stiffness (despite the

mentioned residual stiffness $\eta\mathbb{C}$) for broken areas ($s = 0$) and vice versa for regions of intact material. In contrast, the reason for the last condition, for the derivative may not be clear in the first place. However, its significance becomes meaningful considering the evolution law (3.35), since $g'(0) \neq 0$ would continue to drive the evolution of s even for a broken material. The condition $g'(1) = 0$ is satisfied by the cubic and quartic functions from Kuhn et al., 2015, and also by the parameterized cubic degradation function

$$g_{\text{cub}}(s) = \beta(s^3 - s^2) + 3s^2 - 2s^3 \quad (3.38)$$

for a parameter $\beta \rightarrow 0$. The degradation function (3.38) was proposed in Borden et al., 2016. With this property, the initial state $s = 1$ is generally a solution of (3.35) and stiffness decrease of the material does not start before any load is applied, which is the case for functions with $g'(1) > 0$ as e.g. (3.36). Accordingly, in terms of brittle fracture a better approximation is provided by functions with $g'(1) = 0$. Unfortunately, there is also a disadvantage. It was shown in Kuhn et al., 2015, that when using these functions, even once a critical load is applied it is likely, that the phase field remains one, as this state is, among others, still an admissible solution. However, since (3.38) provides a family of functions, this issue can be overcome by choosing the parameter β slightly above 0. The dashed lines in Figure 3.5b) illustrate the family of degradation functions provided by (3.38). It is also noteworthy, that for $\beta = 2$ the original quadratic function (3.36) is obtained. A meaningful interval for β is $0 \leq \beta \leq 3$, as parameters $\beta > 3$ and $\beta < 0$ yield curves, which are not monotonously increasing in the interval $0 \leq s \leq 1$ (as the lowest of the dashed curves in Figure 3.5a) shows exemplary).

From an uniaxial analysis, one finds the critical stress-strain states corresponding to the onset of localization of the phase field. For the model resulting from (3.36) this state is given by

$$\sigma_c^{\text{quad}} = \frac{9}{16} \sqrt{\frac{E\mathcal{G}_c}{6\epsilon}}, \text{ and } \varepsilon_c^{\text{quad}} = \sqrt{\frac{\mathcal{G}_c}{6E\epsilon}} \quad (3.39)$$

and in contrast the model resulting from the degradation function (3.38) with $\beta = 0$ yields the critical stress-strain state

$$\sigma_c^{\text{cubic}} = \frac{81}{50} \sqrt{\frac{E\mathcal{G}_c}{15\epsilon}}, \text{ and } \varepsilon_c^{\text{quad}} = \sqrt{\frac{5\mathcal{G}_c}{27E\epsilon}}. \quad (3.40)$$

Accordingly, the state of critical loading regarding crack nucleation is effected by the type of degradation function. For this reason and due to the differences in the general mechanical behavior until fracturing, the choice of the degradation function may also be interpreted as a material characterization.

Modeling irreversibility of fracture

The discussion of this paragraph deals with the fact, that cracks occurring within a material can not heal. However, the Ginzburg-Landau evolution equation does indeed allow for a recovery of the crack field s from any state. Considering the dissipation inequality (3.17) together with (3.18) and (3.19) yields the inequality $0 \geq -\Lambda\dot{\phi}^2$. Accordingly, with the evolution equation (3.35) the total dissipation energy for the described phase field

formulation is expressed by

$$\mathcal{D} = \int_{\Omega} \frac{\dot{s}^2}{M} dV \geq 0, \quad (3.41)$$

which illustrates that equal energy dissipation occurs for a decrease as well as an increase of the phase field. Further, in (3.33) there is no energetic barrier incorporated by the bulk potential as it would be for the double well potential. Accordingly, additional restrictions must be considered to avoid crack healing for instance during unloading. In order to overcome this issue, Bourdin et al., 2000 proposed to restrict the crack field once fully broken. In terms of the present phase field model this was accomplished in the model form Kuhn and Müller, 2010 by applying Dirichlet type boundary conditions at fully broken regions, meaning that $s(\mathbf{x}, t) = 0$ for all times $t \geq t_{\text{break}}$, where t_{break} defines the time for which $s(\mathbf{x}, t)$ has vanished completely. In regard of (3.41) and (3.35) this leads to a kinetic coefficient to be given by

$$M = \begin{cases} M^* & \text{for } s > 0 \\ 0 & \text{for } s = 0. \end{cases} \quad (3.42)$$

This strategy is quite convenient when it comes to simulation. In finite elements the conditions can simply be implemented by locking the respective nodes on the element level. However, it may be noticed, that by applying this strategy, the phase field can recover as long as it has not reached the value zero. Another way of prohibiting crack healing was proposed in Miehe et al., 2010b. In contrast to Bourdin's formulation, the phase field is treated as a damage variable in this work and accordingly a stronger condition applies to the rate of the phase field by enforcing

$$\dot{s} \geq 0, \quad (3.43)$$

which does not allow for any regeneration. Thus the kinetic constant is given by

$$M = \begin{cases} M^* & \text{for } \frac{\delta\psi}{\delta s} > 0 \\ 0 & \text{otherwise.} \end{cases} \quad (3.44)$$

This strategy is referred to as damage like formulation.

3.3.2 Alternative Models and Extensions

Certainly, the self organizing characteristic in terms of the evolution of crack patterns enabling a kind of natural tracking of crack propagation has gained the attention of many researchers and accordingly a number of different models have been proposed within the last two decades. A variety of fracture problems have been studied in terms of phase field modeling. For instance, the models presented by Kuhn et al., 2016, Miehe et al., 2016, Aldakheel et al., 2018a or Borden et al., 2016 treat ductile fracture. Contributions dealing with dynamic fracture were presented by Schlüter et al., 2014 and models concerned with the issue of cohesive fracture were proposed by Verhoosel and Borst, 2013 or Kuhn and Mueller, 2016. The basic framework for these specific models, however, is always provided by one of the contributions dealing with the original case of brittle fracture, namely Miehe et al., 2010b, Amor et al., 2009, or Borden et al., 2014. The latter two

in general also adopt Bourdin's total energy regularization, where in contrast the first one is based on thermodynamical arguments and principles of damage mechanics. The damage like character of this model is also manifested by a contrary definition of the phase field variable s_d which corresponds to damage mechanics with 1 indicating fully damaged or broken material and 0 indicating undamaged or intact material, respectively. Hence, $s = s_d - 1$ and this approach may, in some instances, be viewed as an alternative framework. However, the crucial difference of these approaches with respect to the Kuhn and Müller, 2010 approach is, that their basic formulation includes a distinction in the general treatment of tensile and compressive loads. Such a distinction becomes relevant in some situations, as the strain energy is a quadratic form and tension and compression result in the same value of the potential. Due to the divergent response of the respective phase field models with respect to the load characteristic, these models are also referred to as being "anisotropic". However, as this term may be somehow misleading in this concern, it shall be anticipated, that anisotropy solely applies to the phase field evolution and the material tensor is not affected. Within both frameworks the strain energy density of a fully intact body is split such that

$$\psi_e = \psi_e^+ + \psi_e^-, \quad (3.45)$$

where ψ_e^+ and ψ_e^- represent the contributions caused by tension and compression, respectively. The definition of these two parts deviates and will be introduced separately in the following.

Volumetric-deviatoric split

Generally, Bourdins regularization of the total internal energy (3.31) is also the basis for the mode proposed by Amor et al., 2009. The strain energy density is considered as an additive decomposition

$$\psi_e(\boldsymbol{\varepsilon}) = \psi_{ev} + \psi_{ed} = \frac{K}{2} \text{tr}^2(\boldsymbol{\varepsilon}) + \mu \boldsymbol{\varepsilon}_D^2, \quad (3.46)$$

with a contribution caused by the change in volume namely ψ_{ev} and a contribution caused by distortion namely ψ_{ed} . The factor $K = \lambda + 2\mu/3$ is referred to as bulk modulus. The volume energy density part ψ_{ev} is further split into a tension and a compression part such that

$$\psi_{ev} = \frac{K}{2} \left\langle \text{tr}(\boldsymbol{\varepsilon}) \right\rangle_+^2 + \frac{K}{2} \left\langle \text{tr}(\boldsymbol{\varepsilon}) \right\rangle_-^2, \quad (3.47)$$

applying the operators $\langle \cdot \rangle_+ = \max(0, \cdot)$ and $\langle \cdot \rangle_- = \min(0, \cdot)$. The core difference with respect to (3.33) is now, that the degradation function acts on ψ_{ed} and the tension associated contribution of ψ_{ev} . Accordingly the potential becomes

$$F_e^{\text{VD}} = \int_{\Omega} \underbrace{(g(s) + \eta) \left(\frac{K}{2} \left\langle \text{tr}(\boldsymbol{\varepsilon}) \right\rangle_+^2 + \mu \boldsymbol{\varepsilon}_D^2 \right)}_{\psi_e^+} + \underbrace{\frac{K}{2} \left\langle \text{tr}(\boldsymbol{\varepsilon}) \right\rangle_-^2}_{\psi_e^-} dV. \quad (3.48)$$

Using this potential, negative mean stress has no effect on the minimization, as the crack energy is no longer in competition with it. This becomes apparent when the corresponding

evolution equation

$$\dot{s} = -M \left\{ \frac{1}{2} \frac{dg}{ds} \left(\frac{K}{2} \langle \text{tr}(\boldsymbol{\varepsilon}) \rangle_+^2 + \mu \boldsymbol{\varepsilon}_D^2 \right) - \mathcal{G}_c \left(\frac{1-s}{2\epsilon} + 2\epsilon \nabla \cdot \nabla s \right) \right\}, \quad (3.49)$$

is considered. Hence, cracking due to pressure is avoided by the energy functional, whereas cracks caused by tensional loading can still be beneficial regarding an energy minimization and will therefore occur.

Spectral split

A slightly different approach was introduced by Miehe et al., 2010b. The split of the total strain energy density ψ_e is based on the spectral decomposition of the linearized strain tensor

$$\boldsymbol{\varepsilon} = \sum_i \varepsilon_i \cdot (\mathbf{n}_i \otimes \mathbf{n}_i), \quad (3.50)$$

with the eigenvalues ε_i and the corresponding eigenvectors \mathbf{n}_i . Alternatively to (3.46) the strain energy can be decomposed as

$$\psi_e = \frac{\lambda}{2} \text{tr}(\boldsymbol{\varepsilon})^2 + \mu \boldsymbol{\varepsilon} : \boldsymbol{\varepsilon}. \quad (3.51)$$

With (3.50) the potential becomes

$$\psi_e = \frac{\lambda}{2} \left(\left\langle \sum_i \varepsilon_i \right\rangle_+^2 + \left\langle \sum_i \varepsilon_i \right\rangle_-^2 \right) + \mu \left(\sum_i \langle \varepsilon_i \rangle_+^2 + \sum_i \langle \varepsilon_i \rangle_-^2 \right) \quad (3.52)$$

and for the corresponding energy functional only positive components of (3.52) become degraded in order to avoid cracking under compression.

Generally, these two approaches are quite similar as for instance in case of hydrostatic compression no driving terms of strain energy enter the evolution equation. However, the behavior deviates in situations where the three principal strains are negative but different in magnitude. In this case the split based on spectral decomposition from Miehe et al., 2010b reveals zero contribution of strain energy in the evolution equation as in contrast to the volumetric deviatoric split proposed in Amor et al., 2009 has a contribution due to the deviatoric part of the energy density.

Chapter 4

Modifications of the Phase Field Model for Brittle Fracture

The basic phase field model for brittle fracture introduced within the previous chapter reveals many benefits in terms of simulative investigation of initiation and tracking of cracks. Furthermore, its methodical framework was proven to extend Griffith's theory (Griffith, 1921) as an essential pillar of fracture mechanics. In its presented form the formulation is restricted to cracking due to quasi static loading in homogeneous materials. Considering some practical cases of material failure of components in vehicles, construction machines, airplanes or similar engineering structures, cracks are as a matter of fact predominantly driven by cyclic loads (see Haibach, 2006), which addresses different failure mechanisms. Another aspect emerges by a general consideration of lightweight constructions since the application of thin walled structures is common for this development principle. The microstructure within such thin walled components can have an influence on crack patterns, as will be illustrated in the following section. Hence, turning the focus from a general observation and characterization of fracture to practical examples, where cracking plays a major role in terms of accessing loading capacity and operational capability, the need for enhancement of the phase field model becomes apparent. Although the phenomena of these different types of fracturing may be sufficiently characterized, it is certainly still a crucial issue how a respective enhancement of the proposed phase field method can be established in order to adequately picture the cracking behavior. In order to provide a comprehensive description this issue will be the focus of this chapter. The modifications will be motivated by detailed explanations regarding the phenomenological background and it will be shown how these particular effects are incorporated into the phase field fracture framework. In detail, two major modifications of the basic model will be outlined within this work, namely the field of cyclic fatigue crack growth and crack deflection within materials with anisotropic fracture resistance. The considerations of the chapter are restricted to the theory of the enhancement, a respective verification will be provided in chapter 6.2. Even if the basic model for the modifications is provided by the model from Kuhn and Müller, 2010 it will become clear that the proposed methods can also be incorporated within other basic models. Additionally, it may be outlined, that as within other modifications as for e.g. ductile materials (Kuhn et al., 2016) or cohesive fracture (Kuhn and Mueller, 2016), the enhancements do not change or effect in any concern the very principle of the phase field paradigm of the evolution governed by energy considerations.

4.1 Cracking of Materials with Anisotropic Fracture Resistance

4.1.1 Characterization of Crack Deflection

One modification of this work is concerned with the incorporation of a directional fracture toughness. First, it may be outlined, to which extent such materials change the extension direction and then an appropriate phase field model is introduced. According to Griffith, 1921 a crack starts to extend once the additional amount of infinitesimal surface energy

$$d\Gamma = \mathcal{G}_c da \quad (4.1)$$

can be balanced by the decrease of the potential energy relative to the infinitesimal crack extension. This holds as long as cracks in isotropic materials that do not show the introduced anisotropy are considered. The criterion assumes that the direction for the crack extension is known a priori. To overcome this issue, several additional criteria have been proposed to determine the direction for arbitrary loading situations. There is, for instance, the principle of local symmetry from Goldstein and Salganik, 1974 or the Maximum Energy Release Rate (MERR) criterion proposed in Erdogan and Sih, 1963 and Wu, 1978. The starting point of the latter criterion is the assumption of an energy release $\frac{d\Gamma}{da}$ as a function of the potential deflection direction φ (see Figure 4.1). As a key postulate it is assumed that once a respective load level is reached, the crack will grow in the direction maximizing the energy release, which requires

$$\left. \frac{\partial \mathcal{G}}{\partial \varphi} \right|_{\varphi_c} = 0 \quad \text{and} \quad \left. \frac{\partial^2 \mathcal{G}}{\partial \varphi^2} \right|_{\varphi_c} \leq 0 \quad (4.2)$$

for the extension direction φ_c . In this description, the onset of crack growth is defined by

$$\mathcal{G}(\varphi_c) = \mathcal{G}_c, \quad (4.3)$$

where \mathcal{G}_c is the material parameter measured in experiments without crack deflection. But it is exactly this assumption that is not true for a number of wrought products used in modern designing. In this regard, one may for example consider thin walled structures, which are produced by forming processes such as (hot/casting-)rolling or extruding. As illustrated in Figure 4.2a) for the (hot/casting-)rolling process and in Figure 4.2b) for

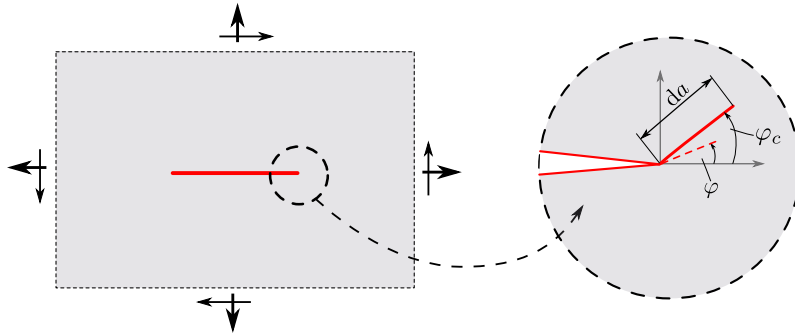


FIGURE 4.1: Schematic illustration of infinitesimal crack extension by an increment da in direction φ .

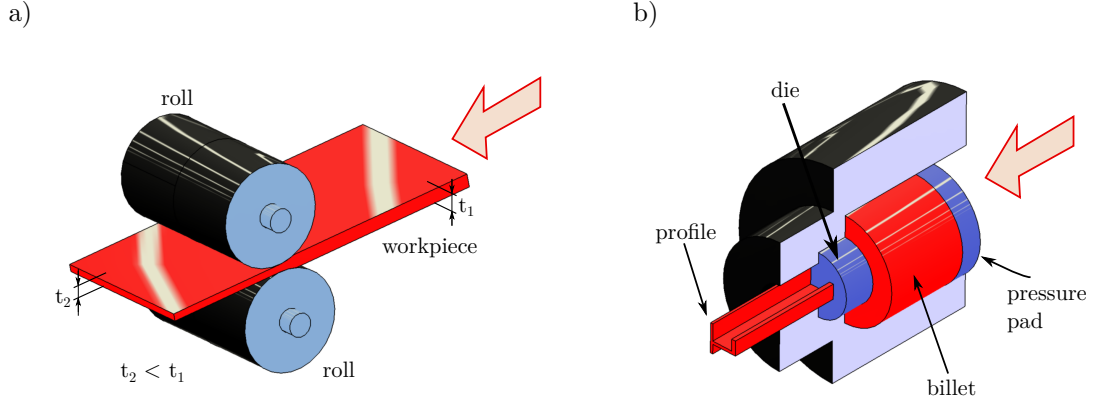


FIGURE 4.2: Illustration of two manufacturing processes for thin walled structures: a) rolling; b) extruding.

extruding the material is strongly deformed during these processes. As it was shown in several experimental studies, e.g. İriç and Ayhan, 2017, Moreno-Valle et al., 2019 or Das et al., 2017, such materials are likely to reveal a directional variation of the fracture toughness or critical energy release rate, respectively. This is caused by a deformation of the microstructure caused by the high plastic strains during such forming processes. For clarification, see the schematic illustration of a respective microstructure in Figure 4.3. The indicated crack paths in this figure illustrate transcrystalline crack growth in the left microstructure and intercrystalline crack growth in the right microstructure, respectively. The crucial property establishes the grain boundaries. The exact circumstances may still be an open field for discussion within the respective community, however, grain boundaries generally complicate the crack evolution within a polycrystalline material. Accordingly, a crack propagating in rolling/extrusion direction (RD) will have to cross a lower number of grain boundaries to reach a certain length compared to a crack propagating in the transverse direction (TD). Analogously, considering intercrystalline crack growth, a crack propagating in RD can follow a less torturous path to reach the same unidirectional length as a crack propagating in TD. In the general case, there is one direction prone for crack extension as it consumes less energy and accordingly

$$\mathcal{G}_c^{RD} < \mathcal{G}_c^{TD}. \quad (4.4)$$

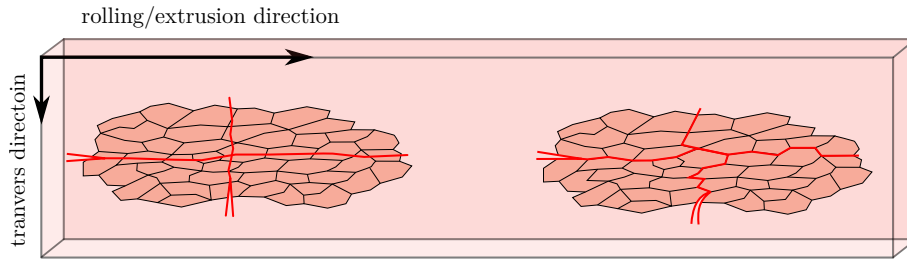


FIGURE 4.3: Schematic illustration of crack evolution (left: transcrystalline crack extension, right: intercrystalline crack extension) through elongated microstructure caused by forming processes.

Certainly it is not only these two directions that deviate, but the fracture toughness varies with the virtual crack direction. Accordingly, not only the release rate \mathcal{G} depends on the direction but also the material resistance \mathcal{G}_c . Following the suggestion of an elliptical interpolation (Kfourri, 1996) between \mathcal{G}_c^{RD} and \mathcal{G}_c^{TD} , the need for an additional criterion for the determination of the deflection direction becomes obvious. In this regard Figure 4.4 shows a comparison of a constant fracture toughness and the case of a twofold anisotropy. In order to overcome this issue Kfourri, 1996 proposed to consider the ratio $\mathcal{G}(\varphi)/\mathcal{G}_c(\varphi)$ and specify φ_c as the direction maximizing this ratio.

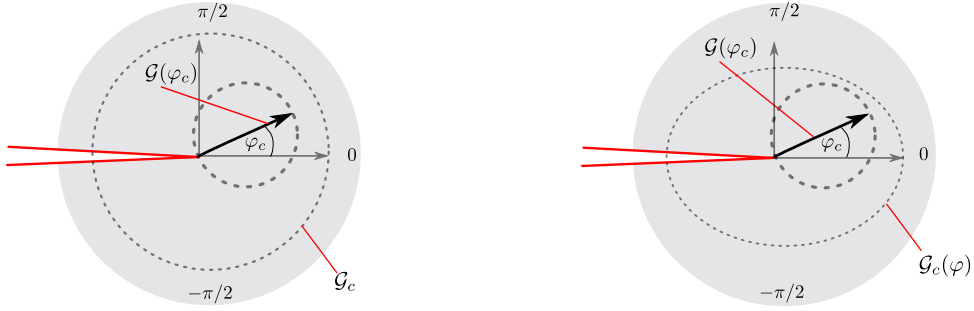


FIGURE 4.4: Schematic comparison of materials with fracture toughness constant w.r.t. angle and anisotropic materials regarding determination of crack extension direction.

4.1.2 Basic Modification

As outlined in the previous chapter, the original phase field model for brittle fracture Kuhn and Müller, 2010 considers an isotropic surface energy density

$$\psi_c = \mathcal{G}_c \underbrace{\left(\frac{(1-s)^2}{4\epsilon} + \epsilon |\nabla s|^2 \right)}_{\Gamma} \quad (4.5)$$

and hence can not account for the kind of a twofold anisotropy explained above. The phase field paradigm predicts the correct contribution for the field of the physical quantity in consideration as the one among all that minimizes the total energy. In case of fracture, the evolution may be interpreted as the continuous competition of strain energy and surface energy for their respective significance in order to minimize the total energy. Consequently, the key is to offer an opportunity for the surface energy not to consume too much energy relative to the crack evolution. If this is enabled for a specific direction of crack extension the surface energy density is modified anisotropic. Given (4.5), one may consider the straight forward approach in accordance to the (MERR)-criterion and assume the critical energy release rate as a function of the virtual cracking angle with

$$\psi_c(\varphi) = \mathcal{G}_c(\varphi)\Gamma. \quad (4.6)$$

This approach was studied in terms of phase field modeling by e.g. Li et al., 2015 or Hakim and Karma, 2009. Within the latter, the fourth order phase field model proposed by Borden et al., 2014 is utilized as the basic model and the crack's orientation φ is determined by

the normal vector

$$\mathbf{n}(\mathbf{x}, t) = \frac{\nabla s(\mathbf{x}, t)}{|\nabla s(\mathbf{x}, t)|}. \quad (4.7)$$

The vectors are oriented perpendicular to contours of the field $s(\mathbf{x}, t)$. This is shown by Figure 4.5, which illustrates a phase field crack within a 2d setting. At locations of $s = 0.9$ the vectors $\nabla s/|\nabla s|$ are indicated. However, defining the crack trajectory this way and introducing the critical energy release rate as $\mathcal{G}_c(\mathbf{n})$ is not free of problems. Within areas away of cracks and particularly for the fourth order phase field model (Borden et al., 2014) at $s = 0$, the gradient ∇s vanishes, which renders this scheme impractical. One may be able to fix this issue by imposing suitable restraints at relevant areas but this is extensive and conflicts with an implicit solution scheme as it is generally proposed for all simulations within the present work. Accordingly, instead of modifying the critical energy release rate it is better to consider the other relevant quantity of the surface energy density (4.5), namely the crack's regularization Γ . The non-local contribution of this quantity consists of the squared norm of the gradient ∇s . Considering the horizontal crack depicted in Figure 4.5 one obviously detects a significantly predominant number of vertical components of the vectors $\nabla s/|\nabla s|$. Thus consistently, an unidirectional crack produces a majority of gradients, that point in the perpendicular direction with respect to the crack orientation. If these gradients are modified such that they become energetically more expensive a directionality is established. In order to incorporate a respective weighting, the identity tensor in the non-local crack potential

$$\psi_e^{\text{nl}} = \mathcal{G}_c \epsilon \underbrace{\nabla s \cdot (\mathbf{1} \nabla s)}_{|\nabla s|^2} \quad (4.8)$$

is proposed in the present work to be substituted by an appropriate second order tensor Φ , that accounts for directionality. The new modified crack energy then reads

$$E_c = \mathcal{G}_c \int_{\Omega} \frac{(1-s)^2}{4\epsilon} + \epsilon \left[\left(\frac{\partial s}{\partial x} \right)^2 \Phi_{11} + 2 \frac{\partial s}{\partial x} \frac{\partial s}{\partial y} \Phi_{12} + \left(\frac{\partial s}{\partial y} \right)^2 \Phi_{22} \right] dV \quad (4.9)$$

within two dimensions. This equation reveals a possible weighting of the particular gradient contribution by the components Φ_{ij} . As the resistance against cracking is specified by these

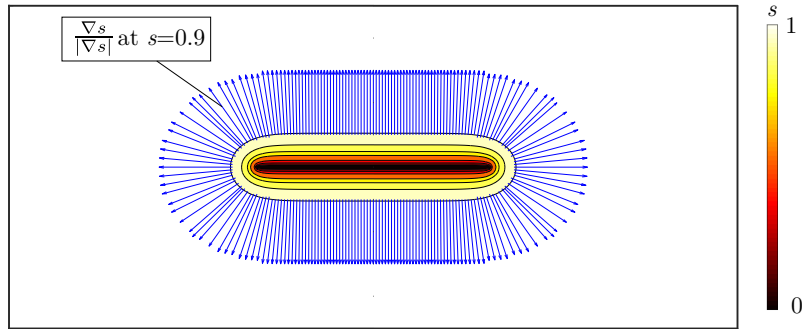


FIGURE 4.5: Contour plot of 2d phase field crack with indication of vectors $\nabla s/|\nabla s|$ for $s = 0.9$.

components, the tensor Φ may be specified as resistance tensor in the following. Still, it is not clear how this resistance tensor has to be designed in order to adequately picture the behavior of the materials described above. Therefore, an interpretation of the gradient ∇s can be given visually, plotting the non-local crack potential (4.8) in a $s, x-s, y-\psi_c^{\text{nl}}$ -coordinate system. The respective surface plot is depicted in Figure 4.6. In case of the basic potential (4.5) one obtains a symmetric paraboloid as shown in Figure 4.6a). Considering a section at an arbitrary level of ψ_e^{nl} it becomes obvious that the direction of ∇s does not affect the crack energy. In contrast the paraboloid may be deformed in a way such that an elliptical paraboloid is obtained. In this case the direction of ∇s indeed has a considerable effect on the energy, since for a gradient revealing a major $\frac{\partial s}{\partial y}$ contribution allows for a shift to a lower level compared to the case of a gradient with major $\frac{\partial s}{\partial x}$ contribution of equal magnitude. The proposed shape change can be introduced via a resistance tensor of the form

$$\Phi_0 = \begin{bmatrix} 1 + \alpha & 0 \\ 0 & 1 - \alpha \end{bmatrix}, \quad (4.10)$$

which reveals the eigenvalues $1 \pm \alpha$ quantifying the degree of directionality of the proposed twofold anisotropy by an additional parameter α . As gradients are not restricted to certain directions, the presented formulation represents an elliptical interpolation between the values $1 + \alpha$ and $1 - \alpha$ with respective reference axes being the eigenvectors. The principle axis of a material defining the anisotropy may not generally coincide with the used reference system, which would lead to possible unrepresented weak directions. To satisfy this general case a rotation of Φ_0 is incorporated applying the rotation tensor with respect to the coordinate axis

$$\mathbf{R} = \begin{bmatrix} \cos \theta & -\sin \theta \\ \sin \theta & \cos \theta \end{bmatrix}, \quad (4.11)$$

where the angle θ defines the rotation of the principal axes with respect to the coordinate system. Utilizing this orthogonal rotation tensor and the gradient in the system $\theta \nabla s$ the actual gradient can be expressed by

$$\nabla s = \mathbf{R}^T \theta \nabla s. \quad (4.12)$$

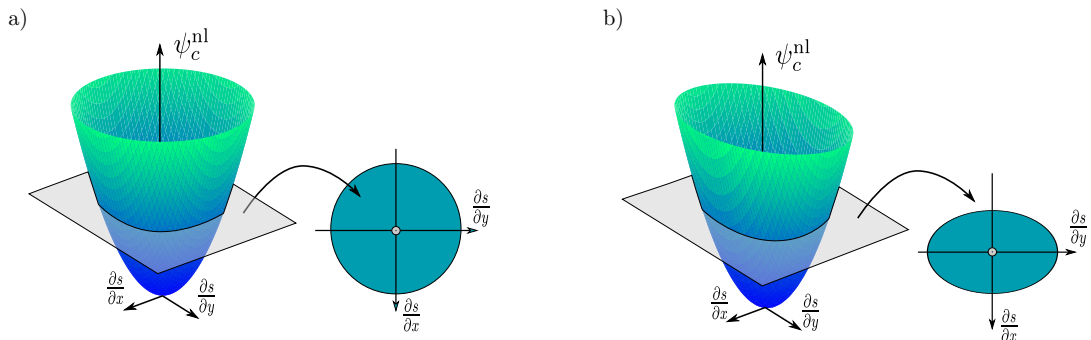


FIGURE 4.6: Schematic illustration of non-local crack potential assuming plane crack evolution of a) the original formulation and b) modified formulation.

Thus one finds

$$\nabla s^T \Phi_0 \nabla s = \theta \nabla s^T \underbrace{\mathbf{R} \Phi_0 \mathbf{R}^T}_{\Phi} \nabla s. \quad (4.13)$$

This yields the rotated second order tensor

$$\Phi = \mathbf{R} \Phi_0 \mathbf{R}^T = \begin{bmatrix} 1 + \alpha (\cos^2 \theta - \sin^2 \theta) & 2\alpha \sin \theta \cos \theta \\ 2\alpha \sin \theta \cos \theta & 1 - \alpha (\cos^2 \theta - \sin^2 \theta) \end{bmatrix}. \quad (4.14)$$

as the general form of the resistance tensor considering a twofold anisotropy. Note that the angle θ vanishes for a principal axis system characterizing the anisotropy that coincides with the reference system and Φ becomes Φ_0 . This formulation is then incorporated within the energy functional (3.33) and one obtains the phase field evolution equation of brittle fracture in materials with an anisotropic fracture toughness by

$$\dot{s} = -M \left\{ \frac{1}{2} g'(s) \boldsymbol{\varepsilon} : [\mathbb{C} \boldsymbol{\varepsilon}] - \mathcal{G}_c \left(\frac{1-s}{2\epsilon} + 2\epsilon \nabla \cdot (\Phi \nabla s) \right) \right\}. \quad (4.15)$$

In this model, the directionality is characterized by material parameters α and θ depending on the orientation of the material and the intensity of the anisotropy, respectively. Again, the resistance tensor, as it is proposed above, only considers twofold anisotropies. A general model could also account for even more complex anisotropies as they are outlined in e.g. Teichtmeister et al., 2017 or Li et al., 2015. This could be addressed by further modifying the resistance tensor.

4.1.3 Analytic Investigation and Parameter Identification

In order to gain a better understanding of the exact influence of the modification introduced above on the phase field model, an analytic assessment is carried out. An analytic solution of the partial differential equations (3.35) or (4.15), respectively, is to the best of the author's knowledge not available. Therefore, the phase field equation for a crack in a load free one dimensional situation

$$0 = 2\epsilon \frac{d^2 s}{dx^2} - \frac{s-1}{2\epsilon} \quad (4.16)$$

is considered. Its solution can be extended to two dimensions under certain assumptions. Incorporating the modification from above the 1d equation becomes

$$0 = 2(1+\alpha)\epsilon \frac{d^2 s}{dx^2} - \frac{s-1}{2\epsilon}. \quad (4.17)$$

To find the solution for this equation on a bounded domain $-1 \leq x \leq 1$, exponential functions are used in the homogeneous part such that

$$s_h = C_1 \exp(\lambda_1 x) + C_2 \exp(\lambda_2 x), \quad (4.18)$$

where $\lambda_{1,2}$ are the roots of the characteristic polynomial of (4.17). They become

$$\lambda_{1,2} = \pm \frac{1}{2\epsilon\sqrt{1+\alpha}}. \quad (4.19)$$

The inhomogeneous part of (4.17) is constant and accordingly a zero degree polynomial a_0 is suitable for the particular solution. Inserting this solution in (4.17) one finds

$$s_p = a_0 = 1. \quad (4.20)$$

and accordingly the general solution becomes

$$s(x) = s_h + s_p = C_1 \exp\left(\frac{1}{2\epsilon\sqrt{1+\alpha}}x\right) + C_2 \exp\left(-\frac{1}{2\epsilon\sqrt{1+\alpha}}x\right) + 1. \quad (4.21)$$

The constants $C_{1,2}$ are defined by the boundary conditions

$$\frac{ds}{dx}\Big|_{s=1} = \frac{ds}{dx}\Big|_{s=-1} = 0, \quad s(x=0) = 0. \quad (4.22)$$

These conditions imply a symmetric course of the phase field with respect to the center of the domain at $x = 0$. In a first place, the latter two conditions are sufficient to determine s within $0 \leq x \leq 1$. The course of the phase field is described by

$$s(x) = \frac{\exp\left(\frac{1}{\epsilon\sqrt{1+\alpha}}\right) - \exp\left(\frac{x-2}{2\epsilon\sqrt{1+\alpha}}\right) - \exp\left(\frac{x}{2\epsilon\sqrt{1+\alpha}}\right) + 1}{\exp\left(\frac{1}{\epsilon\sqrt{1+\alpha}}\right) + 1}. \quad (4.23)$$

This expression can be rewritten by a series of hyperbolic functions

$$s(x) = 1 - \cosh\left(\frac{x}{2\epsilon\sqrt{1+\alpha}}\right) + \sinh\left(\frac{x}{2\epsilon\sqrt{1+\alpha}}\right) \tanh\left(\frac{1}{2\epsilon\sqrt{1+\alpha}}\right), \quad (4.24)$$

which under the assumption of $\epsilon \rightarrow 0$ and incorporating the described symmetry becomes

$$s(x) = 1 - \exp\left(-\frac{|x|}{2\epsilon\sqrt{1+\alpha}}\right) \quad \text{for } \epsilon \rightarrow 0. \quad (4.25)$$

In a comparison with the solution for the basic model (see Kuhn and Müller, 2010), this function does not only depend on the regularizing length scale ϵ but also on the parameter α . Note that the original isotropic model is recovered for $\alpha \rightarrow 0$. The analytic solution (4.25) is illustrated by the plot in Figure 4.7. The solid lines in this plot correspond to the solution of the basic model for isotropic materials. The solutions $s(x)$ are plotted for two different values of ϵ , which illustrated the meaning of this length scale. The crack, or crack field becomes wider for larger values of ϵ and narrows if smaller values of ϵ are used. In contrast, the dashed lines correspond to the solution (4.25) of the modified model. Solutions for different values of the parameter α are presented and these plots reveal an important property of the modification. Considering the basic resistance tensor of the form of (4.10), the parameter α yields a variation of the actual length scale with the consequence of a wider crack for $\alpha > 0$ and a narrow crack for the case of $\alpha < 0$. Within the basic phase field model, sharp cracks are accurately discovered for $\epsilon \rightarrow 0$ and therefore the quality of the approximation of cracks depends on the regularization length. Accordingly, the intensity parameter α may therefore be chosen as small as possible relatively to ϵ . The plots further show that the modification yields the original model for the case of a vanishing anisotropy, i.e. $\alpha \rightarrow 0$.

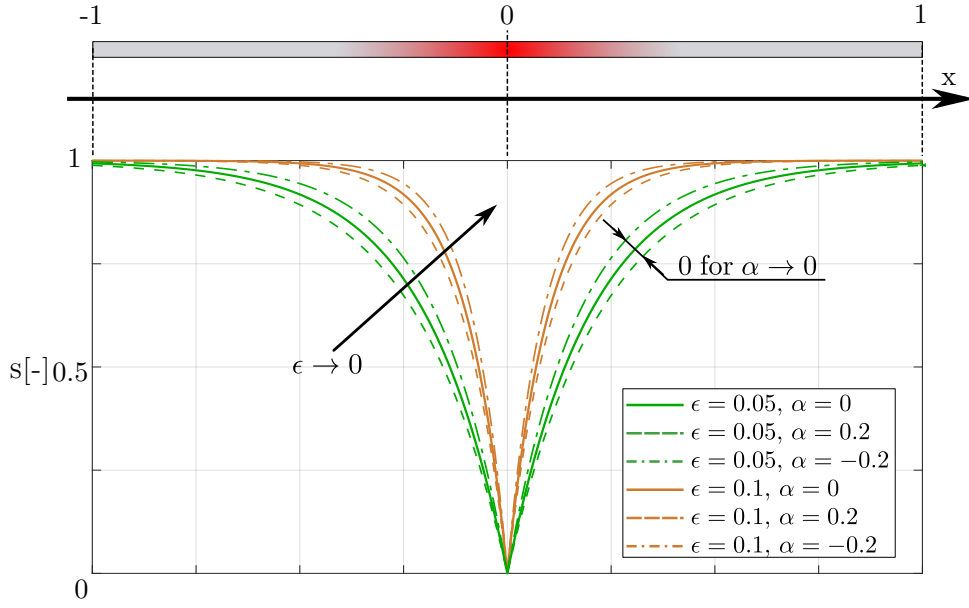


FIGURE 4.7: Illustration of the analytic solution of the proposed phase field model of the one dimensional analysis of a stationary crack using different values for parameters ϵ and α .

Admittedly, within the one dimensional case an anisotropic fracture resistance does not play any role. Nonetheless, this evaluation shows how the modification affects the solution of the phase field. Further, the solution (4.25) may be transferred to two dimensions by a thought experiment. This means that both, the positive and the negative values for α are acting and while the potential regularization width is decreased in a certain direction it is increased in another direction. This is illustrated by means of an energetic assessment. The crack energy of a phase field crack in two dimensions can be approximated by a proper extension of the one dimensional case. For an unidirectional crack, an extrusion of the one dimensional solution is depicted in Figure 4.8a). The major surface energy contribution is provided by the longitudinal part of the crack field (see Figure 4.8a). Extending the solution equation solely in one coordinate direction, the energy consumed by the corresponding phase field can, under consideration of a square domain of $2L$ with a crack of length $a \ll L$ orientated in y -direction, be approximated by

$$E_c = \mathcal{G}_c \int_{-a/2}^{a/2} \int_{-L}^L \frac{(1-s)^2}{4\epsilon} + \epsilon(1+\alpha) \left(\frac{\partial s}{\partial x} \right)^2 + \epsilon(1-\alpha) \left(\frac{\partial s}{\partial y} \right)^2 dx dy, \quad (4.26)$$

With (4.25) and the gradient

$$\nabla s = \begin{pmatrix} \frac{1}{2\epsilon\sqrt{1+\alpha}} \exp\left(-\frac{x}{2\epsilon\sqrt{1+\alpha}}\right) \\ 0 \end{pmatrix} \quad (4.27)$$

for this special case the integral can be computed by

$$= 2\mathcal{G}_c \int_{-a/2}^{a/2} \int_0^L \frac{1}{2\epsilon} \exp\left(-\frac{x}{\epsilon\sqrt{1+\alpha}}\right) dx dy \quad (4.28)$$

$$= 2\mathcal{G}_c\sqrt{1+\alpha} \int_{-a/2}^{a/2} \left[\exp\left(-\frac{x}{\epsilon\sqrt{1+\alpha}}\right) \right]_0^L dy \quad (4.29)$$

$$= a\mathcal{G}_c\sqrt{1+\alpha} \left[1 - \exp\left(\frac{-L}{\epsilon\sqrt{1+\alpha}}\right) \right]. \quad (4.30)$$

The phase field converges to the sharp crack solution for $\epsilon \rightarrow 0$, and in this case the crack energy becomes

$$E_c = a\mathcal{G}_c\sqrt{1+\alpha} \quad \text{for } \epsilon \rightarrow 0, \quad (4.31)$$

which illustrates the different amount of energy consumed by the crack compared to the isotropic case. Additionally, one may note that for a crack growing solely in x -direction, the function $s(y)$ would be different and the respective surface energy would for that case be obtained as

$$E_c = a\mathcal{G}_c\sqrt{1-\alpha} \quad \text{for } \epsilon \rightarrow 0. \quad (4.32)$$

In these considerations the diffuse region at the end of the crack is neglected. The effect of this simplification is assessed. As depicted in Figure 4.8b), the crack energy associated with the two ends of a unidirectional crack can be determined by

$$E_c^{\text{tip}} = \int_{A_{\text{tip}}} \psi_c dA = 2 \int_0^\pi \int_0^R s(r, \varphi) r dr d\varphi. \quad (4.33)$$

In order to express the crack energy density in the system of polar coordinates defined in Figure 4.8b), the solution is rotated with respect to the center ($x = y = 0$) and one obtains

$$s(r, \varphi) = 1 - \exp\left(\frac{-r}{2\epsilon}\right), \quad (4.34)$$

which with $\alpha \rightarrow 0$ becomes a function of the coordinate r only. Further the gradient in the defined $r - \varphi$ -system can be derived by

$$\begin{bmatrix} \frac{\partial s}{\partial r} \\ \frac{\partial s}{\partial \varphi} \end{bmatrix} = \underbrace{\begin{bmatrix} \frac{\partial x}{\partial r} & \frac{\partial y}{\partial r} \\ \frac{\partial x}{\partial \varphi} & \frac{\partial y}{\partial \varphi} \end{bmatrix}}_{\mathbf{T}} \begin{bmatrix} \frac{\partial s}{\partial x} \\ \frac{\partial s}{\partial y} \end{bmatrix}, \quad (4.35)$$

where \mathbf{T} is the respective transformation matrix relating the gradients of the $x - y$ -system with $r - \varphi$ -system. With the coordinate transformations

$$x = r \cos \varphi \quad \text{and} \quad y = r \sin \varphi \quad (4.36)$$

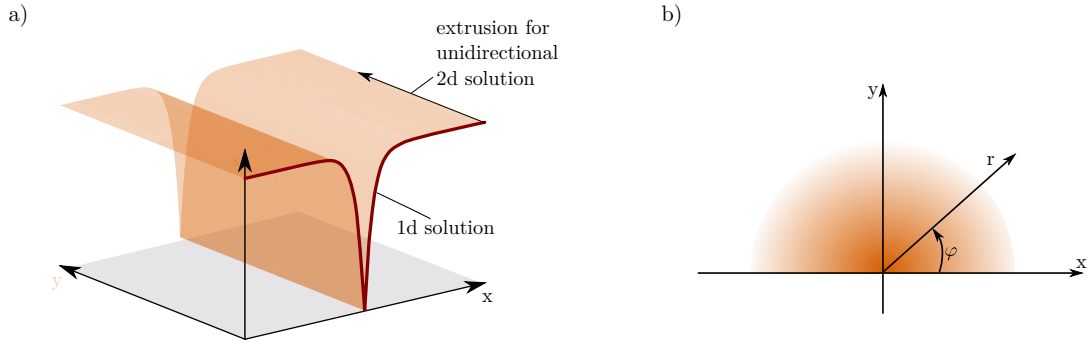


FIGURE 4.8: Schematic illustration of the extension of the one dimensional phase field solution to an unidirectional crack: a) segment of surface plot of the crack field; b) plane view on tip of the crack field.

this matrix and its inverse are found as

$$\mathbf{T} = \begin{bmatrix} \cos \varphi & \sin \varphi \\ -r \sin \varphi & r \cos \varphi \end{bmatrix} \quad \text{and} \quad \mathbf{T}^{-1} = \begin{bmatrix} \cos \varphi & -\frac{1}{r} \sin \varphi \\ \sin \varphi & \frac{1}{r} \cos \varphi \end{bmatrix}. \quad (4.37)$$

For the crack energy density (4.5) the spatial gradient of s may be described in terms of the polar coordinates r and φ by transforming (4.35) to

$$\begin{bmatrix} \frac{\partial s}{\partial x} \\ \frac{\partial s}{\partial y} \end{bmatrix} = \mathbf{T}^{-1} \begin{bmatrix} \frac{\partial s}{\partial r} \\ \frac{\partial s}{\partial \varphi} \end{bmatrix} = \begin{bmatrix} \frac{\cos \varphi}{2\epsilon} \exp\left(\frac{-r}{2\epsilon}\right) \\ \frac{\sin \varphi}{2\epsilon} \exp\left(\frac{-r}{2\epsilon}\right) \end{bmatrix} \quad (4.38)$$

and accordingly the crack energy density becomes

$$\psi_c = \mathcal{G}_c \left(\frac{(1-s)^2}{4\epsilon} + \epsilon |\nabla s|^2 \right) \quad (4.39)$$

$$= \mathcal{G}_c \left(\frac{1}{4\epsilon} \exp\left(-\frac{r}{\epsilon}\right) + \frac{\cos^2 \varphi}{4\epsilon} \exp\left(-\frac{r}{\epsilon}\right) + \frac{\sin^2 \varphi}{4\epsilon} \exp\left(-\frac{r}{\epsilon}\right) \right) \quad (4.40)$$

$$= \frac{\mathcal{G}_c}{2\epsilon} \exp\left(-\frac{r}{\epsilon}\right). \quad (4.41)$$

Inserting this formulation for the crack energy density in (4.33) the integral yields

$$E_c^{\text{tip}} = 2 \int_0^\pi \int_0^R \frac{\mathcal{G}_c}{2\epsilon} \exp\left(-\frac{r}{\epsilon}\right) r \, dr \, d\varphi = 0 \quad \text{for } \epsilon \rightarrow 0. \quad (4.42)$$

According to these considerations the ends of a phase field crack can be neglected within energy evaluations for small values of the length scale ϵ . The radius of the transition zone is not constant in case of the modification for anisotropy. Nonetheless, the character of the equations is unaltered and therefore in case of the anisotropic modification the crack ends, in terms of surface energy, also do not contribute for $\epsilon \rightarrow 0$ in terms of surface energy.

This analysis illustrates how the phase field model is effected in terms of a directional dependency of energy by the introduced modification. While the model can minimize the energy by growing the crack in one direction, it will consume a higher amount if the

crack grows in the perpendicular direction. Furthermore, the derivations indicate that the modification does not violate the convergence of the regularization.

4.2 Phase Field Model for Fatigue Crack Growth

As many reviews of cases of material failure show, the field of cyclic mechanical fatigue is one of the most important branches of previous and current research in engineering. Investigations show for instance, that the major cause for the failure of shafts and axles is fatigue (see Haibach, 2006). Especially today as the rising urge for saving energy drives the principles of lightweight construction to be applied for new products and developments, a clear understanding of fatigue and fatigue crack growth becomes very important. The phenomenon of mechanical fatigue of materials and structures was so far broadly investigated and treated in a number of textbooks by e.g. Dowling, 2013, Suresh, 1992, Schijve, 2009 or Haibach, 2006. In section 2.3 the two phases of the fatigue life are introduced: (*i*) nucleation of microstructural degradation and growth of corresponding microcracks until the formation of a macrocrack and (*ii*) the propagation of this macrocrack until an instance at which final fracture of the structure occurs. From the perspective of numerical modeling there are two challenging key issues:

- **high computational effort**

Fatigue of the microstructure is a steady process under ongoing repetition of loading and unloading. Under comparably low excitation this can be an extremely slow process. Accordingly, a critical number of cycles leading to failure in the order of 10^6 to 10^7 or even more is common within this field. Running simulations for such a number of cycles is certainly impractical. The suitable balance between accuracy in terms of results and simplifications must be found in this concern.

- **lack of mechanistic basis**

By the beginning of the last century the phenomenon of fatigue failure was a scientific miracle. Nowadays, irreversible cyclic slip is identified as the underlying microscopic source of the phenomenon. However, fatigue is affected by a large number of complex processes occurring on different scales. Still, no generally valid equation exists that could describe the fatigue evolution under arbitrary conditions in terms of material, load distribution, amplitude, sequence among others. Accordingly, the issue is not only to solve differential equations numerically. Due to this lack of a general mechanistic description empirical laws must be incorporated within the modeling frameworks in order to develop numerical tools. It must be determined which law is appropriate for a specific problem and how can it be incorporated.

Several attempts to perform lifetime predictions have been published so far. Paris' law (Paris and Erdogan, 1963) is used to simulate fatigue crack growth for instance in Judt and Ricoeur, 2015 using finite elements. In this study a sequential scheme is proposed, where after a solution step for the deformation the ΔJ -integral is evaluated at the crack tip in order to get the incremental value for crack extension from a Paris curve. A new mesh with an extended crack is then set up and the procedure is repeated. The new mesh is refined at the crack tip. Note, that this basic scheme is not capable of handling fatigue crack nucleation. A similar scheme was proposed by O'Hara et al., 2016 using generalized finite elements. Paris' law is also incorporated in a widely used tool for fatigue crack growth

simulations, see NASGRO, Forman et al., 2005. In contrast, models were presented that try to provide a more micromechanical basis. In Marigo, 1985 and Chow and Wei, 1991 cyclic fatigue life until crack initiation was modeled using the framework of Continuum Damage Mechanics (CDM) from Lemaitre, 1992. Fish and Oskay, 2005 introduced a numerical model, where the damage evolution is treated by an increasing void volume fraction described by Gurson's model (Gurson, 1977). In the latter work cracks are modeled by the deletion of finite elements once the void volume fraction exceeds a critical damage value.

4.2.1 Review of Phase Field Models for Fatigue

In terms of phase field modeling, the field of mechanical fatigue or fatigue crack growth is considered only quite recently. The first publication describing an application of a phase field fracture model to fatigue was, to the best of the author's knowledge, proposed by Alessi et al., 2017. This work considers the one dimensional case, meaning fatigue of a bar due to tensile cycling. They propose the respective formulation of the internal energy of the bar with

$$\mathcal{E} = \int_0^L \left[\frac{1}{2} E(D) \varepsilon^2 + d(\bar{\varepsilon})(w'(D) + w(0)l^2 D') \right] dx. \quad (4.43)$$

The phase field order parameter D is considered as a damage variable in the sense of CDM with $D = 0$ representing intact material and $D = 1$ representing broken material. The different interpretations of the order parameter are discussed in the next section. In Alessi et al., 2017 D degrades the Young's modulus E of the bar with length L . Accordingly, the first term of the integrand represents the strain energy density of the bar. The second part of the integrand is denoted as fracture energy of the bar with length scale l and the damage dissipation function $w(D)$ with $w(D = 0) = 0$ and $w'(D) \geq 0$. The function $d(\bar{\varepsilon})$ is denoted a fatigue degradation function. This damage degradation function is designed such that it decreases the fracture potential according to an increase of the accumulated plastic strain $\bar{\varepsilon}$. Decreasing the fracture energy, or as one can also state, degrading the critical energy release rate, enables the damage variable D to increase and accordingly cause fracture of the bar.

Following up on this publication Carrara et al., 2018 proposed a generalization of the model from Alessi et al., 2017. Other approaches were proposed by Mesgarnejad et al., 2019 and Seiler et al., 2020. These models are different in several terms as for instance in the driving force of fatigue but the approaches do indeed coincide with the idea of Alessi et al., 2017 concerning the degradation of the fracture energy to cause crack growth. Furthermore, a phase field fatigue model for cracking in cyclically loaded concrete was proposed by Wriggers et al., 2020. Within several contributions by the author of the present work Schreiber et al., 2019b, Schreiber et al., 2020a, and Schreiber et al., 2019a an alternative approach is considered. Here, an additional energy contribution is introduced to enter the total energy. Basically, this new contribution is proposed to represent the deformation work associated with cyclic loading. This model is outlined in the following.

4.2.2 Interpretation of Order Parameter

As stated in previous sections the interpretation of the order parameter is an important issue to deal with. In Alessi et al., 2017 the order parameter is used as damage variable in the sense of the CDM framework by Lemaitre, 1992. By this kind of interpretation, a physical meaning is assigned to the order parameter. Within CDM the term damage refers to the contribution of micro voids at a material point with

$$D = \frac{\Delta S_D}{\Delta S}. \quad (4.44)$$

In this definition ΔS is denoted the area of a cross section in the point under consideration, and ΔS_D the corresponding area of all microvoids intersected by the cross section. By this definition one obtains the range of the damage variable D as $0, \dots, 1$ and a state $D = 1$ represents broken material or fully damaged material, while the state $D = 0$ refers to intact material. This definition is applied in the phase field model from Alessi et al., 2017. Suppose a material point is exposed to a constant stress $\boldsymbol{\sigma}$. The effective stress tensor

$$\hat{\boldsymbol{\sigma}} = \frac{1}{1-D} \boldsymbol{\sigma} \quad (4.45)$$

will increase, since the effective surface area carrying load is reduced by D . Assuming a linear elastic material referring to

$$\psi = \frac{1}{2} \hat{\boldsymbol{\sigma}} : (\mathbb{C}^{-1} \hat{\boldsymbol{\sigma}}), \quad (4.46)$$

the strain energy density for a damaged material point is described under consideration of the principle of equivalent strain by

$$W_D = \frac{1}{2(1-D)^2} \boldsymbol{\sigma} : (\mathbb{C}^{-1} \boldsymbol{\sigma}). \quad (4.47)$$

The corresponding strains may be obtained by differentiation as

$$\boldsymbol{\varepsilon} = \frac{\partial W_D}{\partial \boldsymbol{\sigma}} = \frac{1}{(1-D)^2} \mathbb{C}^{-1} \boldsymbol{\sigma} \quad (4.48)$$

and accordingly the effective compliance tensor is identified as

$$\tilde{\mathbb{C}}^{-1} = \frac{1}{(1-D)^2} \mathbb{C}^{-1}. \quad (4.49)$$

Solving the constitutive law (3.34) for the strains one obtains

$$\boldsymbol{\varepsilon} = \frac{\boldsymbol{\sigma}}{s^2} \mathbb{C}^{-1} \quad \text{with} \quad \tilde{\mathbb{C}}^{-1} = \frac{1}{s^2} \mathbb{C}^{-1}, \quad (4.50)$$

where the basic degradation function (3.36) is applied and the residual stiffness parameter η is neglected. Comparison of (4.49) and (4.50) shows that the two approaches coincide if the relation

$$s = 1 - D \quad (4.51)$$

holds. Accordingly, the phase field model basically represents a gradient damage model. However, the evolution of damage or the driving mechanism in Alessi et al., 2017 as well as in any other phase field fatigue model is purely phenomenological as no sufficient understanding of the processes exists. In Bourdin et al., 2000 and Bourdin, 2007 the phase field variable is explicitly not meant to describe a physical quantity such as damage. The order parameter is rather incorporated to enable a regularization of cracks and the respective surface energy. The interpretation is in the scope of an indicator function. The basic phase field model Kuhn and Müller, 2010 is based on the latter works and therefore, within the enhancement for fatigue crack growth, this type of interpretation is still maintained. The scalar phase field variable s or the transition zone ($0 < s < 1$), respectively, has no direct physical meaning. The meaning of s results from the philosophy of the phase field paradigm itself. This is to approximate sharp interfaces by a smooth transition of an auxiliary parameter for numerical convenience. In the following, the term damage will always refer to fatigue. The work associated with this fatigue damage will be incorporated as additional driving force for the phase field evolution. This means, that s is driven by an estimation of the fatigue damage increment dD_f , a quantity related to the number of applied load cycles.

4.2.3 Modification of Driving Force Mechanism

The characteristic self organizing properties of the phase field modeling framework significantly result from the formulation of the evolution equation for the considered phases. Generally, one can directly start with the construction of such an equation. However, commonly these evolution equations are derived from energy potentials and contain the property to approximate a sequence of energy minimizers. No additional criteria are required if the potential properly represents the phenomenon regarding all relevant aspects. This was illustrated in the last section by a modification concerning the non-local surface energy contribution. Anisotropy of the fracture resistance was incorporated. The established modification regarding fatigue is different. The static threshold for fracture can be significantly higher than the threshold for the onset of fatigue of a material. Nevertheless, failure occurs under cyclic loading. Figure 4.9 schematically illustrates the problem of the basic phase field model. A sample is subject to tensile loading. For the case of a monotonously increasing load (blue curve in Figure 4.9) the evolution equation (3.35)

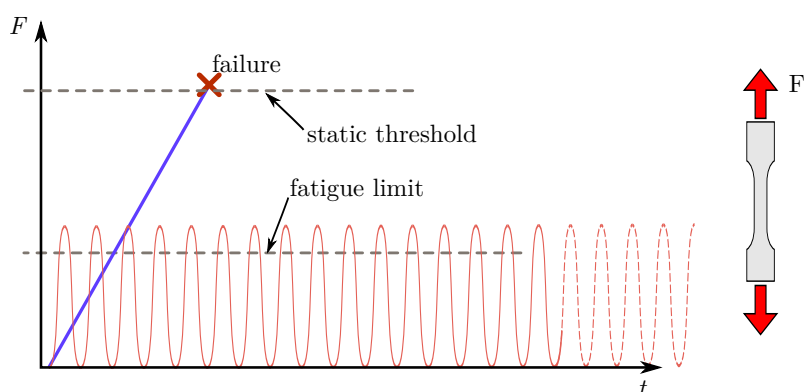


FIGURE 4.9: Schematic illustration of comparison of monotoneous and cyclic loading applied on an ideal brittle material.

yields crack initiation for a certain load level as this minimizes the internal energy. In other words, it will become more favorable from an energetic perspective to decrease the phase field s , than to allow for more strain energy. Due to the significantly lower maximum load value of the cyclic load function a potential evolution of the phase field will not be effective in minimizing the energy. Accordingly, an infinite number of load cycles could be simulated without any occurrence of material degradation. However, such a load function with repetition of loading and unloading indeed spends a significant amount of energy, which is consumed by irreversible processes associated with fatigue (see e.g. Mughrabi, 2013). Obviously, the classical model Kuhn and Müller, 2010 does not take into account the presence of these irreversibilities. Consequently, an additional energy contribution is included into the free energy. Thus, the new enhanced regularized formulation of the total energy is proposed as

$$\begin{aligned} E^f &= E(\boldsymbol{\varepsilon}, s, \nabla s) + E^{\text{ac}}(D_f, s) \\ &= \int_{\Omega} [(g(s) + \eta)W + \mathcal{G}_c \Gamma] \, dV + \int_{\Omega} \underbrace{h(s)P(D_f)}_{\psi_p} \, dV \end{aligned} \quad (4.52)$$

in order to account for the discussed fatigue related energy contributions. This functional of the total internal energy consists of the basic formulation of brittle fracture and an additional energy contribution characterized by the term ψ_p . This contribution is governed by the current state of fatigue damage $D_f(\mathbf{x}, t)$ and provides the necessary driving force. The function $h(s)$ is a degradation function with an analog purpose as $g(s)$. Presuming an increase of the energy density $P(D_f)$ this degradation function enables a decline of the total energy by decreasing the phase field s . This mechanism generally enables crack growth driven by fatigue. A piecewise defined power function is proposed to govern the energy contribution E^{ac} by

$$P(D_f) = q \langle D_f - D_{fc} \rangle^b, \quad (4.53)$$

with the Macaulay brackets, which are defined via

$$\langle \cdot \rangle^n = \begin{cases} 0 & \text{for } (\cdot) \leq 0 \\ (\cdot)^n & \text{for } (\cdot) > 0. \end{cases} \quad (4.54)$$

This function is designed such that the fatigue driving force increases rapidly once the critical value for damage D_{fc} is exceeded. This rapid increase is crucial as otherwise cracks are prone to grow wide, i.e. perpendicular to the growth direction. The function $P(D_f)$ is plotted for a number of different sets of parameters in Figure 4.10. On the other hand the function must be designed in a way such that reliable convergence behavior within the numerical solution scheme is ensured. Accordingly, the parameters q and b that characterize this fatigue driving function can be viewed as regularization parameters.

Technically, the purpose of the modification is to create an opportunity to shift the driving energy up to a level such that the threshold for resistance represented by ψ_c is reached. However, the key issue is still to define how the fatigue damage is determined. In a general manner, the current state of fatigue damage is the sum of the previous state plus the incremental damage representing the increase for a certain period of time or cycles,

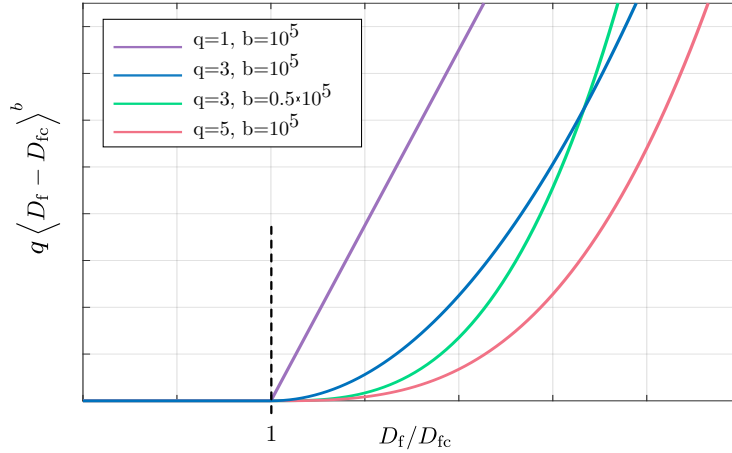


FIGURE 4.10: Illustration of the fatigue driving function $P(D_f)$ for different combinations of parameters q and b .

respectively. This is expressed by

$$D_f = D_0 + dD_f. \quad (4.55)$$

As outlined in section 2.3 fatigue is a complex field and its evolution is effected by a comparative large number of effects. Thus the fatigue increment

$$dD_f = dD_f(D_0, \sigma_a, \bar{\sigma}, R) \quad (4.56)$$

is certainly a function of the load amplitude σ_a , but also depends on the mean value of the stress of the particular cycles $\bar{\sigma}$, the stress ratio R , and also the damage history or the previous state of fatigue damage D_0 . Note that the number of effects considered by (4.56) is incomplete as effects like strain rate or temperature are neglected. However, (4.56) illustrates the most important features of fatigue crack growth and is restricted to those effects considered within this work. This illustrates the complexity of the fatigue phenomenon. Accordingly, an important task in this context is to find an appropriate expression for the increment dD_f , that in the best case may cover all effects. On the other hand one has to keep in mind the increasing computational costs necessary to satisfy the high number of load cycles compared to a quasi static simulation. Rather complex approaches as e.g. contributions from Chow and Wei, 1991 or Fish and Yu, 2002, which are based on continuum mechanics and consistent with the second law of thermodynamics are not feasible from the perspective of computation effort. Technically almost any approach could be integrated in the proposed model but it is simply not convenient to apply a micromechanical approach at this stage. Anyway, there is certainly a number of straightforward approaches. The model for fatigue damage proposed by Chaboche and Lesne, 1988 can be formulated in terms of the damage increment by

$$dD_{f,Ch} = D^{\gamma_1} \left[\frac{\sigma_{\max} - \bar{\sigma}}{f(\bar{\sigma})} \right]^{\gamma_2} dN, \quad (4.57)$$

with the cycle increment dN , the parameters γ_1 and γ_2 as well as the mean stress effect function $f(\bar{\sigma})$, which must be determined by different experiments. Note that the current

state of damage is taken into account by this formula. Separation of variables and integration assuming constant states of σ_{\max} and $\bar{\sigma}$ yields the state of the accumulated fatigue damage as

$$D_{f,\text{Ch}}(t) = \left(\frac{N(t)}{N_{F_i}} \right)^{1/(1-\gamma_1)} \quad (4.58)$$

for constant amplitude loading with the number of bearable load cycles N_{F_i} and the applied number of cycles at a certain time $N(t)$. An even more simple estimate for the damage increment is the Miner rule (Miner, 1945). In terms of incremental damage this rule can be formulated as

$$dD_{f,\text{Mi}} = \frac{1}{N_{F_i}} dN, \quad (4.59)$$

which by integration yields the current state of damage

$$D_{f,\text{Mi}}(t) = \frac{N(t)}{N_{F_i}}. \quad (4.60)$$

Both approaches, i.e. the Chaboche and the Miner approach, were initially developed to describe the first period of the fatigue, which contains the time until macro crack initiation of uncracked specimens. So far these theories were incorporated in numerical models for fatigue crack growth of sharp interface models (see e.g. Bograd et al., 2008). The essential difference between the two approaches is the incorporation of the current state of damage within the first approach. The differences in terms of the characteristic of the damage accumulation are schematically illustrated in Figure 4.11. Generally, due to the linear character of the Miner rule, the sequence of cycle intervals with different amplitude does not play a role in terms of the final state of damage. In contrast, the approach by Chaboche indicates a nonlinear relation in a plot of the number of cycles versus damage. Due to the incorporation of the actual damage state, a different result for the final damage is obtained by different sequences, as Figure 4.11a) illustrates. The change in the amplitude of a load time history can exemplarily be interpreted as a switch from the red curve to the blue curve

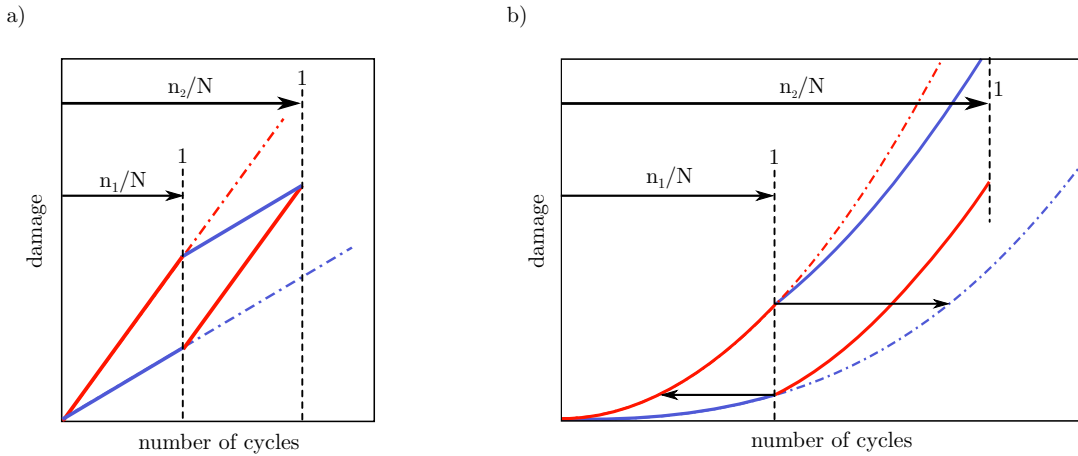


FIGURE 4.11: Comparison of a) linear damage accumulation (Miner) and b) nonlinear damage accumulation (Chaboche).

curve. This effect of the sequence was proven by experimental investigations as outlined in textbooks (Dowling, 2013; Schijve, 2009; Haibach, 2006). The physical reason can be illustrated considering the micromechanical model of a dilute defect distribution (see e.g. Gross and Seelig, 2011). It can be shown that the degradation of the stiffness of a representative volume element containing microcracks is proportional with respect to the squared length of the microcracks. Nonetheless, the nonlinear model Chaboche and Lesne, 1988 contains a large number of parameters. In fact, it may be anticipated that sequence effects in fatigue crack growth are obtained by incorporating the Miner rule (see Schreiber et al., 2019b), which is less complex to implement. This will also be verified in the present work. Furthermore, a physical foundation of the Miner rule in terms of fatigue crack growth can be shown by interpreting damage accumulation as cyclic crack propagation. Utilizing Paris' law (2.62) and separating variables, integration may subsequently be performed as

$$\int_0^{\Delta N} dN = \int_{a_0}^{a_c} \frac{1}{C[\Delta K]^m} da. \quad (4.61)$$

Therein, ΔN is a cycle interval, a_0 is the initial crack length and a_c is the critical crack length representing the point of brutal rupture for a respective amplitude. Considering the cyclic stress range $\Delta K = \Delta\sigma\sqrt{\pi a}Y(a)$, this results in the cycle interval to failure

$$\Delta\sigma = \left[\frac{\sqrt{\pi^{-m}}}{\Delta N_c C} \int_{a_0}^{a_c} \frac{1}{(aY(a))^m} da \right]^{1/m}, \quad (4.62)$$

which according to the similarity with (2.60) regarding its structure is referred to as S-N curve for components (see e.g. Haibach, 2006). Furthermore, if the case of a constant geometry factor $Y(a) = Y$ is considered, this equation may be rearranged to find

$$\Delta N_k = \frac{2 \left(a_k^{(1-m/2)} - a_{(k-1)}^{(1-m/2)} \right)}{(2-m)C[\Delta\sigma_k\sqrt{\pi}]^m}, \quad (4.63)$$

which describes the cycle interval for the crack propagation from initial crack length a_{k-1} until the crack length a_k . This is obtained after ΔN_k under the stress amplitude $\Delta\sigma_k$. Accordingly, the cycle interval until failure of the particular amplitudes $\Delta\sigma_k$ is obtained as

$$\Delta N_k^{\text{break}} = \frac{2 \left(a_c^{(1-m/2)} - a_0^{(1-m/2)} \right)}{(2-m)C[\Delta\sigma_k\sqrt{\pi}]^m}, \quad (4.64)$$

where the same initial and final crack length is presumed for all amplitudes. According to the Miner rule (2.60) the fatigue damage is expressed as the sum of the particular partial damage increments with

$$D = \sum_{k=1}^n \Delta D_k = \sum_{k=1}^n \frac{\Delta N_k}{\Delta N_k^{\text{break}}}. \quad (4.65)$$

Inserting (4.63) and (4.64) in this damage sum and considering the final crack length of the n -th increment to be the critical length a_c one finds the Miner rule confirmed for this setup

as it is proposed that D approaches 1 for complete failure. Certainly, the final crack length for rupture a_c is not equal for all amplitudes $\Delta\sigma_k$. The effect, however, on (4.65) is small as generally $a_0 \ll a_c$ (see Radaaj and Vormwald, 2007). Furthermore, this connection between Paris' law and Miner's rule is shown even for the general case of $Y(a)$ in Ciavarella et al., 2018. These considerations indicate a general relation between Miner's rule and fatigue crack growth. This motivates the Miner rule (4.59) to be used to determine the fatigue damage increment within the proposed phase field model. The critical cycle number N_{F_i} for a certain load amplitude can be obtained from appropriate S-N curves. Accordingly, the estimate for the fatigue damage (4.55) becomes

$$D_f = D_0 + (n^D)^{-1} \left(\frac{\tilde{\sigma}(\boldsymbol{\varepsilon})}{A_D} \right)^k dN, \quad (4.66)$$

with lifetime exponent k , knee point cycle number n^D , and threshold stress A_D . Using this law the new total internal energy E^f of a component that potentially contains a crack driven by quasi static loading and also by critical cyclic loading is finally formulated as

$$\begin{aligned} E^f = & \int_{\Omega} \left[(g(s) + \eta) \frac{1}{2} \boldsymbol{\varepsilon} : [\mathbb{C}\boldsymbol{\varepsilon}] + \mathcal{G}_c \left(\frac{(1-s)^2}{4\epsilon} + \epsilon |\nabla s|^2 \right) \right] dV \\ & + \int_{\Omega} h(s) q \left\langle D_0 + (n^D)^{-1} \left(\frac{\tilde{\sigma}(\boldsymbol{\varepsilon})}{A_D} \right)^k dN - D_{fc} \right\rangle^b dV. \end{aligned} \quad (4.67)$$

The actual driving force entering the S-N curve in this free energy functional is $\tilde{\sigma}(\boldsymbol{\varepsilon})$, which is a scalar stress measure depending on the strain tensor $\boldsymbol{\varepsilon}$. The exact choice may depend on several properties like for instance the material or the type of loading. This dependency will be further discussed in the next section. Within the cyclic resolved simulation scheme, the current state of fatigue damage D_0 is treated as a history variable updated in every simulation step. The simulation scheme is outlined subsequently in section 4.2.5. Regarding the accumulation of driving forces within the fatigue related component of (4.67) it is worth mentioning, that driving stresses not exceeding the fatigue limit A_D are neglected and accordingly have zero contribution. The related stresses provide a good insight into the physical interpretation of this enhanced phase field formulation. In accordance to (3.34) the stresses are derived by

$$\boldsymbol{\sigma}^f = \frac{\partial(\psi + \psi_p)}{\partial \boldsymbol{\varepsilon}} = \underbrace{(g(s) + \eta) \mathbb{C} \boldsymbol{\varepsilon}}_{\boldsymbol{\sigma}^e} + \underbrace{h(s) \frac{\partial P}{\partial D_f} \frac{\partial D_f}{\partial \tilde{\sigma}(\boldsymbol{\varepsilon})} \frac{\partial \tilde{\sigma}(\boldsymbol{\varepsilon})}{\partial \boldsymbol{\varepsilon}}}_{\boldsymbol{\sigma}^{ac}}, \quad (4.68)$$

with the additional contribution to the stresses

$$\boldsymbol{\sigma}^{ac} = h(s) q b \left\langle D_f - D_{fc} \right\rangle^{(b-1)} \cdot dN \frac{k \tilde{\sigma}(\boldsymbol{\varepsilon})^{(k-1)}}{n^D A_D^k} \frac{\partial \tilde{\sigma}(\boldsymbol{\varepsilon})}{\partial \boldsymbol{\varepsilon}}, \quad (4.69)$$

where the derivative $\frac{\partial \tilde{\sigma}}{\partial \boldsymbol{\varepsilon}}$ obviously depends on the choice of the driving force $\tilde{\sigma}(\boldsymbol{\varepsilon})$. The first term in (4.68) is the degraded tensor of the static stresses. The second term can be interpreted as an additional stress component accounting for accumulated micro stresses as a consequence of the cyclic slip irreversibilities caused by repetitive loading and unloading.

4.2.4 Characteristic Driving Stress Quantity

As indicated above the model is significantly effected by the choice for the driving force $\tilde{\sigma}$. Within Schreiber et al., 2020a and Schreiber et al., 2019a the stress in vertical direction was used as driving stress. For strictly vertical tensile testing, i.e. mode I loading, this choice is natural. Different criteria were proposed for the determination of the crack extension direction. Basically, these criteria were shown to lead to similar directions of the deflection angel for small K_{II} contributions. A criterion, which is formulated in terms of stresses was proposed by Erdogan and Sih, 1963. The main hypothesis of this criterion is that the larges tension around the crack tip is relevant for crack extension. This criterion is referred to as Maximum Tensile Stress (MTS) criterion and was derived under the presumptions of LEFM for static loads. According to Kuna, 2010 it can be used for cyclic loading if the restrictions of LEFM are not violated. The MTS uses the maximum circumferential component of the stress tensor in a system of polar coordinates r, φ , where the current crack tip acts as a pole. As illustrated in Figure 4.12, the deflection direction of a crack under arbitrary load is determined assuming that,

- the crack extends in radial direction r with respect to the angel φ_c , which is perpendicular to the maximum tensile stress $\sigma_\varphi(\varphi)_{\max}$ and
- the crack extends once the $\sigma_\varphi(\varphi)_{\max}$ exceeds the material specific critical stress σ_c , which is associated with reference case of $K_I = K_{Ic}$ and $K_{II} = 0$.

Note that due to the singularity of the stresses at the crack tip the MTS is evaluated at a certain distance $r > 0$. In agreement with the items above, the relevant maximum tensile stress $\sigma_\varphi(\varphi)_{\max}$ is characterized by

$$\frac{\partial \sigma_\varphi}{\partial \varphi} = 0 \quad \text{and} \quad \frac{\partial^2 \sigma_\varphi}{\partial \varphi^2} < 0. \quad (4.70)$$

These constraints are in conflict with the implicit implementation of the phase field framework from above. It can, however, be shown (see e.g. Kuna, 2010) that for the direction of $\sigma_\varphi(\varphi)_{\max}$ the shear stress vanishes and the MTS is identical to the first principal stress,

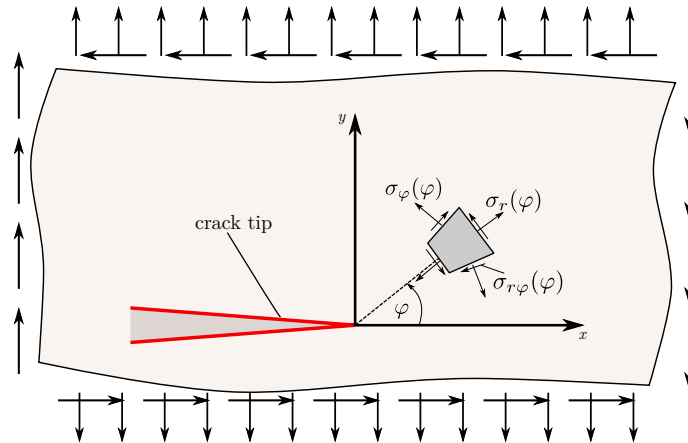


FIGURE 4.12: Near tip stress field in polar coordinates for a crack in an infinite plate under arbitrary load state ($K_{II} > 0$).

which in two dimensions can be explicitly formulated by

$$\sigma_1 = \frac{\sigma_x + \sigma_y}{2} + \sqrt{\left(\frac{\sigma_x - \sigma_y}{2}\right)^2 + \tau_{xy}^2}. \quad (4.71)$$

In other words, according to the MTS criterion the characteristic driving force quantity to be incorporated in the phase field model is the first principal stress. Note that for load cases with $K_{II} \rightarrow 0$ the first principal becomes the σ_y component. Accordingly, within simulations of pure mode I it is sufficient to simply use this component as $\tilde{\sigma}$.

The choice of the first principal stress as driving force quantity will be confirmed by simulations outlined in section 6.2.3. However, this choice does not claim to be generally valid. There may be materials or other effects, where a different stress as e.g. the von-Mises stress, or others provide more reliable results.

4.2.5 Cycle Resolved Simulation Scheme

The mechanisms associated with the disruption of materials caused by cyclic fatigue may depending on the magnitude of the load cycles, extend over a very long period of time. Accordingly, the number of load cycles before crack nucleation or growth occurs can be high. Without an efficient simulation scheme, where a large number of cycles are integrated, simulation times can not be kept within a reasonable limit. The collection of load cycles in terms of damage to blocks is done within conventional fatigue life approaches. The connection of all these blocks represents the whole load history and is called load collective. For fatigue crack growth simulations, Fish and Yu, 2002 proposed the so called "cycle jump". This term denotes a scheme, where the fatigue damage after the i th simulation step handling a certain amount of load cycles $D_{(i+\Delta N_i)}$ is computed by

$$D_{(i+\Delta N_i)} = D_i + \Delta N_i \cdot \Delta D_i. \quad (4.72)$$

The fatigue damage of the previous computation steps D_i as well as the particular interval ΔD_i is obtained by an explicit Euler method. The block size ΔN_i to summarize several load cycles at each time is chosen adaptively.

Within the present work, a time-cycle transfer scheme is developed, which strongly resembles the cycle jump scheme. As (4.66) reveals a certain interval of cycles dN that leads to a respective evolution of ψ_p , the fatigue damage is obviously given explicitly in terms of cycles. Suppose a constant block size per time $\frac{\Delta N}{\Delta t}$, the damage evolution for the current simulation step can be obtained by evaluating (4.66) as

$$D_f^i = D_f^{(i-1)} + dD_f(\Delta t_i). \quad (4.73)$$

Under this assumption the phase field evolution equation may be transferred from the time to the cycle domain conveniently by chain rule differentiation. Consequently, the evolution equation for the phase field model for fracture taking into account cyclic fatigue effects is

reformulated in terms of cycles such that

$$\frac{ds}{dN} = -\hat{M} \left\{ g(s)' \frac{1}{2} \boldsymbol{\varepsilon} : [\mathbf{C}\boldsymbol{\varepsilon}] - \mathcal{G}_c \left(2\epsilon \nabla \cdot \nabla s - \frac{s-1}{2\epsilon} \right) + h(s)' P(D_f) \right\}, \quad (4.74)$$

with the mobility in the cycle domain

$$\hat{M} = M \cdot \left(\frac{\Delta N}{\Delta t} \right)^{-1}. \quad (4.75)$$

The fatigue damage is updated for every simulation step according to the scheme introduced above. One must mention, that in order to ensure a reliable convergence behavior, adaptive adjustment of the step size must be implemented, as otherwise the simulation may break down in case of a rapid increase of the $P(D_f)$ contribution. Hence, the number of cycles treated within a single simulation step is controlled by the current computational stability. The handling of the load cycles as it is proposed within the present work is illustrated within Figure 4.13. Assuming constant amplitudes, the actual cyclic load sequence $F(t)$ applied to the structure is represented by a load that remains constant after the initial ramp up with a magnitude equal to the maximum force value of the cycles. The blocks ΔN_i correspond to the particular simulation steps. As a key difference to other approaches, where loading and unloading for every single cycle is explicitly simulated as e.g. Alessi et al., 2017 the number of cycles that can be computed is significantly higher by the proposed cycle jump approach.

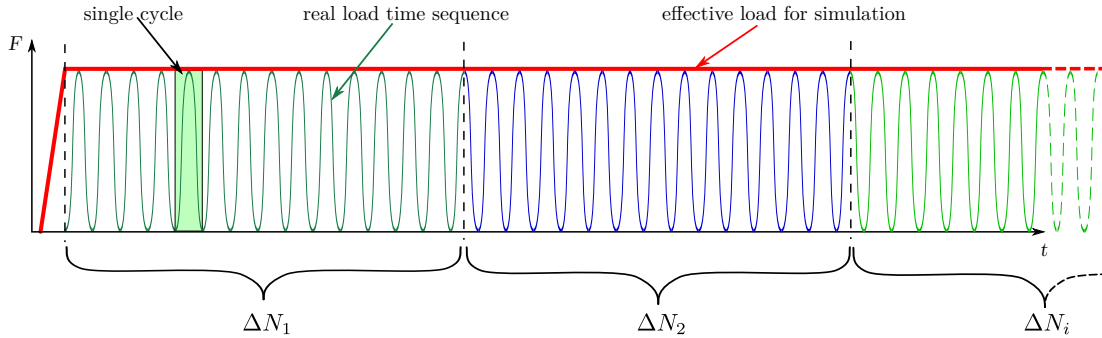


FIGURE 4.13: Schematic illustration of simulation cyclic resolved simulation scheme for fatigue crack growth simulations.

4.2.6 Variation of Mean Stress and Stress Ratio

The description of the damage interval (4.66) restricts the applicability of the phase field model to constant amplitude loading of a sequence with a zero minimal load (see Figure 4.13). However, real load time sequences are much more complex as they generally reveal a random character with alternating mean loads and load minima. Certainly, quantities like the amplitude of the cycles and also the mean load has a crucial effect on the fatigue crack growth behavior. Therefore, these quantities have to be taken into account by the model formulation of the fatigue damage increment. The most common factor to

quantify load cycles of sequences regarding their characteristic loads is the stress ratio

$$R = \frac{\sigma_{\min}}{\sigma_{\max}}, \quad (4.76)$$

with σ_{\min} and σ_{\max} being the respective load minimum and maximum. A slightly different quantification is applied in the following by

$$L = \frac{\tilde{\sigma}_{\text{mean}}}{\tilde{\sigma}} \quad (4.77)$$

as the ratio of the mean of the driving stress with respect to maximum driving stress $\tilde{\sigma}$. This ratio may also be expressed in terms of the external load. Within a small strain setting and linear elasticity these ratios coincide and therefore the mean driving stress can be expressed with

$$\tilde{\sigma}_{\text{mean}} = \tilde{\sigma} \frac{F_{\text{mean}}}{F_{\text{max}}} = \tilde{\sigma} L. \quad (4.78)$$

Accordingly, the appropriate amplitude value to enter the damage increment (4.66) can be expressed by means of the load ratio L . The respective increment of fatigue damage is then expressed as

$$dD_f = (n^D)^{-1} \left(\frac{\tilde{\sigma}(\varepsilon)(1-L)}{f(L)} \right)^k dN, \quad (4.79)$$

where the threshold stress $f(L)$ is proposed as function

$$f(L) = A_D(1-L)^{\bar{\gamma}}. \quad (4.80)$$

In order to mimic mean stress effects and amplitudes below that threshold are not taken into account. Note that this kind of function for $f(L)$ is proposed for a practical reason. The numerical results of section 6.2.2 show an accurate behavior with this function. It is not claimed that this function provides a general method for any material. But the model generally allows for arbitrary functions for the threshold stress in order to properly fit a certain behavior.

For the cycle resolved simulation scheme, this more general damage increment for various amplitude loading means basically that the effective load function is not constant but varies over time. In other words, the envelope of the load time history is traced by a proportional load function. The load factor L is varied according to the alternating cycle characteristics.

Chapter 5

Finite Element Implementation

The Finite Element Method (FEM) is applied in order to approximate the solution of the governing set of partial differential equations. In general, this set consists of the mechanical equilibrium and the evolution equation for the phase field. These equations and the respective modifications were introduced in the previous sections. An implementation into a FEM solution scheme requires the approximation of the underlying domain by the assembly

$$\Omega \approx \Omega^h = \bigcup_{e=1}^{n_e} \Omega_e, \quad (5.1)$$

of n_e finite elements, i.e. the domain is decomposed into smaller parts of finite size. Within these finite elements the field quantities are approximated (see Figure 5.1). The discrete nonlinear system can not be solved directly. It must be linearized and the solution is then obtained by iterative procedures. If the problem reveals a temporal dependency, as it is the case for the phase field evolution (4.15) and (4.74), a time integration scheme must be employed. The description of all these steps for the introduced phase field frameworks is the focus of the current chapter. The implementation is done along the line of corresponding textbooks as e.g. Bathe, 1996, Wriggers, 2001, Zienkiewicz and Taylor, 2001. In some parts, the derivation for the two different phase field models for anisotropic fracture resistance and fatigue crack growth coincides. Therefore, a separated description of the underlying equations will be outlined only when the two models deviate. The system of equations is generally solved for the displacements and the phase field variable utilizing a monolithic scheme. In contrast to staggered solution schemes, where the phase field variable and the displacements are computed in separated iteration loops (see e.g. Miehe et al., 2010a), this rather conservative approach solves the system for all unknowns within a single solution step. The implementation is presented for the two dimensional case.

5.1 Spatial Discretization of Governing Equations

5.1.1 Weak Forms

The governing differential equation for the crack phase field is a multi valued equation as it consists of the mechanical force balance and the evolution equation for the phase field. Accordingly, the boundary value problem is always governed by a set of two equations with the unknowns $\mathbf{u}(\mathbf{x}, t)$ and $s(\mathbf{x}, t)$. For instance, the original phase field model for brittle

fracture by Kuhn and Müller, 2010 yields the set of differential equations

$$\begin{bmatrix} \nabla \cdot & 0 \\ 0 & \frac{1}{M} \frac{d}{dt} + 2W + \frac{\mathcal{G}_c}{2\epsilon} - \mathcal{G}_c 2\epsilon \Delta \end{bmatrix} \begin{bmatrix} \boldsymbol{\sigma}(\mathbf{u}) \\ s \end{bmatrix} = \begin{bmatrix} \mathbf{0} \\ \frac{\mathcal{G}_c}{2\epsilon} \end{bmatrix}, \quad (5.2)$$

where volume forces are neglected, W represents the linear elastic strain energy density and the Laplace operator $\Delta = \nabla \cdot \nabla$ is used. It is, however, generally problematic to employ the strong forms of the governing equations, since this requires a boundary value problem to be smooth over the entire domain. The mechanical equilibrium for example contains the gradient of the stress tensor and accordingly differentiability must be ensured. It is therefore common to use a weak formulation of the governing equations. The weak form of an vector valued problem is obtained by multiplying the differential equation with a potentially vector valued test function $\delta \mathbf{v}$ and subsequent integration over the domain:

$$\mathbf{0} = \int_{\Omega} \mathbf{f}(\mathbf{v}) \cdot \delta \mathbf{v} \, d\Omega. \quad (5.3)$$

The idea is then to consider every non-vanishing possible test function $\delta \mathbf{v}$. If (5.3) holds for all admissible test functions, the correct solution \mathbf{v} is found. As indicated above, the weak form provides the general basis for a finite element implementation regardless of the specific physical subject. Note that this procedure is also referred to as the principle of virtual displacements, see Bathe, 1996.

According to the above scheme the weak form of the mechanical balance law (2.23) can be derived. Utilizing the virtual test function $\delta \mathbf{u}$ and applying partial integration yields

$$0 = \int_{\Omega} \delta \mathbf{u} \nabla \boldsymbol{\sigma} \, d\Omega = - \int_{\Omega} \boldsymbol{\sigma} : \nabla \delta \mathbf{u} \, d\Omega + \int_{\partial\Omega^t} \delta \mathbf{u} \cdot \mathbf{t}^* \, dS, \quad (5.4)$$

where body forces are neglected and Cauchy's theorem (2.16) is used in the last term to incorporate the prescribed traction vector \mathbf{t}^* and $\partial\Omega^t$ is the fraction of $\partial\Omega$, which bears traction boundary conditions. For simplicity body forces are neglect. The integrand of the second integral may be transformed to be expressed by virtual strains instead of displacements via

$$0 = - \int_{\Omega} \underbrace{\boldsymbol{\sigma} : \delta \boldsymbol{\varepsilon}}_{\boldsymbol{\sigma} : \frac{1}{2}(\nabla \delta \mathbf{u} + \nabla \delta \mathbf{u}^T)} \, d\Omega + \int_{\partial\Omega^t} \delta \mathbf{u} \cdot \mathbf{t}^* \, dS. \quad (5.5)$$

Except for the expression of the stress $\boldsymbol{\sigma}$, this weak form generally holds for the phase field models proposed within this work. However, the particular second part of the set of governing equations, namely the weak forms of the phase field evolution equation, obviously deviate and are to be introduced separately. For the model accounting for a directionality of the fracture resistance, introduced in section 4.1, the respective weak form of the evolution

(4.15) is

$$0 = - \int_{\Omega} \left[\delta s \frac{\dot{s}}{M} + \delta s \frac{\partial \psi_e^+}{\partial s} - \delta s \mathcal{G}_c \frac{1-s}{2\epsilon} + \mathcal{G}_c 2\epsilon \nabla \delta s \cdot \boldsymbol{\Phi} \nabla s \right] dV, \quad (5.6)$$

with

$$\frac{\partial \psi_e^+}{\partial s} = g(s)' \left(\frac{K}{2} \langle \text{tr}(\boldsymbol{\epsilon}) \rangle_+^2 + \mu \boldsymbol{\epsilon}_D^2 \right), \quad (5.7)$$

where again partial integration is applied. The corresponding surface integral for the last term vanishes due to the homogeneous Neumann type boundary condition $\nabla s \cdot \mathbf{n} = 0$ at $\partial\Omega$. For the anisotropic model tension compression distinction of the stresses is implemented, since for several numerical examples, that were run within the underlying study this is decisive. Specifically, the volumetric deviatoric split of the strain energy (3.48) proposed by Amor et al., 2009 is applied due to the relatively low effort in terms of implementation within the used monolithic simulation scheme. For the phase field model for fatigue fracture the corresponding weak form of the evolution (4.74) is given by

$$0 = - \int_{\Omega} \left[\delta s \left(\frac{1}{\tilde{M}} \frac{ds}{dN} + g(s)'W + h(s)'P(D_f) + \mathcal{G}_c \frac{s-1}{2\epsilon} \right) + 2\mathcal{G}_c \epsilon \nabla s \cdot \nabla \delta s \right] dV. \quad (5.8)$$

5.1.2 Isoparametric Concept

For all models presented in this work a small deformation setting and a linear elastic material model is used. However, as (5.6) and (5.8) indicate, the coupled system is nonlinear due to the phase field evolution equation. In order to solve such problems, the state of equilibrium must be found for the body under consideration with respect to the applied loads, which may vary with time. This is expressed by the relation

$$\mathbf{0} = \mathbf{F}(t) - \mathbf{P}(t), \quad (5.9)$$

where $\mathbf{F}(t)$ is considered the vector of the external loads, which contains body forces, surface loads and also inertia forces for dynamic systems. Contrary, the vector $\mathbf{P}(t)$ contains the internal forces corresponding to the respective degrees of freedom. The contributions to these vectors for a particular problem are found from the weak forms. These equations may be discretized in the first place, which is done by utilizing the isoparametric concept. The principle to approximate both, the geometry and the field quantities of the particular physical problem by means of the same shape functions H_I is referred to as the isoparametric concept. The index I refers to the element nodes with $I = 1, \dots, n$, where n is the number of nodes per finite element. These shape functions are defined within the reference configuration Ω_{\square} (see right illustration in Figure 5.1) of the respective finite element and enable the approximation of relevant quantities within an element by

$$\mathbf{x}_e = \sum_{I=1}^n H_I \mathbf{x}_I, \quad (5.10)$$

where \mathbf{x}_I are the nodal values. The definition of these shape functions is based on a reference finite element. Throughout this study, four node quadrilateral elements are used.

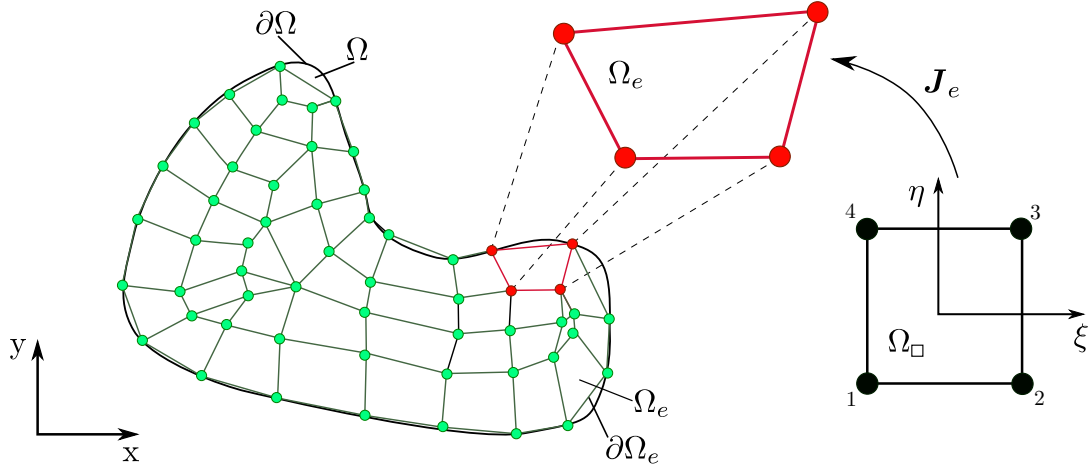


FIGURE 5.1: Schematic illustration of discretization of a body Ω with indication of isoparametric approach.

Figure 5.1 shows this element type and indicates the isoparametric mapping of the reference configuration of the finite element to its spatial configuration. With respect to the $\xi - \eta$ reference system, the underlying shape functions of four node elements are

$$H_I(\xi, \eta) = \frac{1}{2}(1 + \xi_I \xi) \frac{1}{2}(1 + \eta_I \eta), \quad (5.11)$$

with coordinates ξ_I and η_I of the corresponding nodes, i.e.

$$(\xi_1, \eta_1) = (-1, -1), (\xi_2, \eta_2) = (1, -1), (\xi_3, \eta_3) = (1, 1), (\xi_4, \eta_4) = (-1, 1), \quad (5.12)$$

according to the illustration in Figure 5.1. Derivatives of field quantities must be calculated within the finite element approximation. As the field quantities depend on the shape functions, the respective derivatives require derivatives of the shape functions. The common procedure is to perform this differentiation within the reference configuration Ω_\square and transform the results to the spatial configuration Ω_e with

$$\begin{bmatrix} \frac{\partial H_I}{\partial x} \\ \frac{\partial H_I}{\partial y} \end{bmatrix} = \underbrace{\begin{bmatrix} \frac{\partial x}{\partial \xi} & \frac{\partial x}{\partial \eta} \\ \frac{\partial y}{\partial \xi} & \frac{\partial y}{\partial \eta} \end{bmatrix}^{-1}}_{\mathbf{J}_e^{-1}} \begin{bmatrix} \frac{\partial H_I}{\partial \xi} \\ \frac{\partial H_I}{\partial \eta} \end{bmatrix}, \quad (5.13)$$

with \mathbf{J}_e being the Jacobian matrix. Within this finite element approximation integrals of e.g. the weak forms can be evaluated by the transformation

$$\int_{\Omega} (\dots) dV \approx \bigcup_{e=1}^{n_e} \int_{\Omega_e} (\dots) dV = \bigcup_{e=1}^{n_e} \int_{\Omega_\square} (\dots) d\Omega, \quad (5.14)$$

with the relation

$$dV = \det(\mathbf{J}_e) d\Omega, \quad (5.15)$$

which demands $\det(\mathbf{J}_e) > 0$. Accordingly, this also constrains the ordering of nodes of the finite element as indicated in Figure 5.1.

5.1.3 Numerical Quadrature

Integrals over Ω_e must be calculated in order to obtain the residual, the tangent stiffness and damping matrix, which will be introduced in the following sections. Using the relationship in (5.15) the respective integrals of functions $f(\mathbf{x})$ may be transformed into the parameter space of Ω_\square and accordingly

$$\int_{\Omega_e} f(\mathbf{x}) \, dV = \int_{-1}^{+1} \int_{-1}^{+1} f(\boldsymbol{\xi}) \det(\mathbf{J}_e) \, d\xi d\eta, \quad (5.16)$$

where the parameterization is in agreement with (5.12). The integration is performed numerically using the approximation

$$\int_{-1}^{+1} \int_{-1}^{+1} f(\boldsymbol{\xi}) \det(\mathbf{J}_e) \, d\xi d\eta \approx \sum_{p=1}^{n_p} f(\boldsymbol{\xi}) \det(\mathbf{J}_e(\xi_p, \eta_p)) w_p, \quad (5.17)$$

where w_p are integration weights. The corresponding coordinates ξ_p and η_p are to be chosen at specific locations in order to achieve optimal accuracy. However, different patterns for the distribution of these integration points can be applied. For many applications the Gauss-Integration was found to yield most accurate results. It is therefore used in FEM. Within this work the number of integration points per finite element n_p is set to four. The corresponding values for the four node element are

$$\begin{aligned} (\xi_1^G, \eta_1^G) &= (-1/\sqrt{3}, -1/\sqrt{3}), & (\xi_2^G, \eta_2^G) &= (+1/\sqrt{3}, -1/\sqrt{3}), \\ (\xi_3^G, \eta_3^G) &= (+1/\sqrt{3}, +1/\sqrt{3}), & (\xi_4^G, \eta_4^G) &= (-1/\sqrt{3}, +1/\sqrt{3}), \end{aligned} \quad (5.18)$$

with integration weight $w_p = 1$ at all points. Further sets of integration points and weights are summarized in e.g. Zienkiewicz and Taylor, 2001.

5.1.4 Spatial Discretization

In order to discretize the underlying physical model the body of interest is discretized by finite elements. Field quantities as e.g. displacements are approximated through the shape functions and the particular field values at the nodal points of the finite elements, just like the geometry. All numerical investigations are conducted for two dimensional problems with the assumption of plane strain. The Voigt notation for the strain and stress tensor yields

$$\boldsymbol{\varepsilon} = \begin{bmatrix} \varepsilon_{xx} \\ \varepsilon_{yy} \\ 2\varepsilon_{xy} \end{bmatrix} \quad \text{and} \quad \boldsymbol{\sigma} = \begin{bmatrix} \sigma_{xx} \\ \sigma_{yy} \\ \sigma_{xy} \end{bmatrix}. \quad (5.19)$$

The isotropic fourth order stiffness tensor is given by

$$\mathbb{C} = \begin{bmatrix} \lambda + 2\mu & \lambda & 0 \\ \lambda & \lambda + 2\mu & 0 \\ 0 & 0 & \mu \end{bmatrix}, \quad (5.20)$$

with Lamé parameters λ and μ . In the phase field models the unknown field quantities are the displacements \mathbf{u} and the phase field variable s . By means of the isoparametric concept these quantities can be expressed within an element Ω_e via the shape functions $H_I^{\mathbf{u}}$ and H_I^s

$$\mathbf{u}_e(\mathbf{x}) = \sum_{I=1}^n H_I^{\mathbf{u}} \mathbf{u}_I \quad \text{and} \quad s_e(\mathbf{x}) = \sum_{I=1}^n H_I^s s_I \quad (5.21)$$

over the nodes I of the particular element, where \mathbf{u}_I and s_I are the nodal point values of the corresponding fields and $H_I^{\mathbf{u}}$ as well as H_I^s are shape functions. In an analog way the virtual test functions are discretized

$$\delta \mathbf{u}_e(\mathbf{x}) = \sum_{I=1}^n H_I^{\delta \mathbf{u}} \delta \mathbf{u}_I \quad \text{and} \quad \delta s_e(\mathbf{x}) = \sum_{I=1}^n H_I^{\delta s} \delta s_I. \quad (5.22)$$

The model equations contain spatial derivatives. For this reason the differential operator matrices

$$\mathbf{B}_I^{\mathbf{u}} = \begin{bmatrix} H_{I,x}^{\mathbf{u}} & 0 \\ 0 & H_{I,y}^{\mathbf{u}} \\ H_{I,y}^{\mathbf{u}} & H_{I,x}^{\mathbf{u}} \end{bmatrix} \quad \text{and} \quad \mathbf{B}_I^{\delta \mathbf{u}} = \begin{bmatrix} H_{I,x}^{\delta \mathbf{u}} & 0 \\ 0 & H_{I,y}^{\delta \mathbf{u}} \\ H_{I,y}^{\delta \mathbf{u}} & H_{I,x}^{\delta \mathbf{u}} \end{bmatrix} \quad (5.23)$$

as well as

$$\mathbf{B}_I^s = \begin{bmatrix} H_{I,x}^s \\ H_{I,y}^s \end{bmatrix} \quad \text{and} \quad \mathbf{B}_I^{\delta s} = \begin{bmatrix} H_{I,x}^{\delta s} \\ H_{I,y}^{\delta s} \end{bmatrix}, \quad (5.24)$$

where $(\cdot), v$ represent the respective spatial derivatives $\frac{\partial(\cdot)}{\partial v}$. Utilizing these matrices the element values for the strains and the spatial gradient of the phase field variable are described by

$$\boldsymbol{\varepsilon}_e(\mathbf{x}) = \sum_{I=1}^n \mathbf{B}_I^{\mathbf{u}} \mathbf{u}_I \quad \text{and} \quad \delta \boldsymbol{\varepsilon}_e(\mathbf{x}) = \sum_{I=1}^n \mathbf{B}_I^{\delta \mathbf{u}} \delta \mathbf{u}_I, \quad (5.25)$$

as well as

$$\nabla s_e = \sum_{I=1}^n \mathbf{B}_I^s s_I \quad \text{and} \quad \delta \nabla s_e = \sum_{I=1}^n \mathbf{B}_I^{\delta s} s_I. \quad (5.26)$$

Note the distinction between shape functions for virtual quantities and real quantities in order to provide a general description. As it is the case for most FEM formulations, identical shape functions are used for both, real and virtual quantities.

The discretization of the weak form of the mechanical equilibrium can finally be obtained by inserting the discretization from above into (5.5) and accordingly

$$0 = \sum_{I=1}^n \delta \mathbf{u}_I^T \left[\underbrace{- \int_{\Omega_e} \mathbf{B}_I^{\delta \mathbf{u}^T} \boldsymbol{\sigma}_e \, dV}_{\mathbf{P}_I^{\mathbf{u}}} + \underbrace{\int_{\partial \Omega_e} H_I^{\delta \mathbf{u}} \mathbf{t}_e^* \, dA}_{\mathbf{F}_I^{\mathbf{u}}} \right] = \sum_{I=1}^n \delta \mathbf{u}_I^T \mathbf{R}_I^{\mathbf{u}}. \quad (5.27)$$

The expression within the brackets is referred to as the nodal residual of the mechanical balance law $\mathbf{R}_I^{\mathbf{u}}$, with the first and the second integral representing internal and external forces, respectively. In a similar way the discrete variables are incorporated into the weak forms of the respective phase field evolution equations. Thus, the discretization of the anisotropic model is

$$0 = \sum_{I=1}^n \delta s_I \int_{\Omega_e} \left[H_I^{\delta s} \left\{ \frac{\dot{s}_e}{M} + g(s_e)' \left(\frac{K}{2} \langle \text{tr}(\boldsymbol{\varepsilon}_e) \rangle_+^2 + \mu \boldsymbol{\varepsilon}_{De}^2 \right) - \mathcal{G}_c \frac{1-s_e}{2\epsilon} \right\} \right. \\ \left. + 2 \epsilon \mathbf{B}_I^{\delta s^T} (\boldsymbol{\Phi} \nabla s_e) \right] dV = \sum_{I=1}^n \delta s_I R_I^{s,\text{an}} = \sum_{I=1}^n \delta s_I P_I^{s,\text{an}}, \quad (5.28)$$

where the deviatoric part of the strain tensor $\boldsymbol{\varepsilon}_{De}$ is described by

$$\boldsymbol{\varepsilon}_{De} = \begin{bmatrix} \varepsilon_{Dxx_e} \\ \varepsilon_{Dyy_e} \\ \varepsilon_{Dxy_e} \end{bmatrix} = \mathbb{P} \boldsymbol{\varepsilon}_e, \quad (5.29)$$

with the operator matrix

$$\mathbb{P} = \begin{bmatrix} 2/3 & -1/3 & 0 \\ -1/3 & 2/3 & 0 \\ 0 & 0 & 1 \end{bmatrix}. \quad (5.30)$$

A similar procedure is applied to (5.8) in order to find the corresponding discretization

$$0 = \sum_{I=1}^n \delta s_I \int_{\Omega_e} \left[H_I^{\delta s} \left\{ \hat{M}^{-1} \frac{ds}{dN_e} + g(s_e)' \boldsymbol{\varepsilon}_e^T \mathbb{C} \boldsymbol{\varepsilon}_e + h(s_e)' P(D_f) - \mathcal{G}_c \frac{1-s_e}{2\epsilon} \right\} \right. \\ \left. + 2 \mathcal{G}_c \epsilon \mathbf{B}_I^{\delta s^T} \nabla s_e \right] dV = \sum_{I=1}^n \delta s_I R_I^{s,\text{fat}} = \sum_{I=1}^n \delta s_I P_I^{s,\text{fat}}. \quad (5.31)$$

The integrals of (5.27), (5.28) and (5.31) are referred to as the element residual assigned to node I . The contribution originating from the mechanical balance law consists of internal forces $\mathbf{P}_I^{\mathbf{u}}$ and external forces $\mathbf{F}_I^{\mathbf{u}}$. In contrast, the contribution of the phase field evolution equation solely consists of internal forces. Together, these quantities form the nodal residual vectors

$$\mathbf{R}_I^{\text{an}} = \left[\mathbf{R}_I^{\mathbf{u}^T}, R_I^{s,\text{an}} \right]^T \quad \text{and} \quad \mathbf{R}_I^{\text{fat}} = \left[\mathbf{R}_I^{\mathbf{u}^T}, R_I^{s,\text{fat}} \right]^T \quad (5.32)$$

for the phase field models. By the assembly of all these nodal residual vectors the respective global residuals \mathbf{R}^{an} and \mathbf{R}^{fat} are obtained. In a similar way the nodal values of the virtual test functions $\delta \mathbf{u}_I$ and δs_I are assembled to a global vector $\delta \mathbf{U}$. Consequently, the global form of the governing equation is

$$0 = \delta \mathbf{U} \mathbf{R}^{\text{an}} \quad \text{and} \quad 0 = \delta \mathbf{U} \mathbf{R}^{\text{fat}} \quad (5.33)$$

in order to fulfill (5.27) together with (5.28) or (5.31), respectively. For arbitrary values of the test functions, the residual must vanish in order to obtain a solution of a boundary value problem at a certain time.

5.2 Solution of the Nonlinear System and Time Integration

5.2.1 General Solution Procedure

Equations (5.33) represent a nonlinear system of equations, for which the unknown variables s and \mathbf{u} must be determined accurately at every time step. It is convenient to employ iterative solution procedures in order to approximate the solution to a certain degree of satisfaction. The alternative is to deal with nonlinear functional analysis, which is extremely complex. The solution also depends on the first time derivative of the phase field order parameter, rendering a first order transient problem of the form

$$\mathbf{0} = \mathbf{R}(t) = \mathbf{F}(t) - \mathbf{P}(\mathbf{U}(t), \dot{\mathbf{U}}(t)), \quad (5.34)$$

with \mathbf{U} representing the set of degrees of freedom and its time derivative $\dot{\mathbf{U}}$, which is in the present case

$$\mathbf{U} = [\mathbf{u}^T, s]^T \quad \text{and} \quad \dot{\mathbf{U}} = [\mathbf{0}^T, \dot{s}]^T, \quad (5.35)$$

as only the time derivative of the phase field variable is relevant for the solution. However, time integration of (5.34) must be performed, where a variety of different methods is available. These methods are categorized according to their explicit or implicit character and by the number of time steps being involved. Assuming t_{k+1} is the time, for which a solution is to be determined, explicit methods solely involve steps t_k or lower. Implicit approaches also take the solution at t_{k+1} itself into account. Implicit approaches are more complex, however, they benefit in terms of stability and possible time step size. Therefore, the implicit Euler method also referred to as backward Euler method was utilized in this work. Generally, the goal is to find $\dot{\mathbf{U}}_{t_{k+1}}$ from

$$\mathbf{0} = \mathbf{R}_{t_{k+1}} = \mathbf{F}_{t_{k+1}} - \mathbf{P}(\mathbf{U}_{t_{k+1}}, \dot{\mathbf{U}}_{t_{k+1}}) \quad (5.36)$$

and as stated before the new solution $\mathbf{U}_{t_{k+1}}$ is used to describe the rate by

$$\dot{\mathbf{U}}_{t_{k+1}} = \frac{\mathbf{U}_{t_{k+1}} - \mathbf{U}_{t_k}}{\Delta t}. \quad (5.37)$$

This implicit formulation requires an iterative solution as e.g. the Newton-Raphson scheme. This scheme is based on a Taylor series expansion of the residual with respect to \mathbf{U} , which

for a given iteration $(i - 1)$ yields

$$\mathbf{R}(\mathbf{U}) = {}_{(i-1)}\mathbf{R}_{t_{k+1}} + \left. \frac{\partial \mathbf{R}}{\partial \mathbf{U}} \right|_{{}_{(i-1)}\mathbf{U}_{t_{k+1}}} \cdot \underbrace{(\mathbf{U} - {}_{(i-1)}\mathbf{U}_{t_{k+1}})}_{\Delta \mathbf{U}} + \mathcal{O}. \quad (5.38)$$

Neglecting higher order terms \mathcal{O} , inserting (5.36) into this expansion and respecting $\mathbf{R} = \mathbf{0}$ in case of a solution, one finds

$$\left. \frac{\partial \mathbf{P}}{\partial \mathbf{U}} \right|_{{}_{(i-1)}\mathbf{U}_{t_{k+1}}} \cdot {}_i\Delta \mathbf{U} = \mathbf{F}_{t_{k+1}} - {}_{(i-1)}\mathbf{P}_{t_{k+1}} \quad (5.39)$$

as contributions of the external forces do not depend on the unknowns \mathbf{U} . Within a iterative solution scheme the incremental solution vector is

$${}_i\Delta \mathbf{U} = {}_i\mathbf{U} - {}_{(i-1)}\mathbf{U}. \quad (5.40)$$

The derivative of the internal force vector with respect to the displacements at a given iteration yields

$$\frac{\partial \mathbf{P}}{\partial \mathbf{U}} = \frac{\partial \mathbf{P}}{\partial \mathbf{U}} + \frac{\partial \mathbf{P}}{\partial \dot{\mathbf{U}}} \frac{\partial \dot{\mathbf{U}}}{\partial \mathbf{U}} = \frac{\partial \mathbf{P}}{\partial \mathbf{U}} + \frac{1}{\Delta t} \frac{\partial \mathbf{P}}{\partial \dot{\mathbf{U}}}, \quad (5.41)$$

in consideration of the Euler approximation (5.37). The two contributions in (5.41) are commonly denoted as the tangent stiffness matrix

$$\mathbf{K} = \frac{\partial \mathbf{P}}{\partial \mathbf{U}} \quad (5.42)$$

and the tangent damping matrix

$$\mathbf{D} = \frac{\partial \mathbf{P}}{\partial \dot{\mathbf{U}}}. \quad (5.43)$$

With these definitions the so called system matrix \mathbf{S} can be formed and the solution scheme for a given time step on a global level contains the evaluation of

$${}_{(i-1)}\mathbf{R}_{t_{k+1}} = \mathbf{F}_{t_{k+1}} - \underbrace{\left({}_{(i-1)}\mathbf{K}_{t_{k+1}} + \frac{1}{\Delta t} {}_{(i-1)}\mathbf{D}_{t_{k+1}} \right)}_{\mathbf{S}} {}_i\Delta \mathbf{U}_{t_{k+1}}, \quad (5.44)$$

and a solution is found once $\|{}_i\mathbf{R}_{t_{k+1}}\| \leq \text{TOL}$, where TOL is a defined tolerance. Otherwise the procedure is repeated with ${}_{(i-1)}\mathbf{U} \leftarrow {}_i\mathbf{U}$.

5.2.2 Derivation of Associated System Matrix

For the two presented phase field models the nodal contributions are computed on the element level. In the following the derivation of the respective matrices

$$\mathbf{K}_{IJ_e} = \begin{bmatrix} \mathbf{K}_{IJ_e}^{\text{uu}} & \mathbf{K}_{IJ_e}^{\text{us}} \\ \mathbf{K}_{IJ_e}^{\text{su}} & \mathbf{K}_{IJ_e}^{\text{ss}} \end{bmatrix} \quad \text{and} \quad \mathbf{D}_{IJ_e} = \begin{bmatrix} \mathbf{0} & \mathbf{0} \\ \mathbf{0} & \mathbf{D}_{IJ_e}^{\text{ss}} \end{bmatrix} \quad (5.45)$$

are described. The matrices contain derivatives of the internal forces $\mathbf{P}_I^{\mathbf{u}}$, $P_I^{s,\text{an}}$ and $P_I^{s,\text{fat}}$ with respect to the nodal variables \mathbf{u}_I and s_I . So far, the stresses in $\mathbf{P}_I^{\mathbf{u}}$ (5.27) were not defined in detail. The characteristic of the stiffness matrices depends on these stresses. In case of the model for fracture toughness anisotropies tension compression differentiation is incorporated, which renders the stress as

$$\boldsymbol{\sigma} = \frac{\partial(\psi_e^+ + \psi_e^-)}{\partial \boldsymbol{\varepsilon}} = (g(s) + \eta) \left[K \langle \text{tr}(\boldsymbol{\varepsilon}) \rangle_+ \mathbf{1} + 2\mu \boldsymbol{\varepsilon}_D \right] + K \langle \text{tr}(\boldsymbol{\varepsilon}) \rangle_- \mathbf{1}, \quad (5.46)$$

with the Voigt operator $\mathbf{1} = [1, 1, 0]^T$. Accordingly, the particular sub matrices of $\mathbf{K}_{IJ,e}$, which contribute to the global tangent stiffness matrix can be derived as

$$\mathbf{K}_{IJ,e}^{\mathbf{uu}} = \frac{\partial \mathbf{P}_{I,e}^{\mathbf{u}}}{\partial \mathbf{u}_J} = \int_{\Omega_e} \mathbf{B}_I^{\delta \mathbf{u} T} \left\{ (g(s_e) + \eta) \left[K (\mathbf{1}^T \mathbf{1})_+ + 2\mu \mathbb{P} \right] + K (\mathbf{1}^T \mathbf{1})_- \right\} \mathbf{B}_J^{\mathbf{u}} \, dV, \quad (5.47)$$

$$\mathbf{K}_{IJ,e}^{\mathbf{us}} = \frac{\partial \mathbf{P}_{I,e}^{\mathbf{u}}}{\partial s_J} = \int_{\Omega_e} \mathbf{B}_I^{\delta \mathbf{u} T} H_J^s g(s_e)' \left[K \langle \text{tr}(\boldsymbol{\varepsilon}_e) \rangle_+ \mathbf{1} + 2\mu \boldsymbol{\varepsilon}_{D_e} \right] \, dV, \quad (5.48)$$

$$\mathbf{K}_{IJ,e}^{\mathbf{su}} = \frac{\partial \mathbf{P}_{I,e}^s}{\partial \mathbf{u}_J} = \int_{\Omega_e} H_I^{\delta s} g(s_e)' \left[K \langle \text{tr}(\boldsymbol{\varepsilon}_e) \rangle_+ \mathbf{1} + 2\mu \boldsymbol{\varepsilon}_{D_e} \right] \mathbf{B}_J^{\mathbf{u}} \, dV, \quad (5.49)$$

$$\mathbf{K}_{IJ,e}^{ss} = \frac{\partial \mathbf{P}_{I,e}^s}{\partial s_J} = \int_{\Omega_e} \left\{ H_I^{\delta s} H_J^s g(s_e)'' \left\{ \left[\frac{K}{2} \langle \text{tr}(\boldsymbol{\varepsilon}_e) \rangle_+^2 + \mu \boldsymbol{\varepsilon}_{D_e}^2 \right] + \mathcal{G}_c \frac{1}{2\epsilon} \right\} + 2\mathcal{G}_c \epsilon \mathbf{B}_I^{\delta s} \boldsymbol{\Phi} \mathbf{B}_J^s \right\} \, dV. \quad (5.50)$$

Also the only non zero component of the element damping matrix is given by

$$D^{ss} = \frac{\partial P_{I,e}^s}{\partial \dot{s}_J} = \int_{\Omega_e} H_I^{\delta s} H_J^s M^{-1} \, dV. \quad (5.51)$$

The compression tension distinction is not needed for the model of fatigue fracture, as it will be shown in the subsequent result chapter. Therefore, it was not implemented in this model and (4.68) sufficiently pictures the stresses. Nevertheless, the implementation can become complex due to the driving quantity $\tilde{\sigma}$, which may depend on the particular load case. If normal stress in vertical direction is assumed then a proper Voigt notation is

$$\tilde{\sigma} = \mathbf{1}_v^T \mathbb{C} \boldsymbol{\varepsilon} \quad (5.52)$$

with $\mathbf{1}_v = [0, 1, 0]^T$. Incorporating this driving force, the derivative in (4.68) becomes

$$\frac{\partial \tilde{\sigma}}{\partial \boldsymbol{\varepsilon}} = \mathbf{1}_v^T \mathbb{C}. \quad (5.53)$$

As discussed in section 4.2.4, a more general description of fatigue crack growth can be realized by utilizing the first principal stress as driving stress quantity. This can be implemented by reformulating (4.71) in Voigt notation, which leads to

$$\tilde{\sigma} = \mathbf{1}_+^T \mathbb{C} \boldsymbol{\varepsilon} + \left[(\mathbf{1}_-^T \mathbb{C} \boldsymbol{\varepsilon})^2 + (\mathbf{1}_\tau^T \mathbb{C} \boldsymbol{\varepsilon})^2 \right]^{1/2}, \quad (5.54)$$

with the operators $\mathbf{1}_+ = [\frac{1}{2}, \frac{1}{2}, 0]^T$, $\mathbf{1}_- = [\frac{1}{2}, -\frac{1}{2}, 0]^T$ and $\mathbf{1}_\tau = [0, 0, 1]^T$. With these expressions the associated element tangent stiffness matrices for the fatigue model become

$$\mathbf{K}_{IJ}^{\mathbf{uu}} = \frac{\partial \mathbf{P}_{I,e}^{\mathbf{u}}}{\partial \mathbf{u}_J} = \int_{\Omega_e} \left\{ \mathbf{B}_I^{\delta \mathbf{u} T} (g(s_e) + \eta) \mathbb{C} \mathbf{B}_J^{\mathbf{u}} + \mathbf{B}_I^{\delta \mathbf{u} T} \frac{\partial \boldsymbol{\sigma}^{\text{ac}}}{\partial \boldsymbol{\varepsilon}_e} \mathbf{B}_J^{\mathbf{u}} \right\} dV, \quad (5.55)$$

$$\mathbf{K}_{IJ}^{\mathbf{us}} = \frac{\partial \mathbf{P}_{I,e}^{\mathbf{u}}}{\partial s_J} = \int_{\Omega} \mathbf{B}_I^{\delta \mathbf{u} T} H_J^s \left[g(s_e)' \mathbb{C} \boldsymbol{\varepsilon}_e + h(s_e)' \frac{\partial P(D_f)}{\partial \boldsymbol{\varepsilon}_e} \right] dV, \quad (5.56)$$

$$\mathbf{K}_{IJ,e}^{\mathbf{su}} = \frac{\partial \mathbf{P}_{I,e}^s}{\partial \mathbf{u}_J} = \int_{\Omega_e} H_I^{\delta s} \left(g(s_e)' \mathbb{C} \boldsymbol{\varepsilon}_e + h(s_e)' \frac{\partial P(D_f)}{\partial \boldsymbol{\varepsilon}_e} \right)^T \mathbf{B}_J^{\mathbf{u}} dV, \quad (5.57)$$

$$\mathbf{K}_{IJ,e}^{\mathbf{ss}} = \frac{\partial \mathbf{P}_{I,e}^s}{\partial s_J} = \int_{\Omega_e} \left\{ H_I^{\delta s} H_J^s \left(g(s_e)'' \boldsymbol{\varepsilon}^T \mathbb{C} \boldsymbol{\varepsilon}_e + h(s_e)'' P(D_f) + \frac{G_c}{2\varepsilon} \right) + 2\mathcal{G}_c \varepsilon (\mathbf{B}_I^s)^T \mathbf{B}_J^s \right\} dV, \quad (5.58)$$

with the abbreviations

$$\begin{aligned} \frac{\partial \boldsymbol{\sigma}^{\text{ac}}}{\partial \boldsymbol{\varepsilon}_e} &= h(s_e) q b \frac{dNk}{n^D A_D^k} \left[(b-1) \langle D_f - D_{fc} \rangle^{(b-2)} \frac{dNk}{n^D A_D^k} \tilde{\sigma}^{2(k-1)} \frac{\partial \tilde{\sigma}}{\partial \boldsymbol{\varepsilon}_e} \left(\frac{\partial \tilde{\sigma}}{\partial \boldsymbol{\varepsilon}_e} \right)^T \right. \\ &\quad + \langle D_f - D_{fc} \rangle^{(b-1)} (k-1) \tilde{\sigma}^{(k-2)} \frac{\partial \tilde{\sigma}}{\partial \boldsymbol{\varepsilon}_e} \left(\frac{\partial \tilde{\sigma}}{\partial \boldsymbol{\varepsilon}_e} \right)^T \\ &\quad \left. + \langle D_f - D_{fc} \rangle^{(b-1)} \tilde{\sigma}^{(k-1)} \frac{\partial^2 \tilde{\sigma}}{\partial \boldsymbol{\varepsilon}_e^2} \right], \end{aligned} \quad (5.59)$$

$$\frac{\partial P(D_f)}{\partial \boldsymbol{\varepsilon}_e} = q b \langle D_f - D_{fc} \rangle^{(b-1)} \cdot dN \frac{k \tilde{\sigma}(\boldsymbol{\varepsilon})^{(k-1)}}{n^D A_D^k} \frac{d\tilde{\sigma}(\boldsymbol{\varepsilon})}{d\boldsymbol{\varepsilon}_e}, \quad (5.60)$$

$$\frac{\partial \tilde{\sigma}}{\partial \boldsymbol{\varepsilon}_e} = \mathbb{C} \mathbf{1}_+ + \frac{(\mathbf{1}_-^T \mathbb{C} \boldsymbol{\varepsilon}_e) \mathbb{C} \mathbf{1}_- + (\mathbf{1}_\tau^T \mathbb{C} \boldsymbol{\varepsilon}_e) \mathbb{C} \mathbf{1}_\tau}{\left[(\mathbf{1}_-^T \mathbb{C} \boldsymbol{\varepsilon}_e)^2 + (\mathbf{1}_\tau^T \mathbb{C} \boldsymbol{\varepsilon}_e)^2 \right]^{1/2}}, \quad (5.61)$$

as well as

$$\frac{\partial^2 \tilde{\sigma}}{\partial \boldsymbol{\varepsilon}_e^2} = \frac{\mathbb{C} \mathbf{1}_- (\mathbf{1}_-^T \mathbb{C}) + \mathbb{C} \mathbf{1}_\tau (\mathbf{1}_\tau^T \mathbb{C})}{\left[(\mathbf{1}_-^T \mathbb{C} \boldsymbol{\varepsilon}_e)^2 + (\mathbf{1}_\tau^T \mathbb{C} \boldsymbol{\varepsilon}_e)^2 \right]^{1/2}} - \frac{\left[(\mathbf{1}_-^T \mathbb{C} \boldsymbol{\varepsilon}_e) \mathbb{C} \mathbf{1}_- + (\mathbf{1}_\tau^T \mathbb{C} \boldsymbol{\varepsilon}_e) \mathbb{C} \mathbf{1}_\tau \right]^2}{\left[(\mathbf{1}_-^T \mathbb{C} \boldsymbol{\varepsilon}_e)^2 + (\mathbf{1}_\tau^T \mathbb{C} \boldsymbol{\varepsilon}_e)^2 \right]^{3/2}}. \quad (5.62)$$

Finally, the damping matrix can be derived, which is governed by derivatives with respect to $s_{,N}$ due to the transformation into the cycle domain given by (4.74) and (4.75). Vanishing contributions are obtained except for the component

$$D_{IJ}^{ss} = \frac{\partial F_I^s}{\partial s_{,N}} = \int_{\Omega} H_I H_J \hat{M}^{-1} dV. \quad (5.63)$$

Finally, the contributions of the considered element matrices are assembled to the global system matrix

$$\mathbf{R} = \mathbf{F} - \bigcup_{e=1}^{n_e} \sum_{I=1}^n \sum_{J=1}^n \mathbf{S}_{IJ,e} \Delta \mathbf{U}. \quad (5.64)$$

In order to provide a general finite element frame work it is differentiated between shape functions for real quantities and virtual quantities. However, it may be noticed that within all implementations of this study the same shape functions were used for all variables. Using alternative shape functions for both or one type of unknowns may be beneficial, as illustrated in Kuhn and Müller, 2010, where exponential shape functions were employed for the approximation of the phase field variable.

5.2.3 Irreversibility Constraint

Naturally, (5.64) allows for crack healing as it does not prevent the phase field to increase even after it has reached the value zero. Accordingly, one of the irreversibility constraints introduced in section 3.3.1 must be implemented. Due to its straightforward implementation and its robustness in terms of convergence, the method of the artificial Dirichlet boundary conditions (3.42) was used in this regard. Generally, this constraint requires to "freeze" the phase field variable at nodes that reached zero after a converged solution step. The technical condition is

$$\text{if } s_{I(k)} = 0 \quad \text{then } s_{I(k+1)} = 0, \quad (5.65)$$

which is realized from an algorithmic perspective by initializing the value of the phase field variable with zero, prior to every iteration, i.e. ${}_i s_{I(k+1)} = 0$, if the last converged solution revealed the value zero plus a given tolerance for this particular node. This is achieved by setting the component of the internal force vector corresponding to s_I to the negative value of the current iteration with

$${}_{(i-1)} \mathbf{P}_e = -{}_{(i-1)} s_{I_{t_{k+1}}} \quad (5.66)$$

By further setting the \mathbf{S}_{s_I, s_I} component of the system matrix to 1 and the rest of the entities of the corresponding column and row to 0, a subsequent iteration is forced to result in ${}_i s_I = 0$, according to (5.40). However, in order to preserve the iterative solution procedure for the remaining nodal degrees of freedom the contribution to the residual coming from the multiplication of s_I with the corresponding column of the system matrix must be conserved previously by

$${}_{(i-1)} \mathbf{P}_e = {}_{(i-1)} \mathbf{P}_e + \mathbf{S}_{:,s_I} \cdot {}_{(i-1)} s_{I(k+1)}. \quad (5.67)$$

and taken into account within the solution step of the current iteration.

Chapter 6

Simulation of Complex Fracture Problems

In this chapter, different numerical examples of complex cracking phenomena are outlined with regard to the simulation setup, the results, and the conclusions. The phase field models proposed in sections 4.1 and 4.2 address different characteristics of fracture. For the respective simulations the finite element formulations described in the previous section were implemented into the software FEAP (Finite Element Analysis Program, Taylor, 2014). This software is quite suitable as the complete source code is available. This allows for an implementation of new models on the element level using the basic infrastructure as e.g. calculation of shape functions, assembly, or solvers. The implementation of the phase field models is done via element routines and the incorporation of these subroutines into the executable. The program also provides methods for the generation of finite element meshes. As a convincing approximation of phase field cracks is associated with a certain degree of fineness in terms of discretization, it is often recommended to create meshes that are refined in regions of high significance regarding crack propagation. The meshing algorithm provided by FEAP may be labeled as rather basic as only regular meshes can be generated, and a transition to smaller elements does not yield an accurate saving in terms of the number of nodes. For this reason, meshes used for the simulations in this work were also generated by the meshing module of the commercial software Abaqus (Dassault Systemes, 2020), which allows for irregular elements, or alternatively via specially created meshing algorithms implemented in Python (Python Software Foundation, 2021). For the latter case an algorithm for quadrilateral refinement, proposed by Garimella, 2009 was utilized.

The discrete fields of the solutions for the simulation steps were saved as vtu-files, which subsequently were used for visualization by means of the open access tool Paraview (Kitware, 2016). Relevant secondary quantities like e.g. energies or crack characteristics were directly save by FEAP and processed or evaluated with Matlab (Mathworks, 2021). In addition, the number of free parameters is reduced by implementing the model in a non dimensional form similar as in e.g. Schlüter et al., 2014 or Kuhn et al., 2016. Thus, several values are given in relation to global length L and critical energy release rate \mathcal{G}_c . The dimensional values can be regained and are specified, whenever it is relevant to underline the accuracy of the models and compare them to measured data.

6.1 Verification of the Phase Field Model for Anisotropic Fracture Toughness

The examples presented and discussed in this section are presented to investigate the behavior of the phase field model for brittle fracture in materials with anisotropic fracture resistance. The implementation into an element routine involves the equations (5.27), (5.28) and (5.47)-(5.51).

The question of whether the crack patterns are plausible with regard to fracture mechanics is addressed. This issue is treated in the following simulations. Parts of these investigations were performed within a bachelor thesis (Etrich, 2020) supervised by the author of the present work.

6.1.1 Basic Effects of the Modification

Stationary crack fields

Prior to investigating any extensive simulation focusing on global crack evolution and deflection, the very principles of the model are investigated. In the focus is the question, how does the proposed weighting of the gradient incorporating a respective tensor (4.14) effect the character of the crack approximation. In order to characterize the resulting crack field, an analytic investigation was proposed in section 4.1 by means of a plane extrusion of the one dimensional solution. The simulation setup shown in Figure 6.1 was considered in order to verify whether this basic simplification is accurate and whether the crack energy is described correctly by (4.31) and (4.32). Accordingly, this two dimensional stationary problem was solved by finite elements, where the square domain includes an initial crack oriented parallel to the y -direction. The symmetry of the problem was used in order to minimize the computational effort. Accordingly, only a quarter of the domain (the area highlighted in green) was discretized. The analytical assessment is based on the assumption $\epsilon \rightarrow 0$, which demands a possibly small length scale parameter ϵ . This is further illustrated by the plot shown in Figure 4.7. A high mesh density is required for an accurate solution near the crack. Contrary, as no variation of the mechanical displacements is

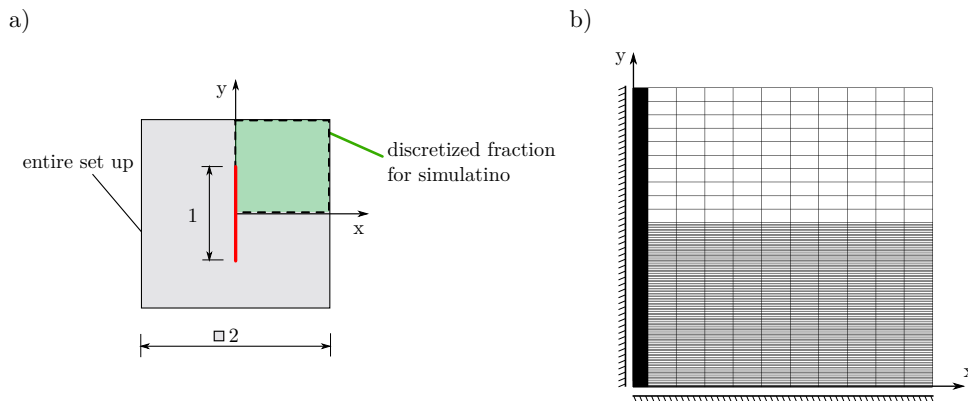


FIGURE 6.1: Setup of simulation of the stationary crack problem for the anisotropic phase fracture phase field model: a) load case b) finite element mesh for simulation.

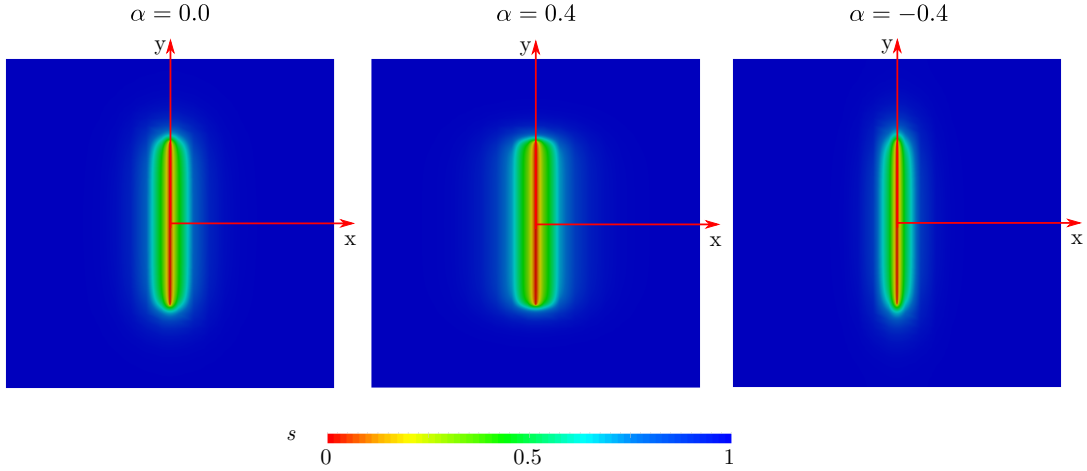


FIGURE 6.2: Contour plots of the phase field variable $s(\mathbf{x})$ determined by stationary simulations with different values of the anisotropy parameter α (results were mirrored with respect to the x and y axes for better presentation).

induced by a stationary crack a coarser discretization is accurate. Accordingly, the finite element mesh was locally refined, i.e. a decreasing element size as the elements get closer to the crack. The mesh shown in Figure 6.1b) consists of 12100 elements and 12544 nodes. In order to include a crack at all nodes with coordinates $x = 0$ and $y < 0.5$ the phase field was set to 0 as a boundary condition. Note that for this simulation the quantities $\eta, \beta, M, \lambda, \mu$ are irrelevant as the problem is load free and stationary. The critical energy release rate is only relevant if the energy consumed by the crack is to be determined. For all simulations within this section the orientation of the material anisotropy coincides with the $x - y$ -system and the anisotropy is therefore solely governed by the parameter α .

The three contour plots shown in Figure 6.2 result in a variation of α . The length scale parameter was set to $\epsilon = 0.01L$. The left plot is obtained for a simulation with $\alpha = 0$, which resembles the original isotropic formulation. In contrast the plot in the center illustrates the result for a simulation with $\alpha = 0.4$. One finds that for this case, the phase field crack gets wider in x -direction along with its entire vertical extent. This widening of the phase field crack is obviously driven by the multiplication of gradients in x -direction by $(1 + \alpha)$. Contrary, at the ends of the crack the transition zone becomes smaller, which is qualitatively consistent as gradients in y -direction are modified by $(1 - \alpha)$. The right plot shows the phase field for a simulation with $\alpha = -0.4$. The resulting phase field shape reveals the opposite behavior. Instead of widening the crack approximation in x -direction it is now narrowed in this case. This illustrates that, as expected according to the derivations in section 4.1, the width of the transition zone between the two phases is effected by the variation of α . The crack approximation of the simulation with $\alpha = -0.4$ can also be considered as a crack that has evolved in horizontal direction within a material described by $\alpha = 0.4$. Consequently, as the crack energy increases with a decrease of the overall contribution of $s < 1$ for this particular parameterization, a crack growing in horizontal direction in relation consumes less surface energy.

The evaluation shows that the model qualitatively behaves according to the investigations made in section 4.1.3. Whether the estimate of the surface energy in simulations with a finite regularization length is accurate, still needs to be investigated. Therefore, a stationary problem was solved repeatedly with variation of the parameter α . The results of 40 simulations are summarized in Figure 6.3. The plot compares the estimate for the crack energy (4.31) found by the extrapolation of the 1d solution with the energy approximations obtained by Gauss integration with the finite element procedure. Note the multiplication by 4 due to the reduced simulation domain. A relatively small length scale of $\epsilon = 0.005L$ was used for the underlying simulations, which is underlined by the reduction of the size of the transition zone, compared to Figure 6.2. The analytic and the numeric results match quite well, confirming the validity of the simplifications made in the analytic estimate.

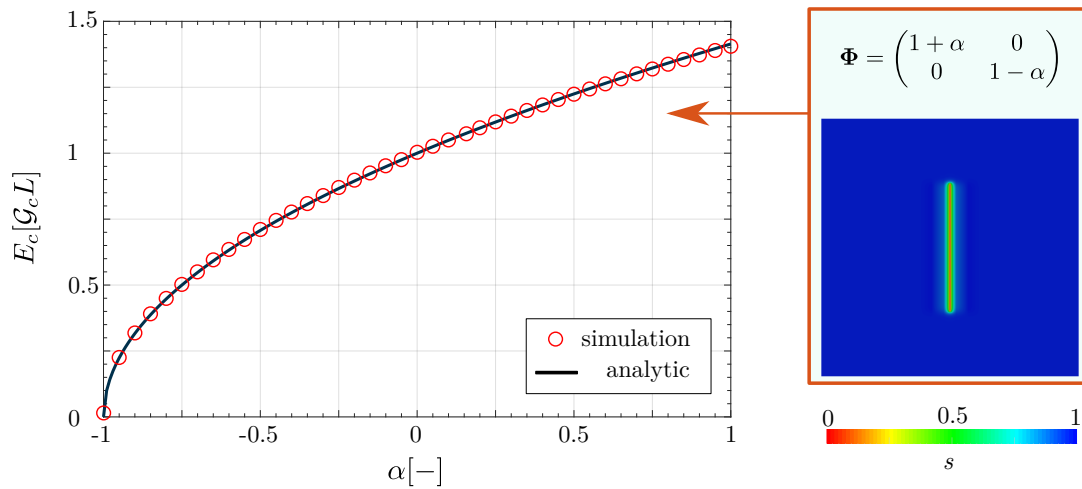


FIGURE 6.3: Evaluation of surface energy from stationary finite element simulations compared to the analytic estimate of anisotropic model.

Energy consumption in mode I cracking

The findings from the evaluation above are very interesting from a pure validation perspective, their benefit in terms of cracking behavior is so far not obvious. In order to illustrate the significance, an investigation of mode I crack growth is considered. For this purpose simulations were set up using the geometry of so called compact tension (CT) specimens (see Figure 6.4a). The background is the following: The directionality of the fracture toughness leads to a crack deflection independent of the load situation. Nevertheless, the stress distribution can be significant such that it becomes decisive and even if a material shows a fracture toughness anisotropy, a crack may not deviate from a straight path. Instead crack propagation will require a higher magnitude of the load. If the CT-specimen undergoes a mode I load, a significant concentration of the normal stress in vertical direction is induced at the tip of the notch. A variation of the strain energy required for crack initiation is expected for different parameterizations regarding anisotropy. In fact, this represents a possible fracture toughness anisotropy quantification (see e.g. Judt et al., 2015). In a simulation setup, the CT-specimen is fixed at the lower hole and a force load is applied at the upper hole of the specimen in order to induce a mode I load case. In every simulation the load was increased monotonically according to a linear function of

the time. It is indicated in Figure 6.4a) how cracks that initiate at the notch tip extended in horizontal direction. The objective is to compare the specific force required for crack

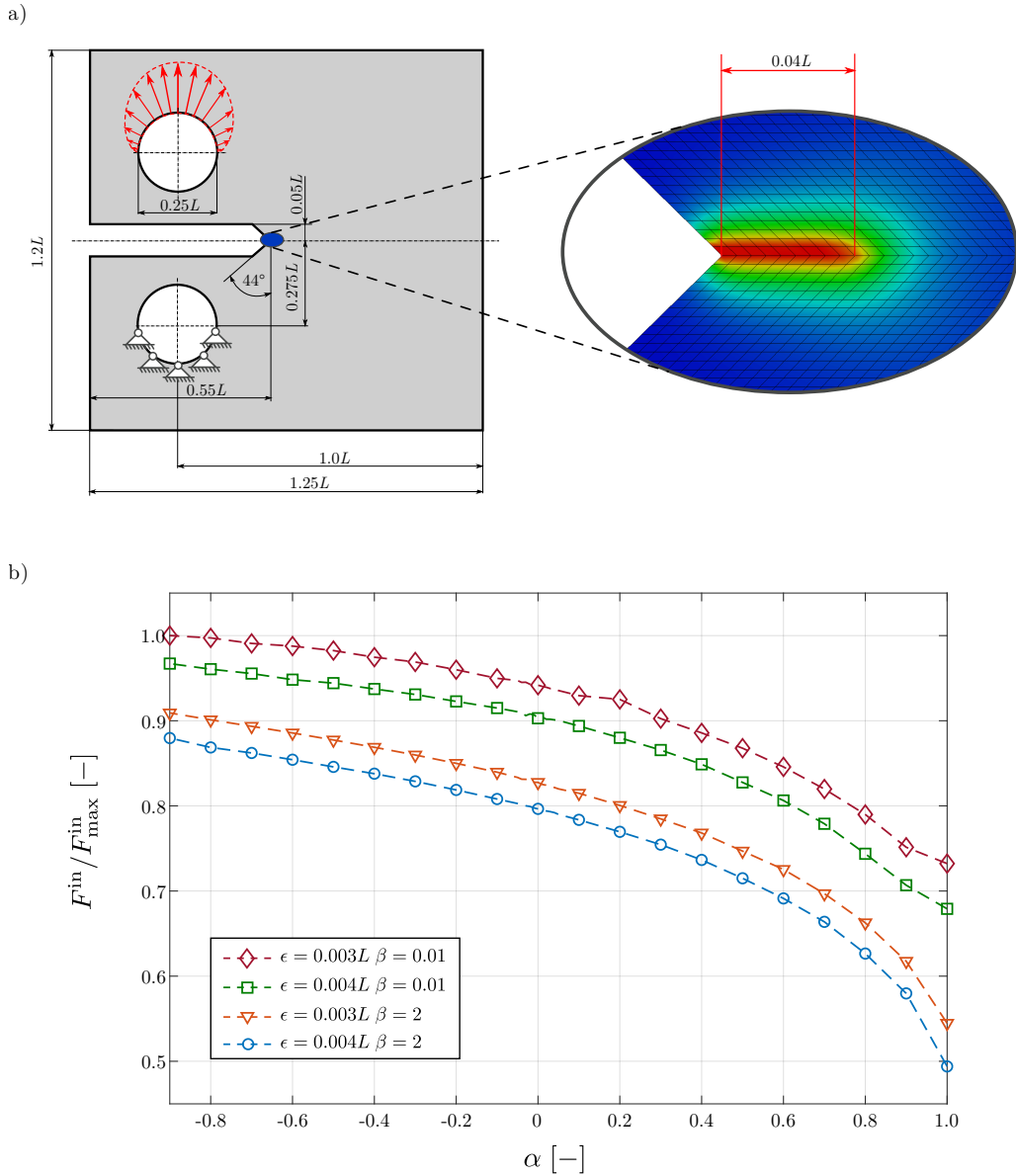


FIGURE 6.4: Illustration of phase field simulations with CT-specimen: a) simulation setup; b) applied force for crack initiation versus corresponding value α obtained from different simulations.

initiation. The process of crack initiation occurs rather rapidly in force control mode and hence the determination of the exact tensile force related to crack initiation is difficult. Therefore, the crack initiation force is defined as the average force associated with the first decrease of the phase field to $s = 0$ for 10 nodes in horizontal direction, representing a length of $0.04L$.

Simulations were run with different parameter sets given in Table 6.1. The results of the complete investigation are summarized in Figure 6.4b), where the normalized tensile

TABLE 6.1: Parameter sets for phase field simulations with the CT-specimen outlined in Figure 6.4.

parameter	set 1	set 2	set 3	set 4
length scale ϵ	$0.003L$	$0.003L$	$0.004L$	$0.004L$
degradation function parameter β	2.0	0.01	2.0	0.01
residual stiffness parameter η			10^{-6}	
Poisson's ratio ν			0.25	
mobility M			$10 \frac{L}{g_c T}$	

crack initiation force of the simulations is plotted versus the anisotropy parameter α . Obviously, the data points of corresponding parameter sets lie on monotonous curves. For all parameter sets the required force decreases with an increasing value of α . The reason for this behavior can be verified in energetic terms. The cracks are generally driven to propagate in horizontal direction, which is prescribed to consumes more energy for negative values for α . The comparatively costly surface potential allows for more strain energy. This is in agreement with the results of stationary simulations from above. The curves from the crack initiation simulations reveal a similar characteristic as found in the energy evaluation in Figure 6.3. Note in that regard, that the evaluation of the surface energy depicted in Figure 6.3 is done for a vertical extent of a crack. Furthermore, an overall decrease of the initiation force is found for the parameterization of set 1 and set 3, which is consistent with the lower critical stress-stain states of (3.39) for the quadratic degradation function implemented by $\beta = 2$. The load for crack initiation also decreases with increasing values of the length scale ϵ since larger values consume more energy.

6.1.2 Assessment of Crack Deflection

As defined in section 4.1 the resistance tensor Φ is quantified by the parameters α and θ . Its effect on potential cracking directions is studied. Numerical examples for three different simulation setups are presented and discussed in order to illustrate the capabilities of the proposed anisotropic phase field model regarding the influence on the crack path. The model behavior is in the focus to provide a comprehensive understanding of the proposed phase field model. A verification in terms of comparing simulation results to experimental observations is outlined within the subsequent section.

Plate with sharp notch

The effects of a certain parameterization on the results obtained from the phase field simulations will be illustrated by a plate with a sharp notch, see Figure (6.5). The plate is subject to a tensile load introduced by a prescribed displacement at the top edge of the specimen. Since the plate is fixed at the lower edge the stress state introduced within the plate is mainly characterized by normal stresses in the vertical direction, where stress concentration occurs at the tip of the notch. This classic mode I load situation drives a crack purely horizontal under the assumption of an isotropic material, which is indicated by the solid red line in Figure 6.5. The specimen was discretized by means of 14899 nodes, which led to a number of 14406 elements (mesh depicted in Figure 6.6). No local mesh refinement was introduced so the element edge length was constant for the entire domain. The displacement $\mathbf{u}(t)$ was implemented within the simulation by linear monotonously

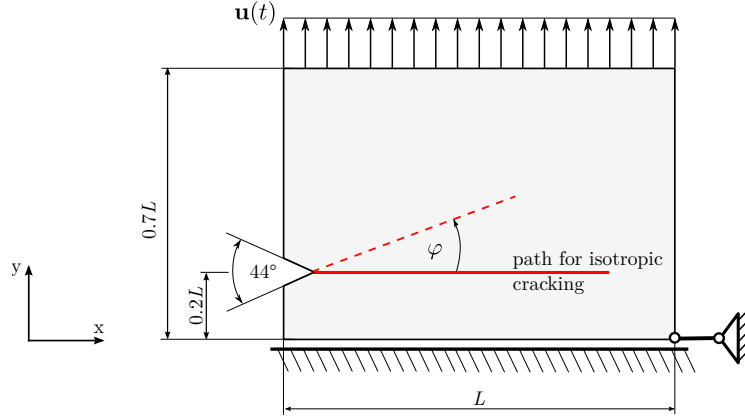


FIGURE 6.5: Setup for phase field simulation of notched plate under tensile load with indication of deflection angle definition.

increasing function. For all simulations the parameter set given in Table 6.1 was used except for the regularization length with $\epsilon = 0.015$ and the degradation function parameter was set to $\beta = 2$.

The results of several simulations are shown in Figure 6.6 by means of contour plots of the phase field variable s . The plot at the top right represents the isotropic case with $\alpha = \theta = 0$. As expected a crack initiates at the notch tip and propagates in the horizontal direction. In contrast, if the anisotropy parameters are altered, even for the identical stress state, one obtains crack paths, that deviate from this orientation and reveal a certain deflection angle φ as schematically indicated in Figure 6.5. Comparing the simulations regarding the deflection angle found in these contour plots the particular effects become clear. If for example a small material rotation is implemented by setting the parameter $\theta = 17^\circ$ and $\alpha = 5 \times 10^{-4}$, the resulting crack path reveals an initial deflection angle of $\varphi \approx 3^\circ$. This deflection angle can be increased by two different options. One may either increase the rotation of the material to e.g. $\theta = 34^\circ$ with a constant value of α or increase the intensity of $\alpha = 0.001$ with constant material orientation. The results in Figure 6.6 show that this yields a deflection angle of approximately 5.5° and 10° , respectively. The behavior is consistent with expectations regarding the orientation and intensity of the anisotropy of the fracture resistance. Several cases of parameterizations are evaluated regarding the evolution of the strain energy. The respective plot is shown in Figure 6.6. The plot on the right depicts the entire duration of the simulations. As the curves lie very close to one another, the decisive part is magnified on the right. All curves reveal an increasing trend until crack initiation. This causes a release of strain energy and leads to a turning point of the curves. The energy decreases during crack growth when the crack propagates from left to right. Considering the plot on the right a difference in the load applied of crack initiation and growth is clearly visible. Interestingly, if the two curves for the parameter set with $\theta = 34^\circ$ are compared it is found that a lower driving force is needed for the crack growing under a higher deflection angle (see Figure 6.6 third row). However, this can be explained by the observations from the previous section, where it was shown that increasing the intensity parameter α results in a widening of the crack approximation along the x -direction and a contraction in the y -direction. Regarding the transformation Φ , this leads to a thinner approximation of the cracks in this particular

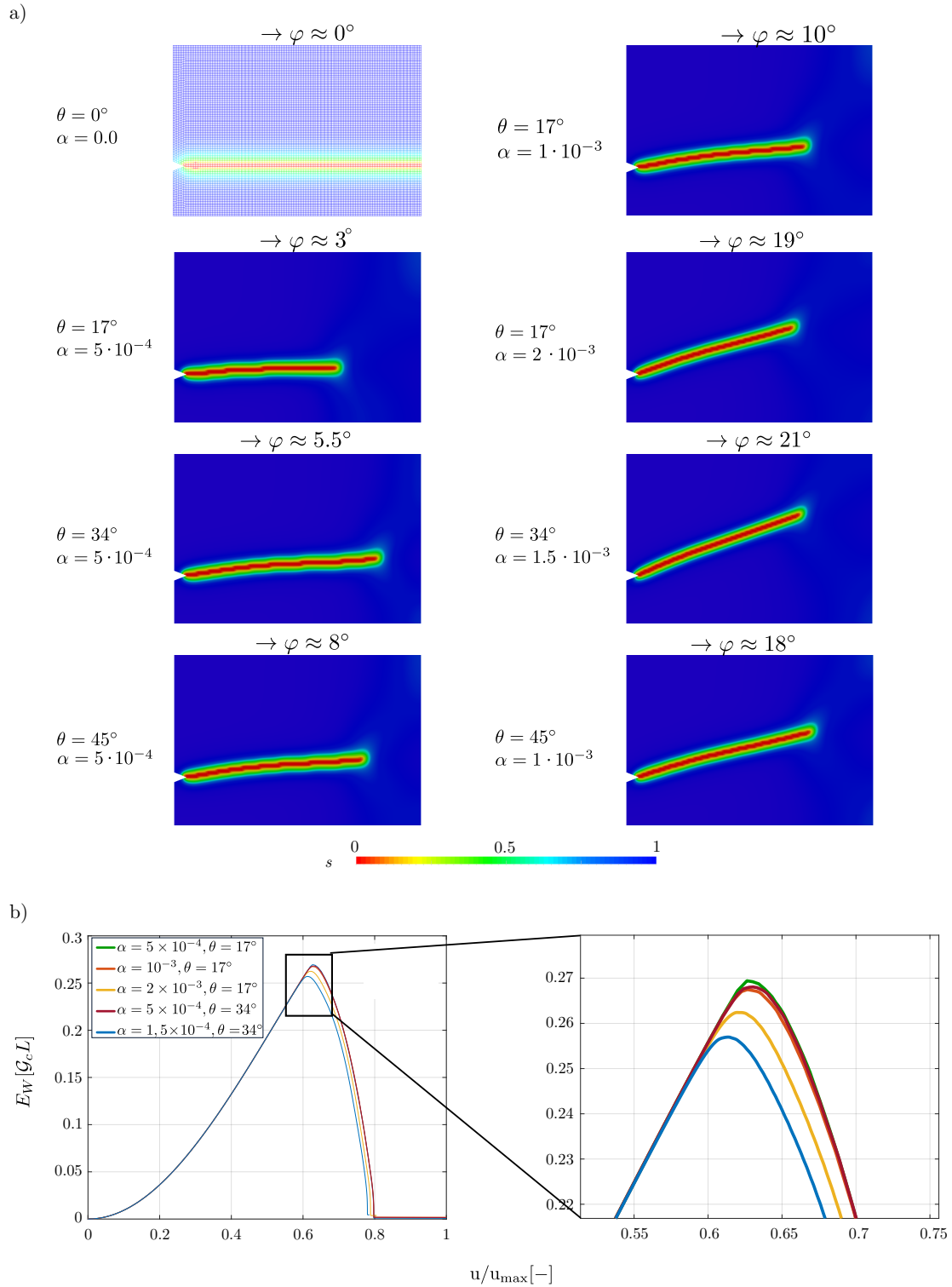


FIGURE 6.6: Comparison of results from simulations with notched plate specimen: a) contour plots indicating the phase field obtained by different sets of parameters α and θ , b) plot of strain energy versus displacement evaluated for several simulations.

example. In summary, the results obtained from the present example illustrate, that the crack path predicted by the model is consistently governed by the parameters.

Three point bending

The 3 point bending test is widely used for investigations of fracture. The respective setup is schematically illustrated in Figure 6.7. A mode I load case is created. Nonetheless, it is different from the perspective of phase field modeling. The setup is related to the bending of a Bernoulli beam. At the section with the highest bending moment the stress field obtains a maximum in tension as well as in compression at opposite sides. For the 3 point bending case of the present example, this results in a concentration of compression stresses occurring in the region where the load is applied. This is a classic example, where a distinction between compression and tension must be taken into account. Without pressure tension distinction this would cause a decrease of the phase field within this region rendering an unphysical behavior. The specimen was discretized using 11631 nodes and 11460 quadrilateral elements. The used finite element mesh was refined in the center area to enable a good approximation of possible cracks and also to keep computing times low. The mesh is indicated at the top of Figure 6.7. The parameter set given in Table 6.1 was used for all simulations with a regularization length of $\epsilon = 0.004L$ and $\beta = 0.01$.

The relevant parameters quantifying the directionality of the fracture resistance namely intensity α and orientation θ were varied over a broad range of parameter combinations. Values for α in a range of $0 \geq \alpha \geq -0.5$ with steps of 0.1 are combined with values for θ in the range of $-90^\circ \geq \theta \geq 90^\circ$ with steps of 15° . Furthermore, the horizontal distance e describing the position of the load application was varied to get three slightly different setups regarding the stress field. Accordingly, a total of 156 simulations were performed. In order to illustrate the model's response, exemplary results are depicted in Figure 6.8. The contour plot on the top of this figure shows the results for the standard case of an isotropic material. As expected the crack initiated at the root of the notch and propagates in vertical direction without deflecting from this path. Due to compressive strains no cracking occurs at the top region of the specimen, which is ensured by the energy split according to Amor et al., 2009. This behavior was found within experiments for isotropic brittle materials. Also in different studies of alternative phase field approaches for fracture as e.g. Aldakheel et al., 2018b or Ambati et al., 2015 this crack path was obtained. The plot below this basic

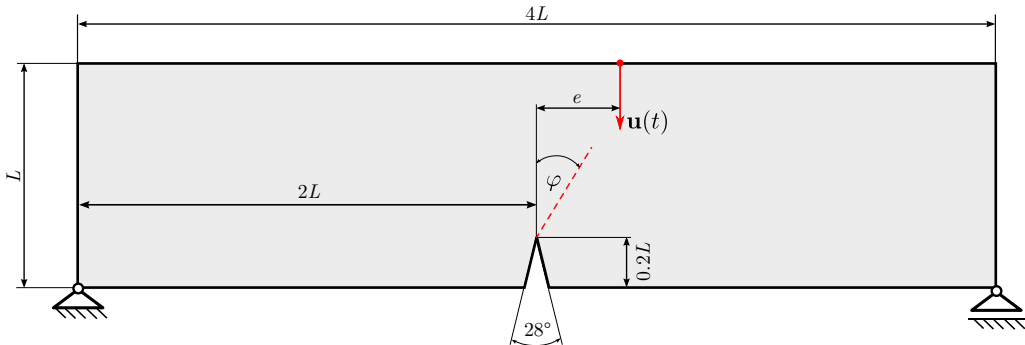


FIGURE 6.7: Setup for phase field simulation of 3 point bending tests with various bending moments.

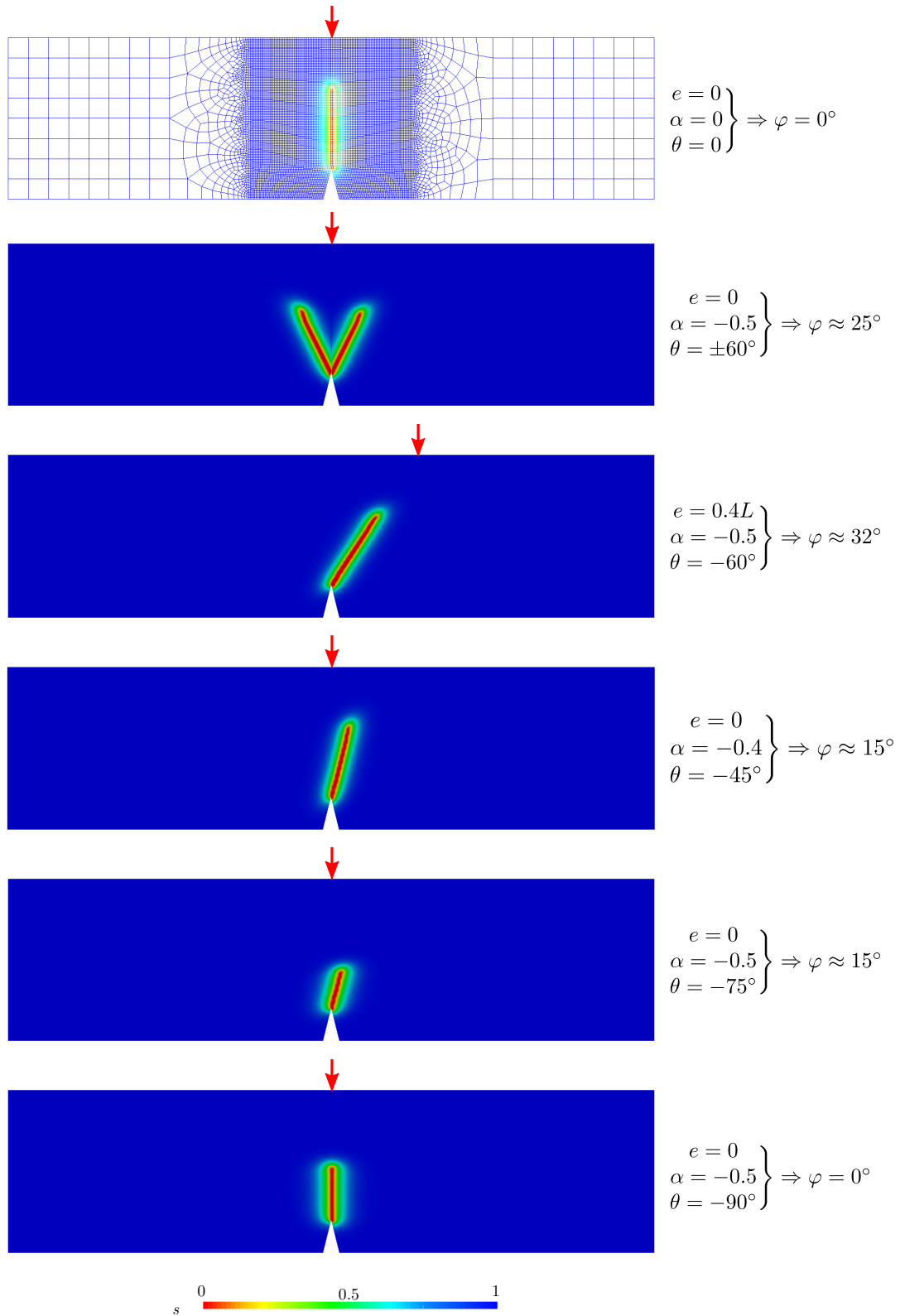


FIGURE 6.8: Comparison of crack paths obtained by selected simulations of the 3 point bending specimen with different sets of parameters α and θ .

case shows the results for orientations $\theta = \pm 60^\circ$ placed on top of each other. For both, the positive and the negative orientation the intensity parameter α was set to $\alpha = -0.5$. As expected within these simulations, the crack deflects from the pure vertical direction and propagates towards the top edge under a deflection angle with equal absolute value and an orientation in agreement with the material orientation. Considering the simple model structure, these results are impressive since the crack is driven to deflect even in presence of a stress field clearly favoring vertical cracking. That the load distribution still influences the cracking behavior is illustrated by the simulation with equal material parameters but under a different bending moment induced via the offset of the load introduction with $e = 0.4L$. For this case, an even higher deflection angle of $\varphi \approx 32^\circ$ is obtained, as with the higher value for e the stress peak is shifted to the right. Once more, the relevance of both parameters is proven since the magnitude of the deflection angle is controlled by α or θ independently.

The consistency of the model behavior in terms of parameter variation becomes even more apparent when considering a comparison of all the performed simulations by means of the scatter plots depicted in Figure 6.9. These plots visualize the obtained deflection angle for all performed simulations of the three point bending specimen, where each of the three plots represents a particular setting of the measure e . The grid lines indicate the anisotropic model parameters. The size of the circle represents the deflection angle. A vertical crack is indicated by a vanishing area. In order to enable a quantitative extraction of the deflection angle coloring is added. As the first observation from this evaluation one finds the deflection angle to increase with an increasing absolute value of the intensity, within the considered range. Further, the relevance of the load case becomes apparent. For the centric load the distribution of the deflection angle happens to be symmetric in terms of the circle area certifying the model consistency. In contrast the distribution becomes asymmetric with increasing value for e , clearly illustrating the tendency of the crack to favor the side with the maximum bending moment. In fact, $e = 0.4L$ reveals an almost suppressing crack deflection to the other direction. Interestingly, in contrast to the intensity, all three plots show that the magnitude of the crack deflection angle is in any case limited with a maximum within $-75^\circ \leq \theta \leq -60^\circ$. This is representatively shown by the two contour plots at the bottom of Figure 6.9. This behavior is in agreement with the modeling framework as the energetic evaluation provided in Figure 6.10 confirms. The line plot in Figure 6.10a) shows the different contributions to the total energy under increasing load, for the case $\alpha = -5$, $\theta = -30^\circ$. The turning point of the strain energy indicates crack initiation as simultaneously the crack energy shows an increase. This state is compared for all θ in Figure 6.10b), which proofs that with an increasing value of θ the complete set of energies at the point of crack initiation and the corresponding load increases. This shows, that cracking, even under decreasing deflection angles, still consumes more energy with increasing orientation θ . The explanation for this behavior is that the rotation of the potential transition zone $0 \leq s < 1$ indicating cracks may be larger for certain orientations. This becomes apparent by comparing the width of the transition zone e.g. for the three last examples of Figure 6.8. In fact, $\theta = 90^\circ$ is equivalent to $\theta = 0$ with a change of the sign of α , which was studied in section 6.1.1. Accordingly, from the energetic perspective the prediction is correct and to force higher deflection angles the intensity parameter would have to be adjusted. However, even in realistic settings, certain anisotropies were found to lead to so called forbidden directions as shown in Roman et al., 2013.

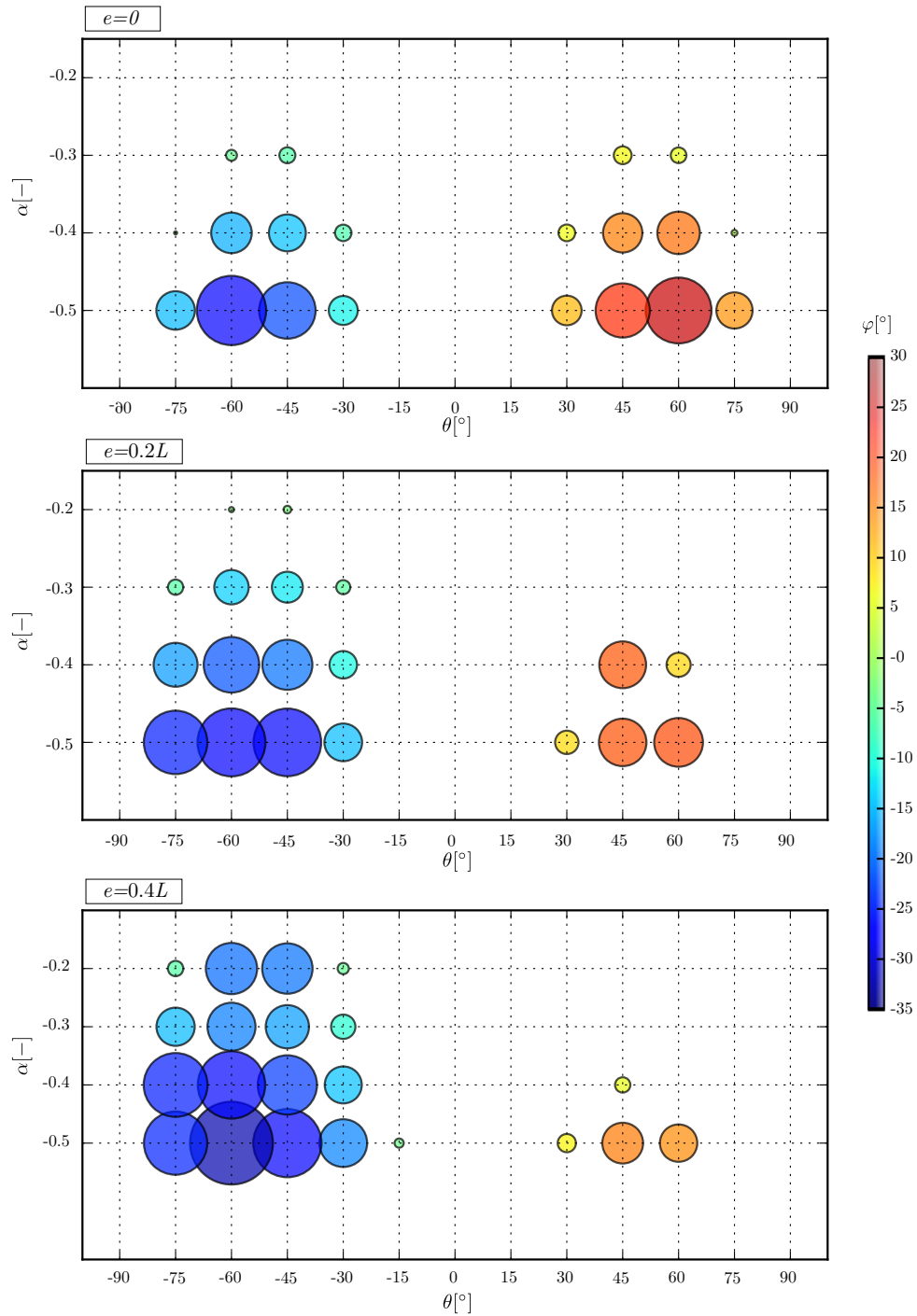


FIGURE 6.9: Comparison of deflection crack deflection angle φ in scatter plot for all simulated parameter combinations α and θ of the 3 point bending specimen.

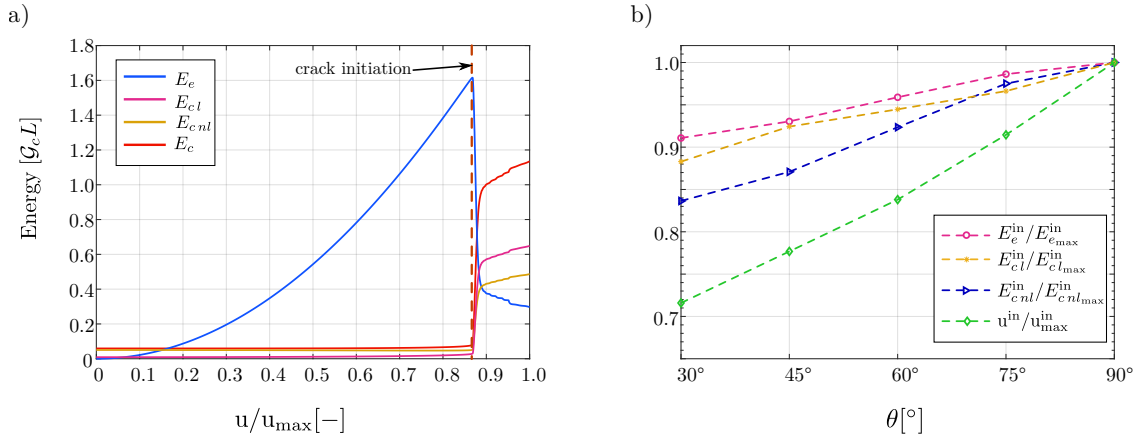


FIGURE 6.10: Energetic evaluation of the simulations with the 3 point bending test for $\alpha = -0.5$: a) evolution of different energy components for $\theta = -30^\circ$, b) normalized quantities versus material orientation.

6.1.3 Validation by Experimental Results

For a more realistic verification of the anisotropic phase field model a comparison with experimental results as well as an alternative crack prediction technique is conducted. In detail, the phase field model is applied to test cases inspired by experimental investigations done in a study by Judt et al., 2015. In the focus of this study are holed aluminum plates of different geometry. The raw material used for the specimens was rolled and the directionality of the fracture toughness was confirmed by measurements of the fracture toughness along with orthogonal directions. The intensity of the anisotropy was quantified by the ratio

$$\chi = \frac{K_{Ic}^{\text{TD}}}{K_{Ic}^{\text{RD}}}, \quad (6.1)$$

where the superscripts TD and RD represent rolling direction and traverse direction, respectively. Isotropic materials are accordingly specified by $\chi = 1$. $\chi < 1$ as well as $\chi > 1$ describe fracture toughness anisotropies with a preference of one or the other direction. The setup provides a well defined framework for the validation of the presented phase field model. The specimen geometries are given in Figure 6.11. The finite element mesh is depicted next to the geometries. In order to provide a comparison of the crack path predictions of the phase field model with those from Judt et al., 2015 requires an exact match of the prediction of the isotropic case ($\alpha = 0$). Relevant model parameters were therefore adjusted until a match of the relevant crack patterns was obtained. The regularization parameter ϵ may generally be chosen as small as possible in order to get the correct solution. Accordingly, the finite element mesh must be very fine at regions where crack evolution is expected.

Remarks on tension compression distinction

As previously outlined, the split of strain energies into tension and pressure contributions is crucial. However, it may not be decisive in every example as e.g. pure tensile testing of a smooth specimen. No compressive stresses are found in this case and usage of energy

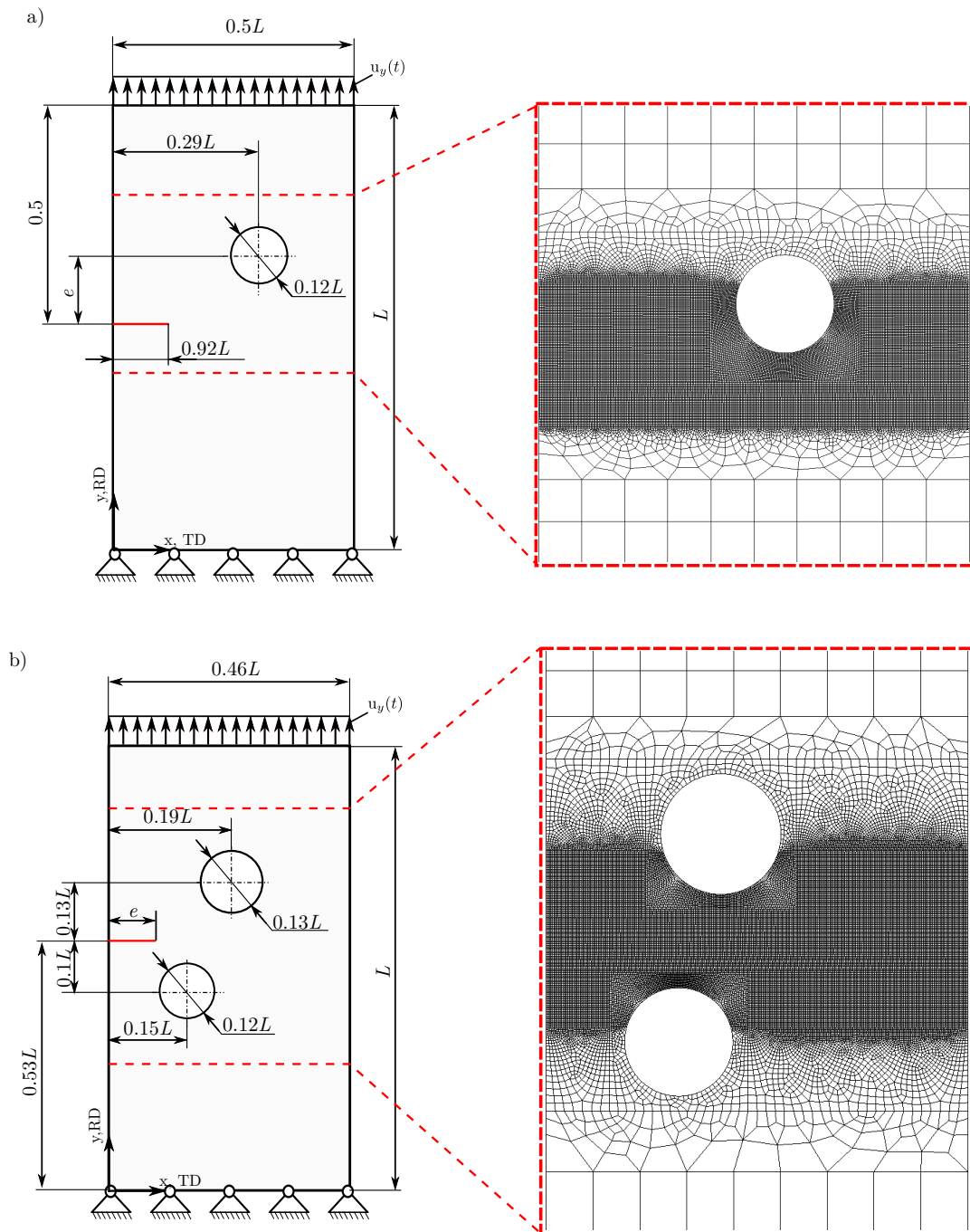


FIGURE 6.11: Setup for anisotropic phase field simulations with holed plates with indication of crack paths for the isotropic case: a) geometry 1, b) geometry 2.

decomposition is irrelevant and can be neglected in order to save computational costs. In the present case of the holed specimens compressive stresses are indeed present in the vicinity of the twelve o'clock and the six o'clock position of the holes. With view on the computational effort of a single simulation and the number of different simulations necessary, the question is whether these compressive stresses are relevant for the crack path. In order to address this question, phase field simulations with and without implementation of the volumetric deviatoric split by Amor et al., 2009 were conducted for the specimen geometry 1. The corresponding crack patterns are shown in Figure 6.12. The contour plots of Figure 6.12a) show the crack path, which resulted from a simulation without tension compression distinction. The crack grows in horizontal direction before it bends and further grows towards the hole. Almost at the same time as the crack reaches the edge of the hole, a second crack initiates at the right side of the hole and grows in horizontal direction. Obviously, this prediction deviates from the correct crack path (see Figure 6.13). In contrast, if tension compression distinction is taken into account the crack bends for a significantly lower angle as depicted in Figure 6.12b). Accordingly, handling of compressive stresses does indeed effect the crack path for this test setup, but although it is taken into account the prediction still fails as again a second crack initiates at the right side of the hole. Both of these simulations were performed with the quadratic degradation function rendered by $\beta = 2$, which predicts crack nucleation for comparatively low stress-strain states (see section 3.3.1). This is the reason for the unphysically predicted cracking at the right side of the hole. As shown by Figure 6.12c), the correct crack pattern is obtained from a simulation with tension compression distinction and setting $\beta = 10^{-3}$. Interestingly, a similar crack path is predicted if the distinction of tensile and compressive stresses is neglected and instead the value for beta is even further decreased to $\beta = 10^{-4}$. In summary, it can be stated that for the present examples the compressive stresses effect the crack path in general so it may be meaningful to use compression tension distinction. However, as illustrated by the simulation results Figure 6.12c) the effect is small and can be handled by simply decreasing the value of the degradation function β . As simulations with tension compression distinction show a less efficient behavior in terms of convergence and consume much more time, no tension compression distinction was used within the following simulations.

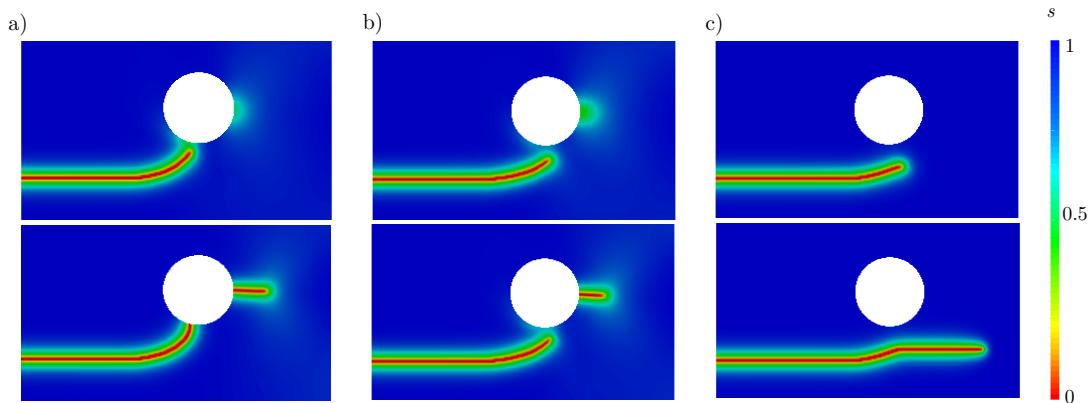


FIGURE 6.12: Comparison of results from simulations of geometry 1 with and without tension compression differentiation with $\alpha = \theta = 0$: a) no split $\beta = 2$, b) split $\beta = 2$, c) split $\beta = 0.001$ and no split $\beta = 0.0001$.

Specimen geometry 1

As depicted in Figure 6.11a) the mesh for specimen geometry 1 was locally refined within the relevant area, where cracking was expected. The generated mesh consists of 34261 nodal points and 34019 elements. The elastic constants were adjusted to mimic the material employed in Judt et al., 2015 (Young's modulus = 72 MPa, $\nu = 0.3$). The phase field parameters for all presented results of this specimen were $\epsilon = 0.004L$ and $\beta = 10^{-4}$. The anisotropy measure χ is referred to as the axis system indicated in Figure 6.11, which sets $\theta = 0$ for all simulations to be compared. The anisotropy values investigated were in a range $\chi \geq 1$, which is in agreement with (6.1) and the axis system indicated in Figure 6.11. Thus cracks are prone to grow in vertical direction rather than in horizontal direction. In order to implement this specific preference into the proposed phase field model, values for alpha must be varied for $\alpha \leq 0$. Simulations with different values of alpha were run, where a monotonously increasing displacement in positive y -direction was applied at all nodes of the top edge, while nodes of the bottom edge were locked. The results of these simulations are illustrated in Figure 6.13 cracks that have extended almost over the specimen width. For comparison, the crack paths proposed in Judt et al., 2015 are depicted at the bottom right of this figure. With respect to these crack paths the results provided by the anisotropic phase field model generally reveal good agreement. The modeling of increasing intensity of the directionality by decreasing the values for α in the first place shifts the crack path consistently closer to the hole. In fact a significant third reversal of the crack path, which closely matches the reference, can be detected for $\alpha = -0.029$. It is worth noting the very small magnitude of α in relation to the significant change of the crack path, which confirms high sensitivity. The simulation with $\alpha = -0.039$ finally results in a crack path that enters the hole at about five o'clock, again in good agreement with the reference.

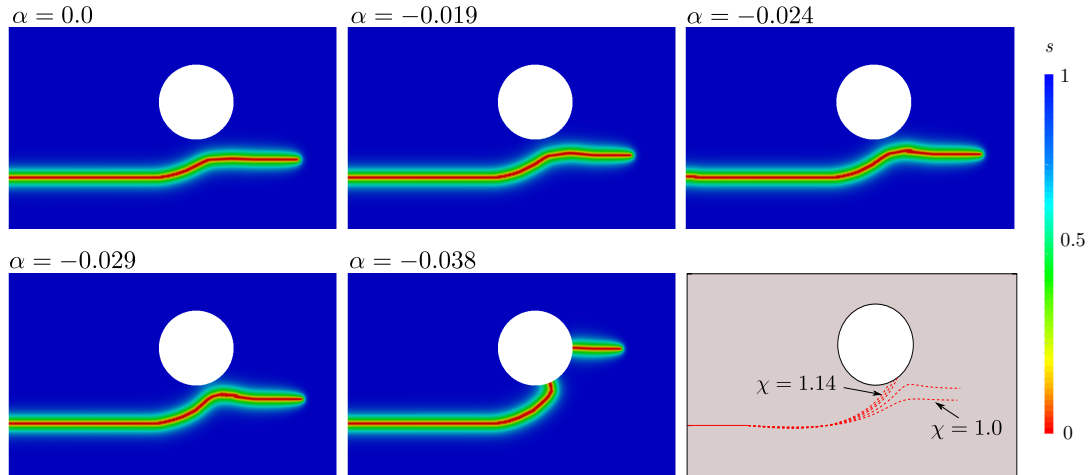


FIGURE 6.13: Comparison of simulation results from the phase field model for different values of α with the reference solution (bottom right).

Specimen geometry 2

The specimen depicted in Figure 6.11b) was discretized by 35066 nodes forming 34724 elements. The same material parameters as for geometry 1 were used. The best fit of the crack path for $\alpha = 0$ was again obtained for a regularization length of $\epsilon = 0.004L$ and

the degradation function was set to $\beta = 10^{-4}$. The crack paths obtained from phase field simulations with different intensities of the directionality are summarized in Figure 6.14. For the isotropic case, the crack starts to grow in horizontal direction and first deflects towards the upper hole after passing the 12 o'clock position of the lower hole. It curves again after a short period of propagation and then continues to grow in horizontal direction. For slight anisotropies the crack deflects towards the lower hole first for a short period before turning towards the upper hole, as the plots for $\alpha = -0.015$ and $\alpha = -0.025$ show. Note, the crack approaches the lower hole closely for $\alpha = -0.025$. The result of the simulation with $\alpha = -0.038$ shows that as expected the crack grows towards the lower hole and finally breaks through its edge before a new crack initiates at the right side of the lower hole. The presented results match the results proposed in Judt et al., 2015 quite well, even with some limitations. In fact no significant deflection towards the lower hole is visible for the isotropic case, which presumably would require an even finer discretization. However, the general trend of the effect on the change of the particular crack patterns with respect to α could consistently be reproduced, which again confirms the practical character of the proposed anisotropic phase field model.

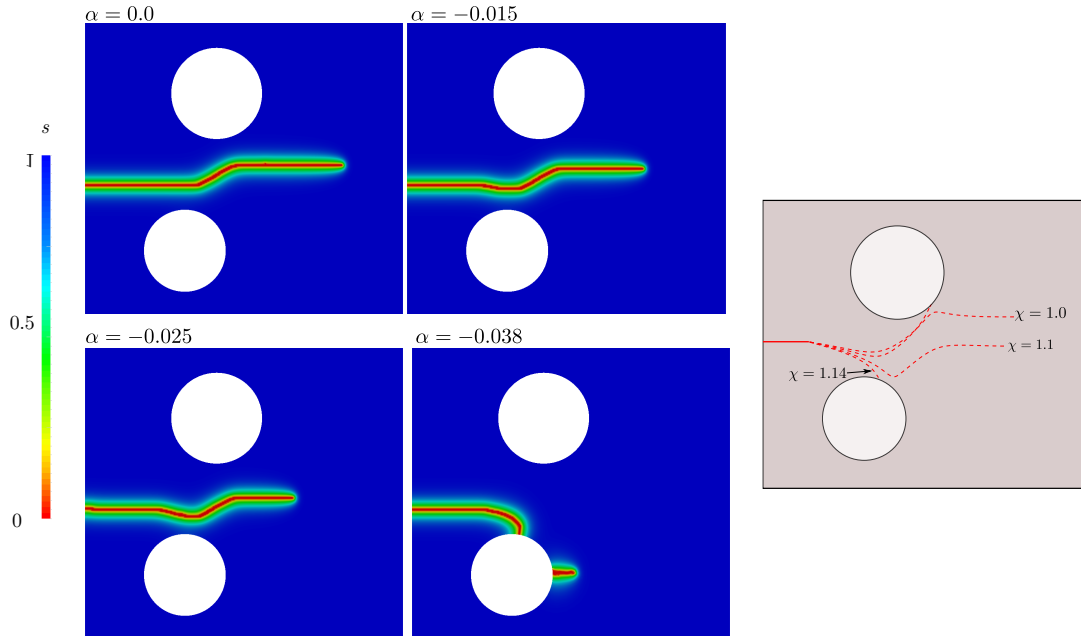


FIGURE 6.14: Comparison of simulation results from the phase field model for different values of α with the reference solution (right).

6.2 Verification of the Phase Field Model for Fatigue Crack Growth

The numerical examples of this section are presented in order to investigate, characterize and also to verify the phase field model for fatigue crack growth defined by the free energy functional (4.67). At first, the focus is on the driving force mechanism of this formulation to illustrate the meaning of the parameters. Subsequently, the model characteristics will be investigated in terms of crack growth rates for various load ratios. The respective Paris

curves provide a criterion to assess whether realistic material behavior can be mimicked by the phase field model. For these evaluations solely mode-I load cases are set up. However, the second very crucial property to be investigated is whether the correct crack path is predicted by the phase field model. This will be treated using several illustrative simulations of representative mixed mode load cases.

6.2.1 Characterization of Fatigue Crack Growth Behavior

The simulations outlined in the following were performed with the CT-specimen according to the ASTM, 2009 standard. This specimen type is very widespread and often used when it comes to the characterization of fracture relevant material constants. In order to investigate fatigue crack growth rates for different sorts of materials, it was used within e.g. Ritchie, 1977; Uematsu et al., 2020; Chen et al., 2013 or Gook, 1993, to list just a few publications. Also within several numerical studies of fatigue cracking this geometry was utilized as in e.g. Fish and Yu, 2002; Flouriot et al., 2003.

The definition of the geometry of this specimen is depicted in Figure 6.15a). The discretization of the CT-specimen, which was used for the cyclic simulations is shown in Figure 6.15b). The cracks are expected to grow purely horizontal under a mode I type loading. Accordingly, the mesh was refined in small narrow rectangular area across the complete specimen width. The used mesh consists of only 3650 nodes and 2984 elements. Consider the comparatively high number of load cycles necessary for realistic setups, computation times are rather long even if the cycle jump procedure is applied. Also the current crack length is of significant importance as it is e.g. used to determine the growth rate. The contour plot in Figure 6.15a) reveals how the crack length is defined according to the respective ASTM, 2009 standard. The effective crack length is the horizontal distance from the center of the holes to the crack tip. For the present phase field framework the location of the crack tip is defined by the node coordinates of the node with $s = 0$ at the maximum x -coordinate. The effective crack length is supposed to enter the formula for the

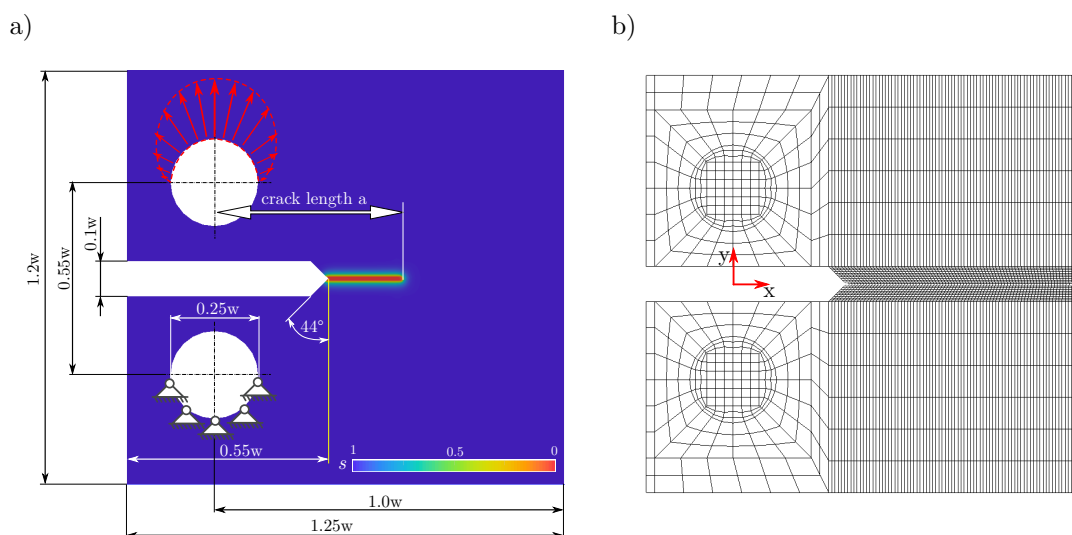


FIGURE 6.15: Illustration of used setup for simulations with CT-specimen:
a) indication of effective crack length b) finite element mesh.

respective cyclic ΔK range

$$\Delta K = \frac{\Delta F}{B\sqrt{L}} f\left(\frac{a}{L}\right), \quad (6.2)$$

with

$$f\left(\frac{a}{L}\right) = \frac{\left(2 + \frac{a}{L}\right) \left[0.886 + 4.64 \left(\frac{a}{L}\right)^2 - 13.32 \left(\frac{a}{L}\right)^3 + 14.72 \left(\frac{a}{L}\right)^4 - 5.69 \left(\frac{a}{L}\right)^5\right]}{\left(1 - \frac{a}{L}\right)^{3/2}}. \quad (6.3)$$

This formula is an approximation obtained from a variety of linear elastic finite element simulations and was confirmed in e.g. Srawley, 1976. The effective crack length is represented by a , the specimen thickness is B and ΔF represents the force range applied through the vertical loading of the bolt holes. As illustrated in Figure 6.15a) this load was implemented as a distributed sinusoidal surface load in order to approximate the load transmission by the upper bolt. The surface load was adequately distributed to the nodes located on the upper semicircle of the bolt hole. For the presented finite element discretization the effective crack length is not available in a continuous form. Hence it is substituted by the discrete form a_p , where $p = 1 \dots n_d$ and n_d represents the respective number of data points associated with the effective crack length. Accordingly, (6.2) is evaluated using $f\left(\frac{a_p}{L}\right)$.

As illustrated in the section 4.2 the driving force mechanism is different for the phase field model for fatigue crack growth and for the static model. The fatigue related driving mechanism is illustrated by the following numerical example. The initial state of the phase field variable was set to one over the entire domain, so the specimen can be referred to as not pre-cracked. A cyclic phase field simulation was set up with constant amplitude loading of pulsating kind ($R = 0$). This pulsating load is approximated by a ramp function as schematically illustrated in Figure 4.13. The parameters relevant for this cyclic simulation are given Table 6.2. For both degradation functions the quadratic function (3.36) was utilized, i.e. $h(s) = g(s) = s^2$. The simulation resulted in a decrease of the phase field right at the tip of the notch of the CT-specimen indicating crack initiation. A detailed

TABLE 6.2: Parameter set used for cyclic phase field simulations with the CT-specimen outlined in Figure 6.16.

length scale ϵ	0.01L
degradation function parameter β	2.0
residual stiffness parameter η	10^{-6}
Young's modulus E	$2.1 \cdot 10^5$ MPa
Poisson's ratio ν	0.25
critical energy release rate \mathcal{G}_c	$2.33 \cdot 10^3$ J/m ²
threshold stress A_D	200 MPa
knee point cycle number n^D	10^6
lifetime exponent k	5
mobility \hat{M}	$10 \frac{L}{\mathcal{G}_c \Delta N}$
cycle increment ΔN	15

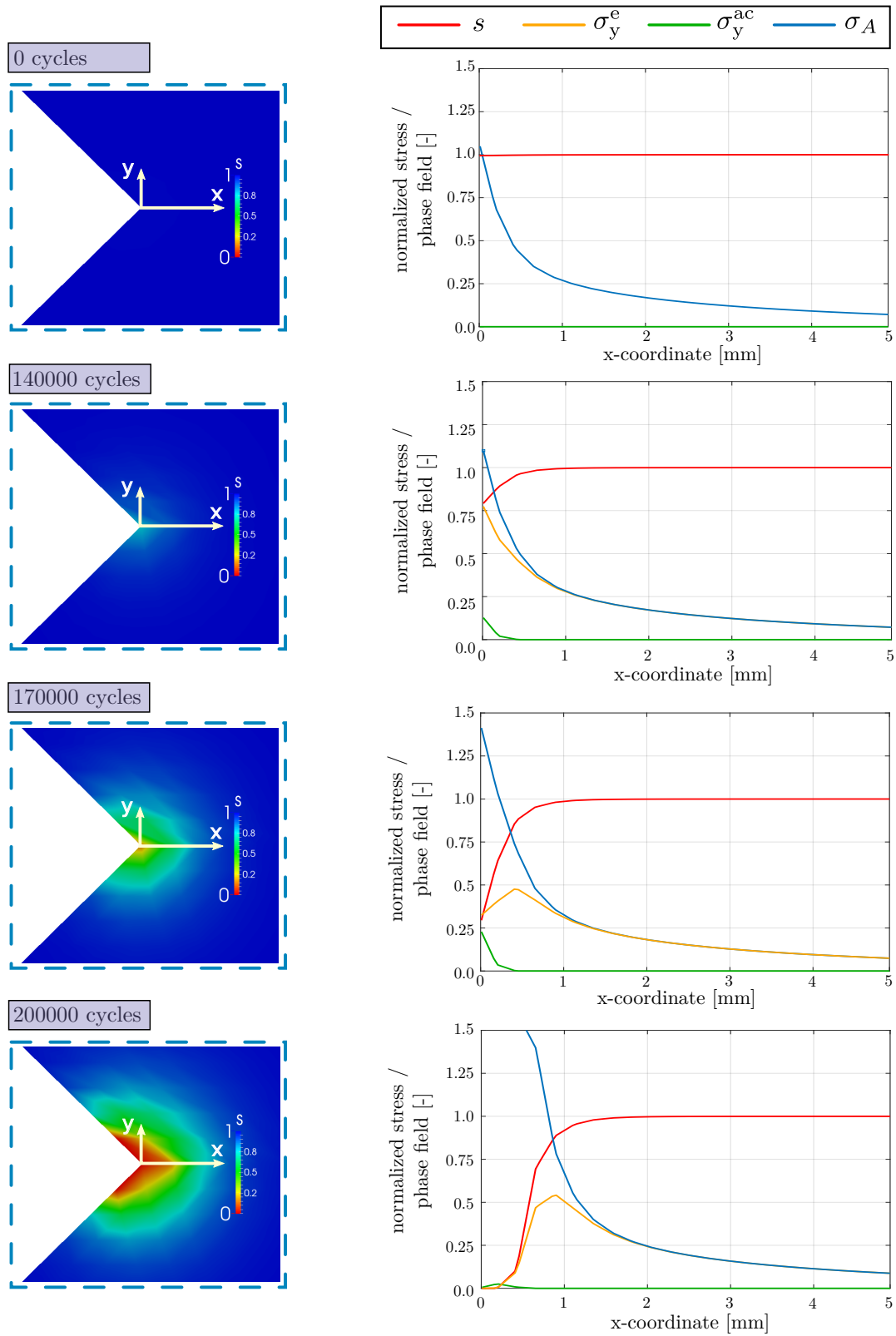


FIGURE 6.16: Evaluation of several crucial components of the phase field model over an increasing number of load cycles (left: phase field at notch tip, right: stress contributions on a horizontal straight path at $y = 0$).

evaluation of this crack initiation process is summarized in Figure 6.16. This evaluation illustrates the situation at the notch tip for four subsequent stages of applied load cycles. The contour plots of the phase field variable at the left side show the closer vicinity of the notch tip. This square section has an edge length of approximately $0.02L$. The plots on the right side show the corresponding state of several quantities along a path in x -direction with origin at the notch tip. The different lines represent the contributions to the stress in y -direction (w.r.t the coordinate system indicated in the contour plots), σ_y^e and σ_y^{ac} as well as the effective stress $\tilde{\sigma}$ according to (4.68). The contributions are normalized by the threshold stress A_D . Furthermore, the phase field variable is also plotted.

The illustrations at the top of Figure 6.16 represent the initial situation at the ramp up, which means full load applied within the first cycle. As depicted, for this situation the phase field remains unaltered proving that the static load alone can not cause cracking. The line plot also reveals that the driving stress quantity $\tilde{\sigma} > 1$. This means that the threshold stress is exceeded and therefore the onset of fatigue damage accumulation is occurring. As $s = 1$ the elastic stress σ_y^e and the effective stress $\tilde{\sigma}$ coincide. The stress contribution σ_y^{ac} is 0 as at this early stage no irreversible processes occurred. This configuration stays almost unaltered until enough damage is accumulated to have consequences. This is depicted by the two plots in the second row, which show the state after approximately $1.4 \cdot 10^5$ load cycles. The increase of fatigue related energies is indicated by the rise of σ_y^{ac} . This leads to a slight decrease of the phase field variable in the close vicinity of the notch tip indicating the onset of crack initiation. The drop of the phase field causes a decrease of the material's stiffness and hence the elastic stresses σ_y^e are degraded. The phase field at the notch tip has almost vanished showing a value of approximately $s = 0.25$ after $1.7 \cdot 10^5$ load cycles were applied. The elastic stress has decreased further. The driving stress quantity $\tilde{\sigma}$ expresses an increase according to the rise of deformation, which illustrates that $\tilde{\sigma}$ is an effective stress measure. Also the accumulative stress contribution shows further increase. The phase field variable completely vanishes at the position $x = 0$ and a fatigue crack has accordingly initiated at approximately $2.0 \cdot 10^5$ cycles, as illustrated by the two plots at the bottom. Also the corresponding contour plot now clearly indicates a phase field crack. Both stress contributions have vanished as they are completely degraded. Note, that with decreasing phase field variable the elastic stresses σ_y^e also decrease, while the accumulative stress contribution σ_y^{ac} does not (compare states $1.4 \cdot 10^5$ and $1.7 \cdot 10^5$ cycles). This holds, even if both are degraded by the same degradation function. This illustrates that the increase in fatigue related stresses resists degradation. The reason for this lies in the strong increase of the driving stress quantity $\tilde{\sigma}$. Finally, σ_y^{ac} vanishes once $s = 0$. However, this illustrates that within the here presented model the driving stress $\tilde{\sigma}$ must be an effective stress measure governed by the actual deformation. Otherwise, for constant load amplitudes the degradation of the phase field can not continue once the real elastic stress goes below the threshold for damage accumulation again. Generally, the sequence of the four states in Figure 6.16 illustrate how the situation of the stress components is shifted along the x -axis once the crack has initiated. The stress at the newly formed crack tip has increased causing the onset of the fatigue mechanism for the subsequent region. During this process, the point, where the effective stress $\tilde{\sigma}$ and the elastic stress σ_y^e diverge is almost constant. However, the driving quantity $\tilde{\sigma}$ at the crack tip is higher than at the notch tip before crack initiation. This leads to a smaller number of cycles necessary for crack growth compared to crack initiation, which qualitatively is in line with experimentally validated material behavior as outlined in e.g. Haibach, 2006.

Using the same parameters as in Table 6.2 except a slightly reduced threshold stress A_D , another simulation was run for a significantly higher number of simulation steps in order to assess the entire characteristic crack growth behavior. The node at the notch tip was initially set to $s = 0$ in order to reduce the period of crack initiation. Figure 6.17 summarizes the results. Contour plots of the phase field in the CT-specimen for several

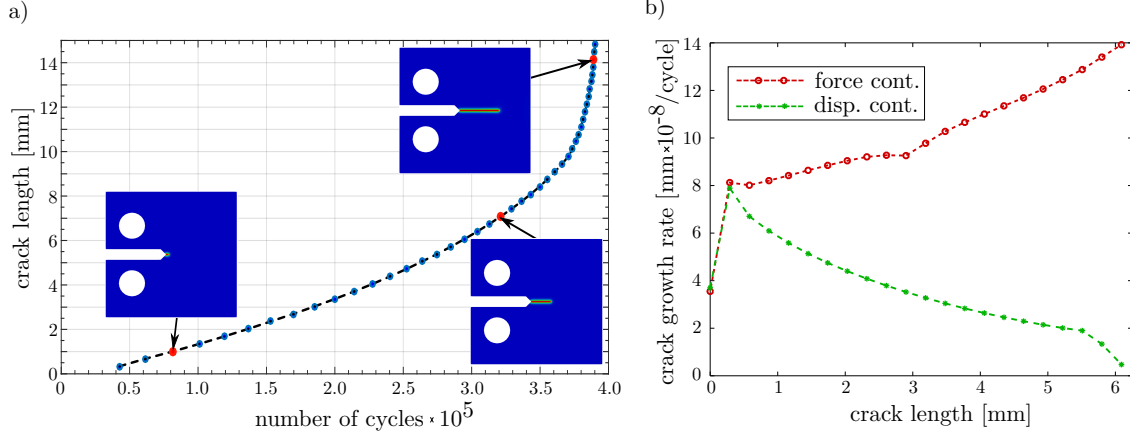


FIGURE 6.17: Results from fatigue crack growth simulation: a) N - a curve with indication of respective contour plots of s for specific states b) crack growth rate versus crack length for different types of loading.

specific N - a states are indicated in the diagram of Figure 6.17a), illustrating the current crack length versus the applied load cycles. Note that for practical reasons the real crack length is used in this illustration, which is measured from the tip of the V-notch to the maximum x -coordinate with $s = 0$. As depicted, a fatigue crack was finally propagated to a total length of 15 mm. The result of this simulation in terms of the fatigue crack evolution shows satisfying characteristics. The N - a curve shows a nonlinear behavior, which is very typical for this kind of experiment with the CT-specimen (see Dowling, 2013; Haibach, 2006; Schijve, 2009). As the load application stays unaltered during the testing, the lever to the crack tip becomes larger with increasing crack length and by this the magnitude of the stress increases leading to more rapid failure of the material. According to the results, this property is adequately modeled by the Wöhler law incorporated for the driving mechanism even for the period of brutal rupture. This is demonstrated by the almost vertical run of the N - a relation at the end of the simulation. The fact that the fatigue model reacts properly to changes in the load is also demonstrated by the evaluation shown in Figure 6.17b). The diagram shows the current crack growth rate with respect to the crack length for a simulation performed in force control mode and in displacement control mode. The respective growth rates were evaluated in the discrete form

$$\left(\frac{da}{dN} \right)_p \approx \frac{a_p - a_{p-1}}{N_p - N_{p-1}}. \quad (6.4)$$

The maximum displacement load was previously adapted in order to arrange an equal stress state for the initial growth period. Accordingly, the first two data points of both curves approximately coincide and the tests are comparable. After this initial phase, the growth

rates for force control and displacement control deviate. In contrast to the pure force control mode, where a longer crack causes higher peak stress, the constant displacement load leads to a relaxation of stresses as the crack propagates. Therefore, the crack growth rate decreases with increasing crack length as lower driving stresses enter the driving fatigue energy contribution. More characteristics of the model are revealed by the energy evaluation depicted in Figure 6.18. This plot shows the different contributions to the energy

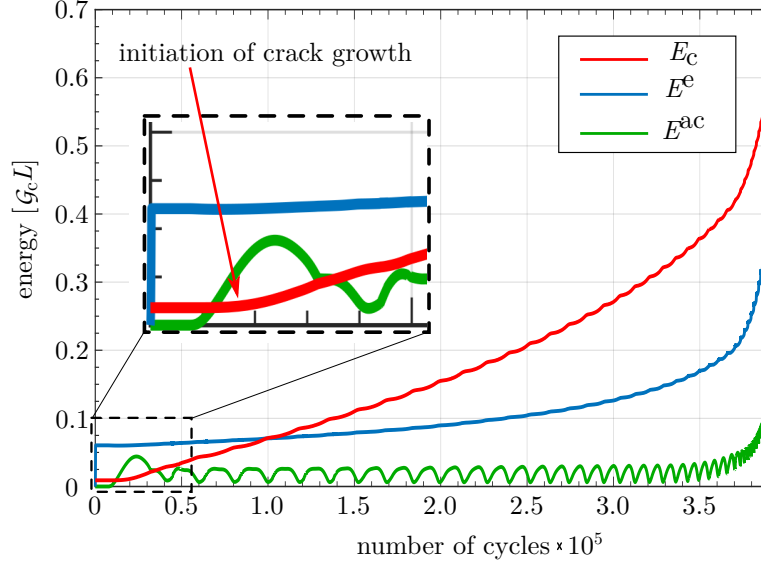


FIGURE 6.18: Evaluation of different energy contributions of the phase field model over a increasing number of load cycles.

with respect to the applied load cycles of the simulation from the force controlled simulation form above. The fatigue related energy contribution E^{ac} as well as the static strain energy E^e are scaled by a factor of 10 as they are small compared to the surface energy E_c . The plot shows an initial increase of the fatigue energy E^{ac} with growing cycle number, while E_c is constant for the first $0.2 \cdot 10^5$ cycles. Onset of crack growth is indicated by the first increase of the E_c contribution. The strain energy E^e reveals a jump function until this point. This shows that strain energy plays a secondary role as a driving force at this early stage. At the point, where the crack starts to grow the fatigue energy decreases. This occurs due to the consequence of the degradation by $h(s)$ with decreasing s . Further, a slight increase in strain energy can be recognized. This is caused by the rise of the stress level at the crack tip due to the larger crack. After this first period of crack growth the fatigue energy increases around the new crack tip, which is indicated by the second rise of E^{ac} . The described process starts again to further propagate the crack. Note, even if the strain energy slightly increases after the initial increment of crack propagation, it is almost constant for the main part of the simulation. It grows with a significantly higher slope only after about $2.5 \cdot 10^5$ cycles indicating brutal rupture as the stresses approach the static failure limit.

Within section 2.3 the Paris law was outlined as it is the main model to describe and quantify fatigue crack growth behavior for metallic materials. It deals with the cyclic stress intensity factor range, which incorporates the properties of geometry, loading conditions and also the current crack length. It is relevant to check whether the proposed phase

field model for fatigue crack growth renders Paris' linear function in a double logarithmic diagram. For this purpose, four interdependent simulations are run for the CT-specimen with different force amplitudes. The model parameters from Table 6.2 are applied in these simulations. The results are evaluated in Figure 6.20. For each simulation a fatigue crack was generated and grown to a total length of 6 mm. The crack growth curves obtained are shown in Figure 6.20a). Fewer cycles are needed to obtain a certain crack length with rising load amplitude. Within the Paris diagram Figure 6.20b), not only the data points of one particular simulation fall on a straight line but also the data of all four simulations together confirm the Paris law. A best fit linear function was determined (black line in Figure 6.20b) by the curve, fitting tool from Matlab using least square approximations. A very accurate coefficient of determination $R^2 = 0.996$ was obtained for the data set of the simulations. The underlying power law can be given by the Paris parameters $C = 2.8 \cdot 10^{-7} \frac{\text{mm/cycle}}{(\text{MPa}\sqrt{\text{m}})^m}$ and $m = 2.5$, which are realistic parameters for low alloy steels (see Dowling, 2013). In order to evaluate a broader range of different materials the underlying set of Wöhler parameters was varied within several additional simulations. The corresponding Paris laws are presented in the diagram of Figure 6.19. Four different parameter sets shown in the legend of the diagram are used for this evaluation. Only for the parameterization represented by the blue curve an additional simulation with a higher force amplitude was performed to confirm the linear behavior in the larger range. The intersection with the vertical axis represents the parameter C . It is mainly effected by the knee point cycle number n^D , where an increase of n^D causes a decrease of C . An increase of n^D leads to higher computation times in the first place. This can be counteracted by using a proper cycle jump increment. The slope of the Paris function is effected by the slope of the Wöhler curve and also by the knee point stress A_D , as the three other cases show.

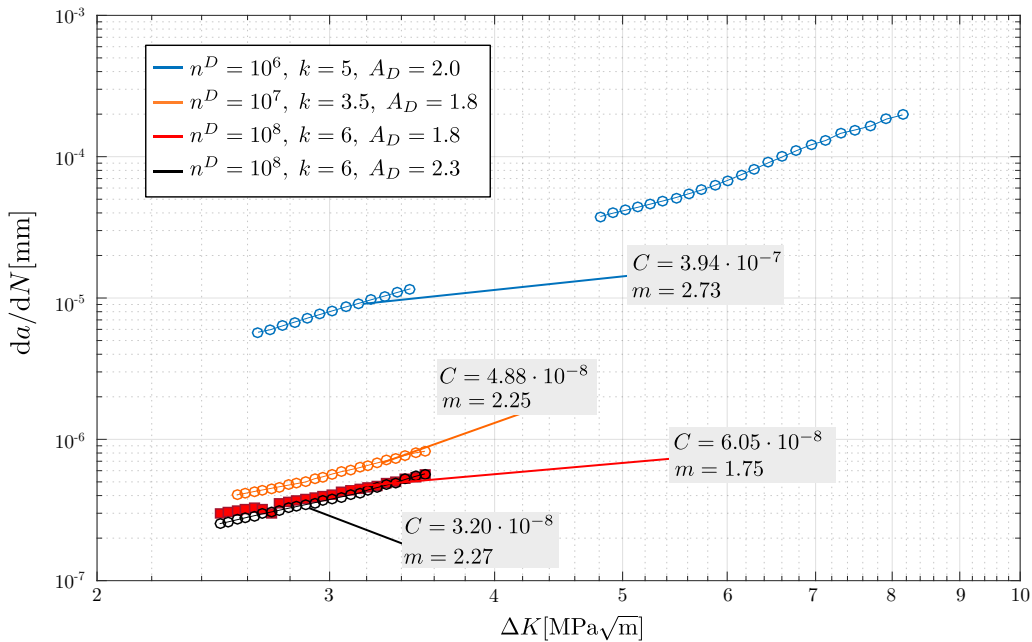


FIGURE 6.19: Evaluation of crack growth data from several phase field simulations with varying parameterization in a Paris' diagram.

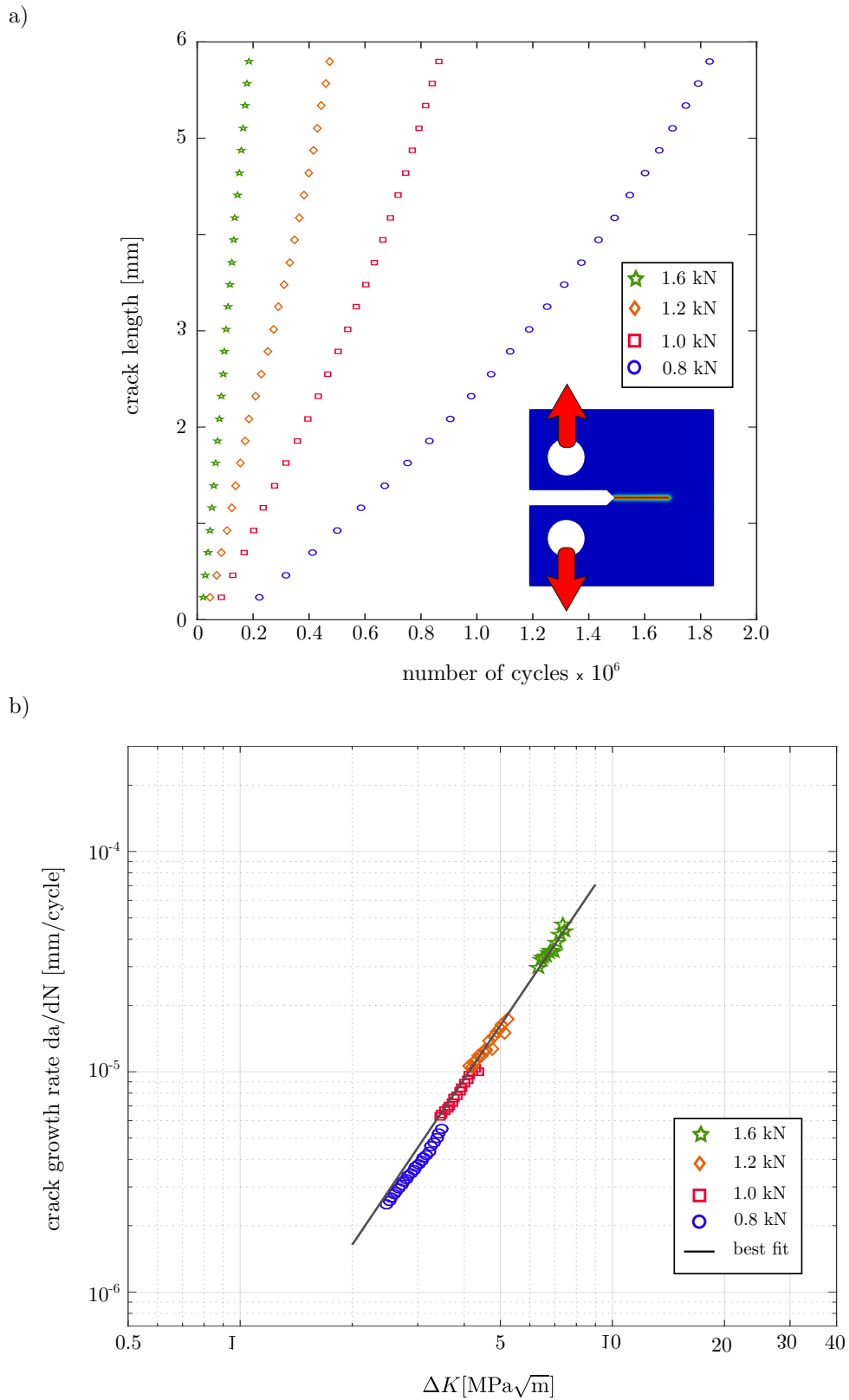


FIGURE 6.20: Evaluation of crack growth data from four different phase field simulations: a) N-a plot and b) double logarithmic diagram of crack growth rates vs. ΔK factor (Paris' diagram).

6.2.2 Effect of Load Sequence and Mean Load

So far only constant amplitude loading was considered. Much more relevant in terms of loading are sequences with varying amplitude loading. Within these sequences not only the maximum loads change but also the mean load. For example, the number of bearable load cycles decreases if the associated mean load is higher compared to a sequence with equal amplitude but lower mean load. The incorporation of the mean stress into the phase field model is described in section 4.2.6. The main difference to constant amplitudes is the use of a variable increment for the fatigue damage in (4.79). Within this paragraph, these modifications are assessed by means of different simulations for the CT-specimen introduced above. For all simulations outlined in the following the model parameters of Table 6.2 are used. The parameter $\bar{\gamma}$ for the mean stress effect was set to 0.3. In order to evaluate the model behavior regarding the mean stress effects several simulations were run, keeping the amplitude constant but with an altered stress ratio. The ratios of the energy contributions for crack initiation of six different stress ratios are shown in Figure 6.21. The bar plot illustrates, that the static strain energy becomes more relevant for higher stress ratios as it contributes more to the total energy, while the contribution of the fatigue energy decreases. In experiments, it was reported (see e.g. Haibach, 2006; Dowling, 2013; Schijve, 2009) that fatigue crack growth curves are shifted to higher rates for increasing stress ratios. Accordingly, the results in Figure 6.21 illustrate a very suitable property of the proposed model. The higher the static load the more pronounced the strain energy contributes to crack growth. Accordingly, to support crack growth at higher stress ratios

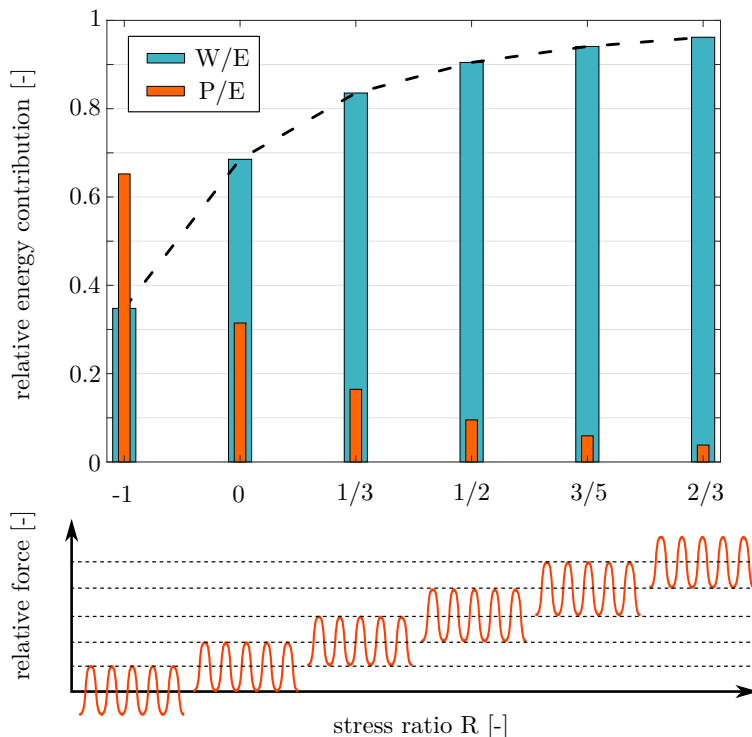


FIGURE 6.21: Comparison of required energy for fatigue crack initiation (W=strain energy, P= fatigue energy, E=total energy) for simulations with different stress ratios.

less accumulated fatigue energy is required. To check the general behavior in terms of crack growth rates the simulations are run further. The Paris diagram in Figure 6.22 illustrates the basic characteristic of fatigue crack growth for the six simulations in terms of crack growth rates. Consistently higher rates da/dN occur for increasing stress ratios R under equal stress intensity factor ranges. For comparison, the right diagram in Figure 6.22 illustrates the evolution of the crack length with respect to the absolute number of load cycles. An increase of the bearable load cycles for a lower stress ratio is found. In order to prove the ability of the present model general growth rates with respect to R for arbitrarily sequences are investigated. For this purpose further simulations are performed for the load sequences shown in Figure 6.23a), which bare equal maximum loads but different amplitudes. Interestingly, in the Paris diagram, depicted in Figure 6.23b), the da/dN curves show an increasing crack propagation speed.

Within the setup for the simulation with different stress ratios, the mean stress effect $\bar{\gamma}$ was kept constant. Generally, the function $f(L)$ in the damage increment controls the threshold stress for the fatigue accumulation. Therefore it determines the mean stress effect. Exemplary, for the stress ratio $R = 0.5$ the parameter $\bar{\gamma}$ was varied in order to illustrate the effect on Paris laws. The results are shown in Figure 6.24. It can be recognized, that the crack growth rates significantly decrease with the value of $\bar{\gamma}$. The choice of the $f(L)$ is not based on any identified law but is rather for illustrative purposes. However, the results clearly illustrate that an adaption of the proposed phase field model can be accomplished in this way. As the model allows for an arbitrary function $f(L)$ an adaption to observed material behavior is possible.

In addition to the effects of stress ratio and mean stress, the actual sequence has a very significant effect on the fatigue life of a structure. It matters a lot at which time a stress reversal occurs. Whether the proposed phase field model respects this property is analyzed by means of three fatigue simulations with the CT-specimen. The load sequences of the simulations are indicated in Figure 6.25a). This plot shows the envelope of the

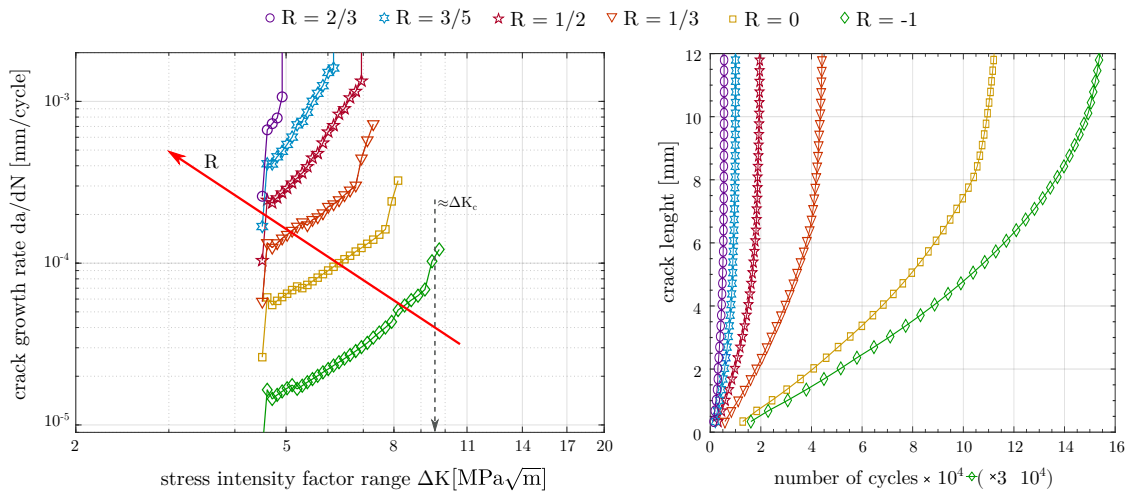


FIGURE 6.22: Results from cyclic phase field simulations with different stress ratios (left: crack growth rates, right: curves of crack length versus number of applied load cycles).

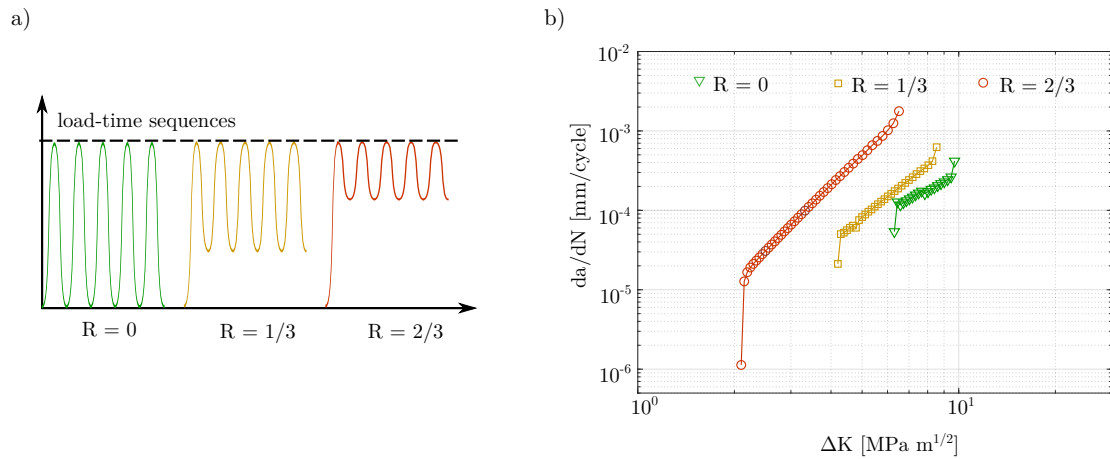


FIGURE 6.23: Paris curves obtained from phase field simulations for different stress ratios with equal maximum load.

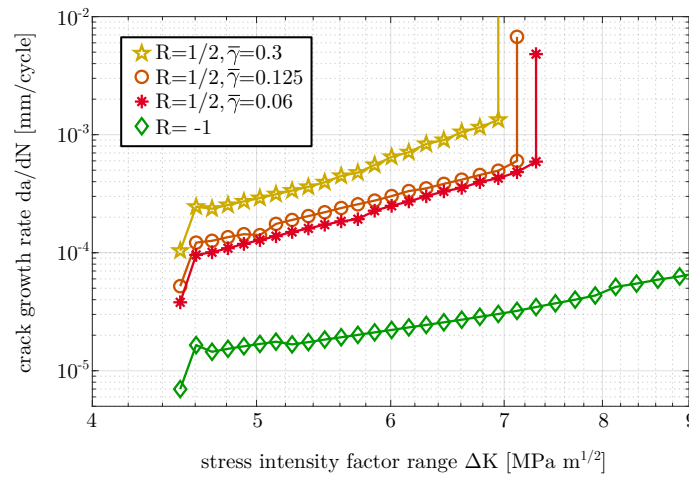


FIGURE 6.24: Paris curves obtained from phase field simulations with the CT-specimen for variation of mean stress parameter $\bar{\gamma}$.

applied cyclic loads. The cycle setup of all sequences yields $R = 0$. In addition to one case with constant maximum loading, two sequences were tested with increasing and decreasing maximum load, respectively. The resulting crack growth curves are shown in Figure 6.25b). Interestingly, the case with the high loads at the beginning and low loads at the end reveals the fastest crack propagation, as compared to a constant load or the sequence with the low loads first. This illustrates that the proposed fracture phase field model shows a sequence effect, even if Miner's rule is incorporated, which has no sequence sensibility due to its linear nature.

6.2.3 Mixed mode Loading

A crucial task in fatigue crack growth analyses is the knowledge of crack paths. This information may be included in a fail safe design of a structure. For trivial cases as the vertical loading of the CT-specimen, the path may be obvious. However, for real problems the present conditions in terms of load, deformation and crack interaction can vary all the

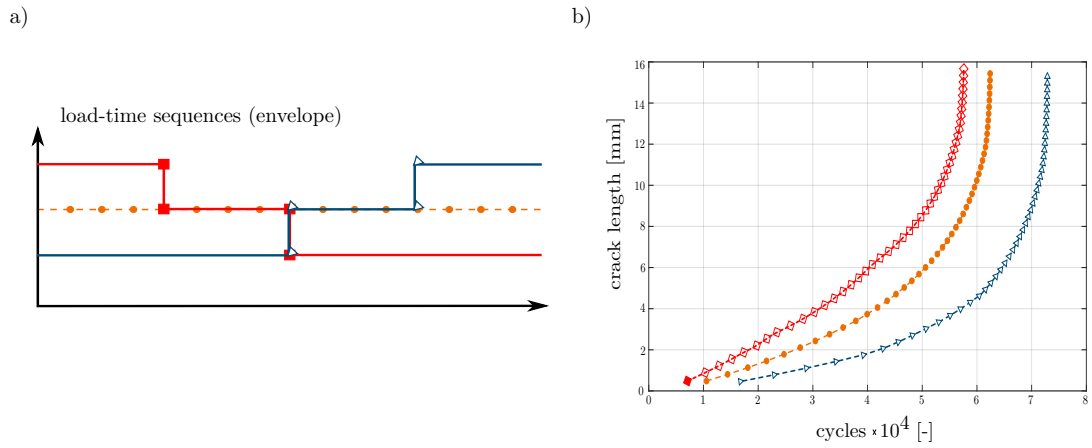


FIGURE 6.25: Evaluation of fatigue crack growth simulation for different load sequences: a) schematic illustration of sequences; b) Crack growth curves obtained for phase field simulations with the CT-specimen for the different sequences.

time and the fatigue evolution may become complex. To deal with mixed mode loading the first principle stress is proposed within section 4.2.4 as the driving force quantity of the fatigue mechanism. In order to verify this choice, two example cases where the deflection of the fatigue crack and also crack interaction is expected are simulated. The results are outlined in the following.

The first example is a classic mode II case. The specimen depicted in Figure 6.26 was set up for a simulation. The horizontal displacement of the upper half of the specimen induces a mode II like stress distribution at the initial crack tip, which is initially set to half of the specimen width. The specimen was discretized by 10880 finite elements and 11418 nodes. The mesh is depicted in Figure 6.26a). As the plot shows, the mesh was refined in the relevant area for crack evolution. The analytic solution of the mode II case (2.41) is visualized by the plot of Figure 6.26b). According to this diagram one finds the

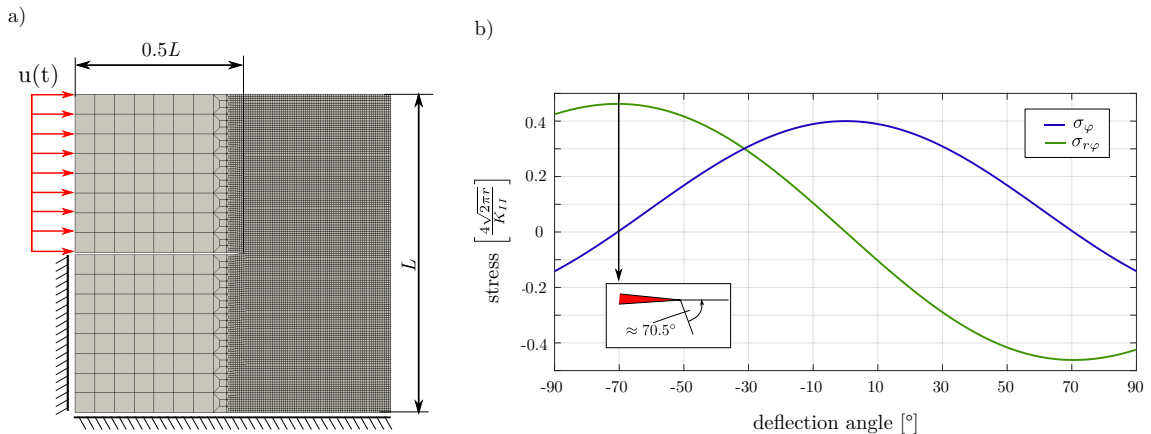


FIGURE 6.26: Fatigue phase field simulation of mode II load case: a) simulation setup, b) plot of relevant stress components in polar coordinates versus the potential deflection angle of the mode II load case.

maximum of the tangential stress at about -70.5° . The model parameters of Table 6.2 were used for the cyclic simulation.

The results of the simulation are shown in Figure 6.27 in form of contour plots of the phase field variable after an increasing number of load cycles. The plots clearly illustrate that the crack propagates under an angle of about -70° with respect to the horizontal direction. This is in agreement with the analytic definitions of the mode II load case. The results agree with experimental observations presented by Mahajan and Ravi-Chandar, 1989. This illustrates that using the first principle as driving stress is well chosen. The phase field model for fatigue fracture predicts the crack propagation in terms of growth rate and also in terms of growth direction. Note that in general a second crack would evolve towards the $+70.5^\circ$ direction. This is the direction of the minimum from the plot of Figure 6.26b). For the fatigue model no tension compression split was implemented. But the tension compression distinction is implicitly incorporated as the Wöhler curve neglects cycles with loads below the threshold A_D .

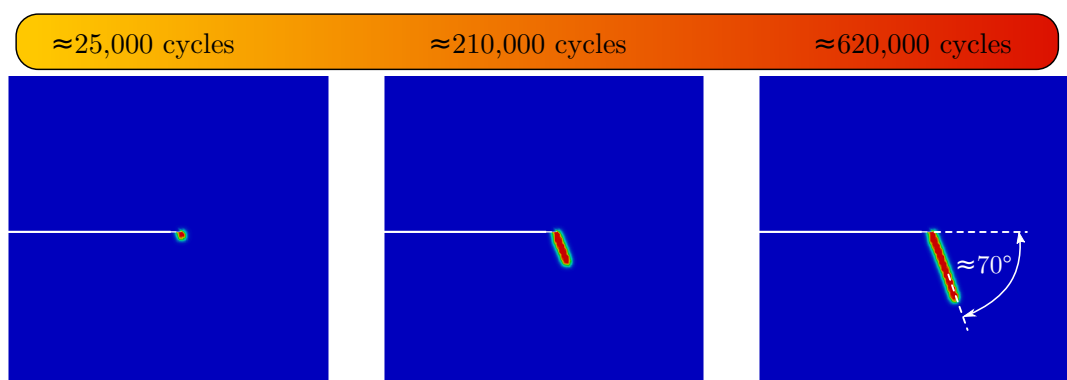


FIGURE 6.27: Contour plots of the phase field variable s over the domain of the mode II simulation set after increasing number of applied load cycles.

The second mixed mode numerical example is depicted in Figure 6.28 (top left). For this example crack curving is expected and the generalized driving stress quantity must be employed. The used specimen is a strip with a sharp notch on each side with a vertical distance to each other. The lower edge is fixed and a cyclic displacement load with $R = -1$ in vertical direction is applied at the top edge. The contour plots of the phase field variable s in Figure 6.28 illustrate the evolution of two fatigue cracks. The number of applied load cycles is indicated above the corresponding contour plots. The results show, that the fatigue cracks initiate at each notch at about 28000 cycles. The initial growth direction is purely horizontal. After a short period of horizontal crack extension (40000 cycles), it can be observed that the cracks start to grow away from each other. The cracks follow this direction for a while before both cracks change their direction again and propagate in the opposite direction. Then the cracks start to grow onto each other. The plot at the bottom right shows the final pattern of embraced cracks after the simulation was stopped at about 55000 cycles.

This characteristic behavior can be explained by an analytic solution of the crack tip field of linear elastic fracture mechanics. As outlined above, a crack is prone to extend straight in case of a pure mode I load. In contrast, it deflects under an angle of about 70.5° for a pure mode II case. Under an arbitrary load, both stress intensity factors K_I

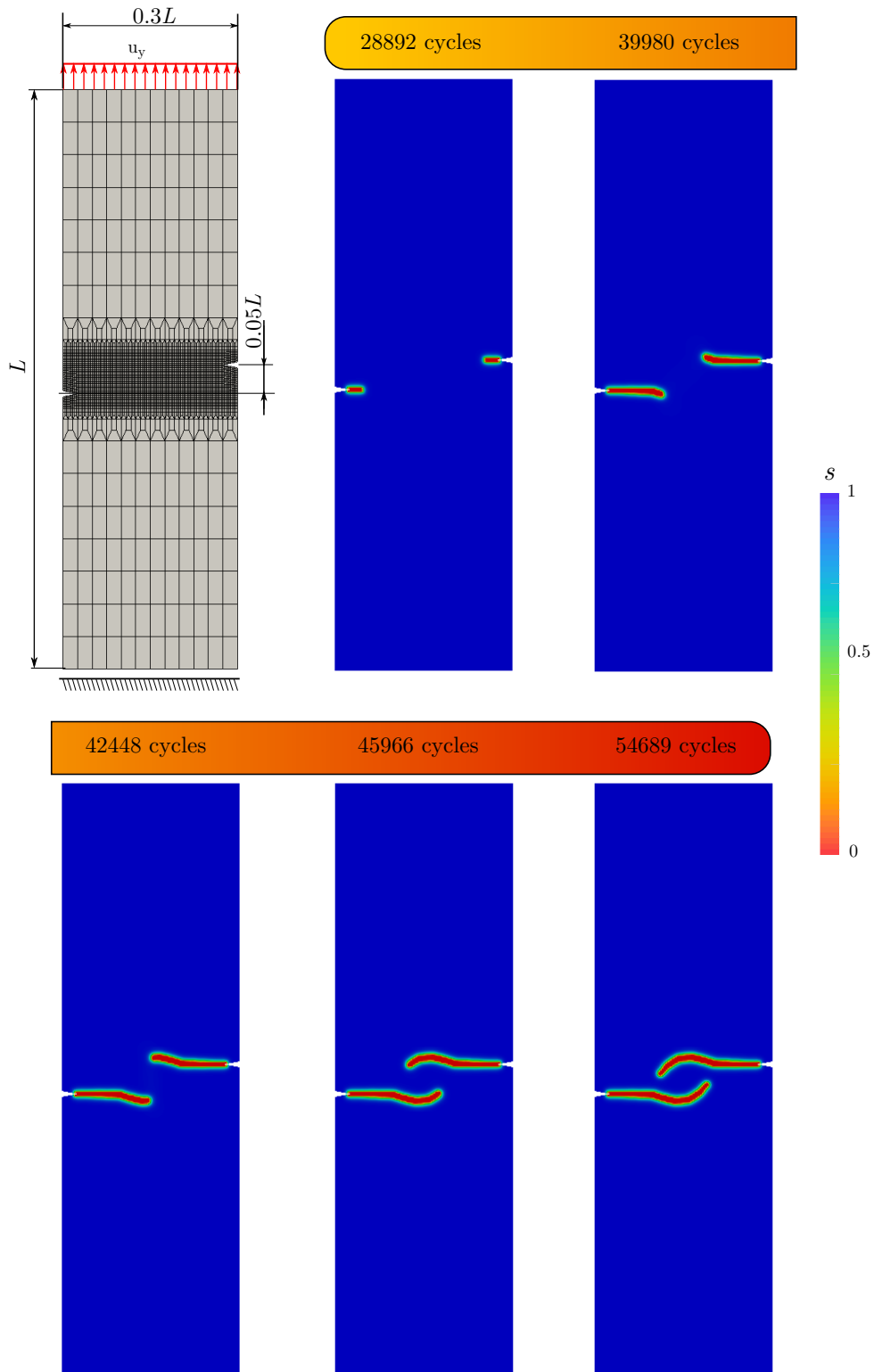


FIGURE 6.28: Setup (top left) and results (s after different numbers of applied load cycles) of crack interaction simulation with the fatigue phase field model.

and K_{II} contribute to the stress field at the crack tip. A crack that undergoes a load with a significant K_{II} contribution will deviate from the straight path. The K_{II} contribution for two parallel cracks of equal length in an infinite plate under a tensile load perpendicular to the cracks can be approximated by (see e.g. Gross and Seelig, 2011)

$$K_{II} = K_0 \frac{a^2}{2d^2} [\sin(4\theta) - \sin(2\theta)]. \quad (6.5)$$

In this equation, d is the distance between the cracks, $2a$ is their length and, θ is the skew angle. This angle becomes $\pi/2$ for stacked cracks and zero for collinear cracks. This function is plotted in Figure 6.29. The equation implies that the K_{II} contribution is positive as long as the cracks reveal a certain horizontal distance. After a certain angle θ is reached, the K_{II} contribution changes its sign and cracks grow in the opposite direction. This explains the crack paths as found by the simulation. Furthermore, the presented simulation results are also verified by results from Yates et al., 2008. The crack patterns obtained within this work were obtained for cyclic experiments and show very similar behavior.

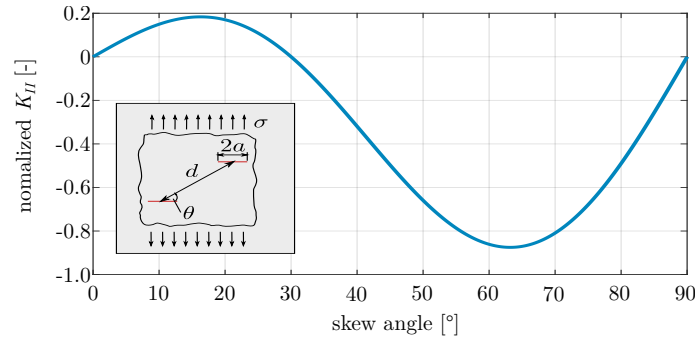


FIGURE 6.29: Illustration of K_{II} versus skew angle θ according to (6.5) for the crack interaction setup shown in Figure 6.28.

Chapter 7

Conclusion and Outlook

Within this work, the phase field method was applied in order to solve complex fracture problems. A basic model for brittle fracture proposed by Kuhn and Müller, 2010 was therefore enhanced in relevant areas. Accordingly, the general formulation is based on an energy density function proposed by Bourdin et al., 2000 as regularization of the variational concept for brittle fracture from Francfort and Marigo, 1998. The latter can be understood as an extension or generalization of the fracture criterion from Griffith, 1921, which is one of the basic concepts for the characterization of fracture mechanics.

The formulation of the inner energy for a body that may also contain cracks consists of a contribution representing the stored strain energy and another contribution accounting for all energy forms associated with the cracking process. The procedure to obtain the exact crack pattern for a certain boundary value problem is then in general the minimization of this energy formulation. Further, cracks are described within this concept as a smooth transition of an order parameter between 1 and 0. The evolution of this crack parameter is coupled with the mechanical balance law. Accordingly, the state of an energetic minimum takes possible cracks into account.

For the accurate prediction of crack propagation in materials that reveal an anisotropy of the fracture toughness the crack energy density was modified. This kind of anisotropy effects the crack path as in addition to the stress state in the vicinity of the crack tip the resistance function plays a significant role. Due to its directionality, the nonlocal part of the regularized crack energy density appears as a productive quantity to be modified. In fact the spatial gradient of this part was enhanced to the effect of a weighting of the particular spacial derivatives. The new model accordingly reveals a directionality regarding crack evolution as the evolution is governed by energy minimization. In detail, through this modification the anisotropy can be quantified by two additional parameters. These parameters describe the orientation of the considered two fold anisotropy and also its intensity. The obtained anisotropic phase field fracture model was checked for reliability in terms of the predicted crack paths. The presented results show that the modification of the crack energy causes a divergence of the crack path with respect to the path for an isotropic material. The evaluation of a parameter study clearly illustrates the consistency of the parameterization as the respective crack deflection increases with increasing intensity. Furthermore, the crack paths found in experimental investigations with anisotropic aluminum plates can be reproduced by the new phase field model.

A second phase field model is presented in the present work that aims to provide a description of the complex phenomenon of fatigue crack growth. The phenomenon of cyclic

fatigue occurs already at stress levels far below static design limits. This renders a problem in terms of the principal driving force mechanism of the phase field paradigm as the comparable low load can not cause a state such that the internal energy would benefit from cracking. Within the presented phase field approach an additional energy contribution was established in order to overcome this issue. Within the phase field formulation this contribution represents energies associated with cyclic slip irreversibilities caused by cyclic loading and unloading. A simple linear law, namely Miner's rule is utilized for the evaluation of the current state of fatigue damage within the material. The physical connection of this empirical law to crack propagation is illustrated. In order to bring this energy contribution up to the order of the static limit a piecewise defined function of the fatigue damage is incorporated. This function rapidly increases once a critical value of fatigue damage is exceeded at a certain location. In order to overcome the issue of simulating the huge number of bearable load cycles until the fatigue mechanism reveals macroscopic consequences in terms of crack nucleation or propagation the cycle jump principle is applied. This scheme proposes to summarize a certain amount of load cycles to blocks and evaluate the corresponding damage increment for the entire block. Accordingly, the required simulation steps can be reduced by the factor of the used block size. Numerical simulations of the described phase field model for fatigue fracture were performed with several different two dimensional geometries. The respective results verify reasonable results in terms of fatigue crack nucleation and growth of the model. In order to validate whether the obtained crack growth behavior is really sufficient in accordance with the phenomenon of fatigue several different investigations of the crack growth rates were performed. In this regard, it can be shown that Paris' equation, a principal law for the quantification of fatigue crack growth, is reproduced by the presented phase field model. Therefore, it may be emphasized that in contrast to classical fatigue fracture prediction tools Paris' law is an outcome from the model and is not as usual needed a prior. Furthermore, the model is able to account for several influences on the fatigue life. Well known phenomena from fatigue fracture mechanics as stress ratio dependence of the Paris' parameters or even load sequence effects are adequately predicted. Interestingly, the latter holds even if the Miner rule, a linear relation, is used to drive the crack propagation. In a further part of simulations, the model is investigated regarding its capability for the general load case of mixed mode loading. The key issue to enable arbitrary directions for cracking is to incorporate the correct driving stress quantity. The first principal stress was adopted as a consequence of respective analytic criteria. The obtained fatigue crack path for a mode II simulation reveals a deflection angle, which clearly matches analytic predictions as well as experimental results. Also a test case, where crack interaction effects play a significant role was investigated and the results can also be validated by experimental results.

In conclusion, the proposed enhancements of the phase field fracture method contribute to a more general and more flexible tool for the simulation of fracture processes. A sound basis for even more complex anisotropies as well as fatigue crack growth is now available within the library of phase field fracture models. However, so far the framework must not be considered comprehensive. It has been shown that the principle directionality of the fracture toughness can be handled, but there are still more complex anisotropies to be considered. In further studies the introduced resistance tensor for the description of the anisotropy may be further modified in order to represent materials with more complex polar plots of the critical energy release rate as proposed in e.g. Li et al., 2015; Roman et al., 2013. Also, the model must be applied to a wider range of materials in order to

validate its general reliability. For example, materials produced by additive manufacturing processes like 3D printing may provide a sufficient spread of possibilities since the material parameters can be varied by the process set. In the case of the phase field model for fatigue a number of potential enhancements may be mentioned. The fatigue phenomenon is very sensitive to a number of influences from the environment as temperature or also the surrounding medium. Also plastic deformations can play a significant role in the fatigue life. Specifically, this becomes relevant for the modeling of retardation effects caused by single overloads within a load time sequence. Furthermore, considering the amplitude range of low cycle fatigue, plasticity is relevant for the application of the proposed phase field model.

Bibliography

- Aldakheel, F., P. Wriggers, and C. Miehe (2018a). “A modified Gurson-type plasticity model at finite strains: formulation, numerical analysis and phase-field coupling”. In: *Computational Mechanics* 62, pp. 815–833.
- Aldakheel, F., B. Hudobivnik, A. Hussein, and P. Wriggers (2018b). “Phase-Field Modeling of Brittle Fracture Using an Efficient Virtual Element Scheme”. In: *Computer Methods in Applied Mechanics and Engineering* 341.
- Alessi, R., S. Vidoli, and L. DeLorenzis (2017). “A phenomenological approach to fatigue with a variational phase-field model: The one-dimensional case.” In: *Engineering Fracture Mechanics* 190, pp. 53–73.
- Altenbach, H. (2012). *Kontinuumsmechanik—Einführung in die materialunabhängigen und materialabhängigen Gleichungen*. 2nd ed. Berlin: Springer, p. 342.
- Ambati, M., T. Gerasimov, and L. DeLorenzis (2015). “A review on phase-field models of brittle fracture and a new fast hybrid formulation”. In: *Computational Mechanics* 55.2, pp. 383–405.
- Ambrosio, L. (1990). “Existence theory for a new class of variational problems”. In: *Archive for Rational Mechanics and Analysis* 111, pp. 291–322.
- Ambrosio, L. and V. M. Tortorelli (1990). “Approximation of functional depending on jumps by elliptic functional via Γ -convergence”. In: *Communications on Pure and Applied Mathematics* 43.8, pp. 999–1036.
- Amor, H., J.-J. Marigo, and C. Maurini (2009). “Regularized formulation of the variational brittle fracture with unilateral contact: Numerical experiments”. In: *Journal of the Mechanics and Physics of Solids* 57.8, pp. 1209–1229.
- ASTM (2009). *ASTM E399-09, Standard Test Method for Linear-Elastic Plane-Strain Fracture Toughness K_{Ic} of Metallic Materials*. West Conshohocken, PA: ASTM International.
- Badillo, A. (2015). “Quantitative phase-field modeling for wetting phenomena”. In: *Physical review. E, Statistical, nonlinear, and soft matter physics* 91.
- Bathe, K.-J. (1996). 1st ed. New Jersey: Prentice Hall, p. 1012.
- Betten, J. (2001). *Kontinuumsmechanik—Elastisches und inelastisches Verhalten isotroper und anisotroper Stoffe*. 2nd ed. Berlin: Springer, p. 556.

- Betten, J. (2004). *Finite Elemente für Ingenieure 2 – Variationsrechnung, Energiemethoden, Näherungsverfahren, Nichtlinearitäten, Numerische Integrationen*. 2nd ed. Heidelberg: Springer, p. 307.
- Bhate, D. N., A. Kumar, and A. F. Bower (2000). “Diffuse interface model for electromigration and stress voiding”. In: *Journal of Applied Physics* 87.4, pp. 1712–1721.
- Bograd, F., P. Lestriez, and Y. Q. Guo (2008). “Numerical modeling of fatigue damage and fissure propagation under cyclic loadings”. In: *International Journal of Damage Mechanics* 17, pp. 1056–7895.
- Borden, M. J., T. J. R. Hughes, C. M. Landis, and C. V. Verhoosel (2014). “A higher-order phase-field model for brittle fracture: Formulation and analysis within the isogeometric analysis framework”. In: *Computer Methods in Applied Mechanics and Engineering* 273, pp. 100–118.
- Borden, M. J., T. J. R. Hughes, C. M. Landis, and A. Anvari (2016). “A phase-field formulation for fracture in ductile materials: Finite deformation balance law derivation, plastic degradation, and stress triaxiality effects”. In: *Computational Methodes in Applied Mechanics and Engineering* 312, pp. 130–166.
- Bourdin, B. (2007). “Numerical implementation of the variational formulation of brittle fracture”. In: *Interfaces and Free Boundaries - INTERFACE FREE BOUND* 9, pp. 411–430.
- Bourdin, B., G. A. Francfort, and J-J. Marigo (2000). “Numerical experiments in revisited brittle fracture”. In: *Journal of the Mechanics and Physics of Solids* 48, pp. 797–826.
- Carrara, P., A. Marreddy, R. Alessi, and L. DeLorenzis (2018). “A novel framework to model the fatigue behavior of brittle materials based on a variational phase-field approach.” In: *arXiv: Materials Science*.
- Chaboche, J. L. and P. M. Lesne (1988). “A non-linear continuous fatigue damage model”. In: *Fatigue Fracture of Engineering Materials and Structures* 11, pp. 1–17.
- Chan, S. (1977). “Steady-state kinetics of diffusionless first order phase transformation”. In: *The Journal of Chemical Physics* 67.12, pp. 5755–5762.
- Chen, L. and Y. Wang (1996). “The Continuum Field Approach to Modeling Microstructural Evolution”. In: *Journal of the Minerals, Metals and Materials Society* 48.
- Chen, L.Y., G.Z. Wang, J.P. Tan, F.Z. Xuan, and S.T. Tu (2013). “Effects of residual stress on creep damage and crack initiation in notched CT specimens of a Cr–Mo–V steel”. In: *Engineering Fracture Mechanics* 97, pp. 80–91.
- Chow, C.L. and Y. Wei (1991). “A model of continuum damage mechanics for fatigue failure”. In: *International Journal of Fracture* 50, pp. 301–316.

- Ciavarella, M., P. D'antuono, and A. Papangelo (2018). "On the connection between Palmgren-Miner rule and crack propagation laws". In: *Fatigue & Fracture of Engineering Materials & Structures* 41.7, pp. 1469–1475.
- Clormann, U. and T. Seeger (1986). "Rainflow-HCM. Ein Zählverfahren für Betriebsfestigkeitsnachweise auf Werkstoffmechanischer Grundlage". In: *Fachgebiet Werkstoffmechanik, TH Darmstadt*.
- Das, A., H.W. Viehrig, F. Bergner, C. Heintze, E. Altstadt, and J. Hoffmann (2017). "Effect of microstructural anisotropy on fracture toughness of hot rolled 13Cr ODS steel – The role of primary and secondary cracking". In: *Journal of Nuclear Materials* 491, pp. 83–93.
- Dassault Systemes (2020). *Abaqus CAE description*. URL: <https://www.3ds.com/products-services/simulia/products/abaqus/abaquscae/> (visited on 04/10/2021).
- De Giorgi, E. and G. Dal Maso (1983). "Γ-Convergence and calculus of variations". In: *Mathematical Theories of Optimization*. Berlin, Heidelberg: Springer, pp. 121–143. ISBN: 978-3-540-39473-0.
- De Giorgi, E., M. Carriero, and A. Leaci (1989). "Existence theorem for a minimum problem with free discontinuity set". In: *Archive for Rational Mechanics and Analysis* 108, pp. 195–218.
- Diewald, F., M. Lautenschlaeger, S. Stephan, K. Langenbach, C. Kuhn, S. Seckler, H. J. Bungartz, H. Hasse, and R. Müller (2020). "Molecular dynamics and phase field simulations of droplets on surfaces with wettability gradient". In: *Computer Methods in Applied Mechanics and Engineering* 361, p. 112773.
- DIN (2016). *Schwingfestigkeitsversuch - Durchführung und Auswertung von zyklischen Versuchen mit konstanter Lastamplitude für metallische Werkstoffproben und Bauteile*. Deutsches Institut für Normung.
- Dineva, P., D. Gross, R. Mueller, and T. Rangelov (2011). "Dynamic stress and electric field concentration in a functionally graded piezoelectric solid with a circular hole". In: *Journal of Applied Mathematics and Mechanics* 91.2, pp. 110–124.
- Dowling, N. E. (2013). *Mechanical Behavior of Materials: Engineering Methods for Deformation, Fracture, and Fatigue*. 4th ed. Person, p. 955.
- Erdogan, F. and G. C. Sih (1963). "On the crack extension in plates under plane loading and transverse shear". In: *Journal of Basic Engineering* 85.4, pp. 519–525.
- Ettrich, T (2020). *Analyse und Validierung eines Phasenfeldmodells für anisotropes Riswachstum*. BA thesis. Technische Universität Kaiserslautern, dept. Mechanical and Process Engineering.
- Fish, J. and C. Oskay (2005). "A Nonlocal Multiscale Fatigue Model". In: *Mechanics of Advanced Materials and Structures* 12.6, pp. 485–500.

- Fish, J. and Q. Yu (2002). “Computational Mechanics of Fatigue and Life Prediction Composite Materials and Structures”. In: *Computer Methods in Applied Mechanics and Engineering* 191, pp. 4827–4849.
- Flouriot, S., S. Forest, G. Cailletaud, A. Köster, L. Rémy, B. Burgardt, V. Gros, S. Mosset, and J. Delautre (2003). “Strain localization at the crack tip in single crystal CT specimens under monotonous loading: 3D Finite Element analyses and application to nickel-base superalloys”. In: *International Journal of Fracture* 124, pp. 43–77.
- Forman, R. G., V. Shivakumar, J. W. Cardinal, L. C. Williams, and P. C. McKeighan (2005). “Fatigue Crack Growth Database for Damage Tolerance Analysis”. In: *National Technical Information Service*, p. 126.
- Francfort, G.A. and J.-J. Marigo (1998). “Revisiting brittle fracture as an energy minimization problem”. In: *Journal of the Mechanics and Physics of Solids* 46.8, pp. 1319–1342.
- Fried, E. and M.E. Gurtin (1994). “Dynamic solid-solid transitions with phase characterized by an order parameter”. In: *Physica D* 72.4, pp. 287–308.
- Garimella, Rao (2009). “Conformal Refinement of Unstructured Quadrilateral Meshes”. In: pp. 31–44. ISBN: 978-3-642-04318-5.
- Goldstein, R. V. and R. L. Salganik (1974). “Brittle fracture of solids with arbitrary cracks”. In: *International Journal of Fracture* 10, pp. 507–523.
- Gook, T. S. (1993). “Developing fatigue crack growth data using the round compact tension specimen”. In: *International Journal of Fracture* 23, R61–R64.
- Griffith, A. A. (1921). “The phenomena of rupture and flow in solids”. In: *Philosophical Transactions of the Royal Society of London* 221, pp. 163–198.
- Gross, D. and W. Becker (2002). *Mechanik elastischer Körper und Strukturen*. 1st ed. Heidelberg: Springer, p. 200.
- Gross, D. and Th. Seelig (2011). *Bruchmechanik—Mit einer Einführung in die Mikromechanik*. 5th ed. Heidelberg: Springer, p. 350.
- Gurson, A. L. (1977). “Continuum Theory of Ductile Rupture by Void Nucleation and Growth: Part I—Yield Criteria and Flow Rules for Porous Ductile Media”. In: *Journal of Engineering Materials and Technology* 99.1, pp. 2–15.
- Gurtin, M. E. (1996). “Generalized Ginzburg-Landau and Cahn-Hilliard equations based on a microforce balance”. In: *Physica D* 92, pp. 178–192.
- Haibach, E. (2006). *Betriebsfestigkeit—Verfahren und Daten zur Bauteilberechnung*. 3rd ed. Heidelberg: Springer, p. 759.

- Hakim, V. and A. Karma (2009). “Laws of crack motion and phase-field models of fracture”. In: *Journal of the Mechanics and Physics of Solids* 57.2, pp. 342–368.
- Irwin, G. R. (1957). “Analysis of stresses and strains near the end of a crack traversing plate”. In: *Philosophical Transactions of the Royal Society of London* 21, pp. 361–364.
- Judt, P. O. and A. Ricoeur (2015). “Crack growth simulation of multiple cracks systems applying remote contour interaction integrals”. In: *Theoretical and Applied Fracture Mechanics* 75, pp. 78–88.
- Judt, P. O., A. Ricoeur, and G. Linek (2015). “Crack path prediction in rolled aluminum plates with fracture toughness orthotropy and experimental validation”. In: *Engineering Fracture Mechanics* 138, pp. 33–48.
- Karma, A., D. Kessler, and H. Levine (2001). “Phase-Field Model of Mode III Dynamic Fracture”. In: *Physical Review Letters* 87 (4), p. 045501.
- Kazaryan, A., Y. Wang, S. A. Dregia, and R. B. Patton (2001). “Grain growth in systems with anisotropic boundary mobility: Analytical model and computer simulation”. In: *Phys. Rev. B* 63 (18), p. 184102.
- Kfourri, A.P. (1996). “Crack extension under mixed-mode loading in an anisotropic mode-asymmetric material in respect of resistance to fracture”. In: *Fatigue and Fracture of Engineering Materials and Structures* 19.1, pp. 27–38.
- Kim, H.-K., S. G. Kim, W. Dong, I. Steinbach, and B.-J. Lee (2014). “Phase-field modeling for 3D grain growth based on a grain boundary energy database”. In: *Modelling and Simulation in Materials Science and Engineering* 22.3, p. 034004.
- Kitware (2016). *Paraview Webpage*. URL: <https://www.paraview.org/> (visited on 04/10/2021).
- Kobayashi, R. (1993). “Modeling and numerical simulations of dendritic crystal growth”. In: *Physica D: Nonlinear Phenomena* 63.3, pp. 410–423.
- Koslowski, M., A.M. Cuitiño, and M. Ortiz (2002). “A phase-field theory of dislocation dynamics, strain hardening and hysteresis in ductile single crystals”. In: *Journal of the Mechanics and Physics of Solids* 50.12, pp. 2597–2635.
- Kuhn, C. and R. Mueller (2016). “A discussion of fracture mechanisms in heterogeneous materials by means of configurational forces in a phase field fracture model”. In: *Computer Methods in Applied Mechanics and Engineering* 312, pp. 95–116.
- Kuhn, C. and R. Müller (2010). “A continuum phase field model for fracture”. In: *Engineering Fracture Mechanics* 77, pp. 3625–3634.
- Kuhn, C. and R. Müller (2010). “Exponential Finite Elements for a Phase Field Fracture Model”. In: *PAMM* 10.1, pp. 121–122.

- Kuhn, C., A. Schlüter, and R. Müller (2015). “On degradation functions in phase field fracture models”. In: *Computational Materials Science* 108, pp. 374–384.
- Kuhn, C., T. Noll, and R. Müller (2016). “On phase field modeling of ductile fracture”. In: *GAMM Mitteilungen* 39, pp. 35–54.
- Kuna, M. (2010). 2nd ed. Wiesbaden: Vieweg Teubner, p. 446.
- Leguillon, D. (2002). “Strength or toughness? A criterion for crack onset at a notch”. In: *European Journal of Mechanics - A/Solids* 21.1, pp. 61–72.
- Lemaitre, J. (1992). *A course on damage mechanics*. 1st ed. Heidelberg: Springer, p. 210.
- Li, B., C. Peco, D. Millán, I. Arias, and M. Arroyo (2015). “Phase-field modeling and simulation of fracture in brittle materials with strongly anisotropic surface energy”. In: *International Journal for Numerical Methods in Engineering* 102.3-4, pp. 711–727.
- Mahajan, R. V. and K. Ravi-Chandar (1989). “An experimental investigation of mixed-mode fracture”. In: *International Journal of Fracture* 41, pp. 235–252.
- Marigo, J. J. (1985). “Modelling of brittle and fatigue damage for elastic material by growth of microvoids”. In: *Engineering Fracture Mechanics* 21, pp. 861–874.
- Mathworks (2021). *Python Programming Language*. URL: <https://de.mathworks.com/products/matlab.html> (visited on 04/10/2021).
- McFadden, G. B. and A. A. Wheeler (2002). “On the Gibbs Adsorption Equation and Diffuse Interface Models”. In: *Proceedings: Mathematical, Physical and Engineering Sciences* 458.2021, pp. 1129–1149.
- Mesgarnejad, A., A. Imanian, and A. Karma (2019). “Phase-field models for fatigue crack growth”. In: *Theoretical and Applied Fracture Mechanics* 103.
- Mianroodi, J. R. and B. Svendsen (2015). “Atomistically determined phase-field modeling of dislocation dissociation, stacking fault formation, dislocation slip, and reactions in fcc systems”. In: *Journal of the Mechanics and Physics of Solids* 77, pp. 109–122. ISSN: 0022-5096.
- Miehe, C., M. Hofacker, and F. Welschinger (2010a). “A phase field model for rate-independent crack propagation: Robust algorithmic implementation based on operator splits”. In: *Computer Methods in Applied Mechanics and Engineering* 199.45, pp. 2765–2778.
- Miehe, C., F. Welschinger, and M. Hofacker (2010b). “Thermodynamically consistent phase-field models of fracture: Variational principles and multi-field FE implementations”. In: *International Journal for Numerical Methods in Engineering* 83.10, pp. 1273–1311.

- Miehe, C., F. Aldakheel, and T. Stephan (2016). “Phase-Field Modeling of Ductile Fracture at Finite Strains. A Robust Variational-Based Numerical Implementation of a Gradient-Extended Theory by Micromorphic Regularization: Phase Field Modeling of Ductile Fracture”. In: *International Journal for Numerical Methods in Engineering*. DOI: 10.1002/nme.5484.
- Miner, M. A. (1945). “Cumulative damage in fatigue”. In: *Journal of Applied Mechanics* 12, A159–A164.
- Moreno-Valle, E.C., W. Pachla, M. Kulczyk, I. Sabirov, and A. Hohenwarter (2019). “Anisotropy of Tensile and Fracture Behavior of Pure Titanium after Hydrostatic Extrusion”. In: *MATERIALS TRANSACTIONS* 60.10, pp. 2160–2167.
- Mughrabi, Hael (2013). “Microstructural fatigue mechanisms: Cyclic slip irreversibility, crack initiation, non-linear elastic damage analysis”. In: *International Journal of Fatigue* 57, pp. 2–8.
- Mumford, D. and J. Shah (1985). “Boundary detection by minimizing functionals”. In: *IEEE Proceedings on Computer Vision and Pattern Recognition*.
- Nestler, B. (1999). “A multiphase-field model: sharp interface asymptotics and numerical simulations of moving phase boundaries and multijunctions”. In: *Journal of Crystal Growth* 204.1, pp. 224–228.
- Nestler, B. and A. A. Wheeler (2002). “Phase-field modeling of multi-phase solidification”. In: *Computer Physics Communications* 147.1. Proceedings of the Europhysics Conference on Computational Physics Computational Modeling and Simulation of Complex Systems, pp. 230–233.
- O’Hara, P., J. Hollkamp, C.A. Duarte, and T. Eason (2016). “A two-scale generalized finite element method for fatigue crack propagation simulations utilizing a fixed, coarse hexahedral mesh”. In: *Computational Mechanics* 57, pp. 55–74.
- Paris, P.C. and F. Erdogan (1963). “A Critical Analysis of Crack Propagation Laws”. In: *Journal of Basic Engineering* 85, pp. 528–539.
- Provatas, N. and K. Elder (2010). *Phase Field Methodes in Material Science and Engineering*. 1st ed. Berlin: Wiley, p. 300.
- Python Software Foundation (2021). *Python Programming Language*. URL: <https://www.python.org/> (visited on 04/10/2021).
- Radaaj, D. and M. Vormwald (2007). *Ermüdungsfestigkeit–Grundlagen für Ingenieure*. 3rd ed. Heidelberg: Springer, p. 688.
- Rajkotwala, A.H., A. Panda, E.A.J.F. Peters, M.W. Baltussen, C.W.M. [van der Geld], J.G.M. Kuerten, and J.A.M. Kuipers (2019). “A critical comparison of smooth and sharp interface methods for phase transition”. In: *International Journal of Multiphase Flow* 120, p. 103093.

- Rice, J. (1968). “A Path Integral and the Approximate Analysis of Strain Concentration by Notches and Cracks”. In: *Journal of Applied Mechanics* 35, pp. 379–386.
- Ritchie, R. O. (1977). “Near-Threshold Fatigue Crack Propagation in Ultra-High Strength Steel: Influence of Load Ratio and Cyclic Strength”. In: *Journal of Engineering Materials and Technology* 99, pp. 195–204.
- Roman, B., E. Hamm, and F. Melo (2013). “Forbidden Directions for the Fracture of Thin Anisotropic Sheets: An Analogy with the Wulff Plot”. In: *Physical Review Letters* 110.
- Sargado, J. M., E. Keilegavlen, I. Berre, and J. M. Nordbotten (2018). “High-accuracy phase-field models for brittle fracture based on a new family of degradation functions”. In: *Journal of the Mechanics and Physics of Solids* 111, pp. 458–489.
- Schijve, J. (2009). *Fatigue of Structures and Materials*. 2nd ed. Springer, p. 621.
- Schlüter, A., A. Willenbücher, C. Kuhn, and R. Müller (2014). “Phase field approximation of dynamic brittle fracture”. In: *Computational Mechanics* 54, pp. 1141–1161.
- Schmidt, S., W. Dornisch, and R. Müller (2017). “A phase field model for martensitic transformation coupled with the heat equation”. In: *GAMM-Mitteilungen* 40.2, pp. 138–153.
- Schreiber, C., C. Kuhn, and R. Müller (2017). “A phase field model for materials with anisotropic fracture resistance”. In: *Proceedings of the 7th GACM Colloquium*, pp. 330–334.
- Schreiber, C., C. Kuhn, and R. Müller (2019a). “On phase field modeling in the context of cyclic mechanical fatigue”. In: *PAMM* 19.1.
- Schreiber, C., C. Kuhn, and R. Müller (2019b). “Phase field modeling of cyclic fatigue crack growth under mixed mode loading”. In: *Computer Methods in Materials Science* 19, pp. 50–56.
- Schreiber, C., C. Kuhn, R. Müller, and T. Zohdi (2020a). “A phase field modeling approach of cyclic fatigue crack growth”. In: *International Journal of Fracture* 225, pp. 89–100.
- Schreiber, C., C. Kuhn, and R. Müller (2020b). “Phase field simulation of fatigue crack propagation under complex load situations”. In: *Archive of Applied Mechanics*.
- Schreiber, C., C. Kuhn, and R. Mueller (2021). “Phase field modeling of fatigue crack initiation and growth under various loading situations”. In: *PAMM* 20.1, e202000029.
- Seiler, M., T. Linse, P. Hantschke M., and Kästner (2020). “An efficient phase-field model for fatigue fracture in ductile materials”. In: 224.
- Sih, G. C. (1972). *Mechanics of Fracture*. Vol. 1. Noordhoff: Springer. Chap. Introductory Chapter, A special theory of crack propagation.

- Srawley, J. E. (1976). “Wide range stress intensity factor expressions for ASTM E 399 standard fracture toughness specimens”. In: *International Journal of Fracture* 12, pp. 475–476.
- Steinbach, I. and M. Apel (2006). “Multi phase field model for solid state transformation with elastic strain”. In: *Physica D: Nonlinear Phenomena* 217.2, pp. 153–160.
- Suresh, S. (1992). *Fatigue of materials*. 1st ed. Cambridge University Press, p. 604.
- Taylor, R. L. (2014). *FEAP - Finite Element Analysis Program*. URL: <http://www.ce.berkeley/feap>.
- Teichtmeister, S., D. Kienle, F. Aldakheel, and M.A. Keip (2017). “Phase field modeling of fracture in anisotropic brittle solids”. In: *International Journal of Non-Linear Mechanics*, pp. 100–118.
- Uematsu, Y., T. Kakiuchi, D. Ogawa, and K. Hashiba (2020). “Fatigue crack propagation near the interface between Al and steel in dissimilar Al/steel friction stir welds”. In: *International Journal of Fatigue* 138, p. 105706. ISSN: 0142-1123.
- Verhoosel, C. V. and R. de Borst (2013). “A phase-field model for cohesive fracture”. In: *International Journal for Numerical Methods in Engineering* 96.1, pp. 43–62.
- Voyiadjis, G. Z. and N. Mozaffari (2013). “Nonlocal damage model using the phase field method: Theory and applications”. In: *Computational Methodes in Applied Mechanics and Engineering* 50, pp. 3136–3151.
- Wang, F., A. Reiter, M. Kellner, J.Brillo, M Selzer, and B Nestler (2018). “Phase-field modeling of reactive wetting and growth of the intermetallic Al₂Au phase in the Al-Au system”. In: *Acta Materialia* 146, pp. 106–118.
- Wang, S.-L., R.F. Sekerka, A.A. Wheeler, B.T. Murray, S.R. Coriell, R.J. Braun, and G.B. McFadden (1993). “Thermodynamically-consistent phase-field models for solidification”. In: *Physica D: Nonlinear Phenomena* 69.1, pp. 189–200.
- Wang, Yunzhi and Ju Li (2010). “Phase field modeling of defects and deformation”. In: *Acta Materialia* 58.4, pp. 1212–1235.
- Wheeler, A.A., B.T. Murray, and R.J. Schaefer (1993). “Computation of dendrites using a phase field model”. In: *Physica D: Nonlinear Phenomena* 66.1, pp. 243–262.
- Wriggers, P. (2001). *Nichtlineare Finite-Elemente-Methoden*. 1st ed. Heidelberg: Springer, p. 465.
- Wriggers, P., F. Aldakheel, L. Lohaus, and M. Heist (2020). “Water-induced damage mechanisms of cyclically loaded High-performance concretes”. In: *Bauingenieur* 95.4, pp. 126–132.

- Wu, C. H. (1978). “Maximum-energy-release-rate criterion applied to a tension-compression specimen with crack”. In: *Journal of Elasticity* 8, pp. 235–257.
- Wöhler, A. (1866). “Über die Festigkeitsversuche mit Eisen und Stahl”. In: *Zeitschrift für Bauwesen* 16, pp. 67–84.
- Xu., B., D. Schrade, D. Gross, and R. Müller (2010). “Phase field simulation of domain structures in cracked ferroelectrics”. In: *International Journal of Fracture* 165, pp. 163–173.
- Yates, J.R., M. Zanganeh, R.A. Tomlinson, M.W. Brown, and F.A. Diaz Garrido (2008). “Crack paths under mixed mode loading”. In: *Engineering Fracture Mechanics* 75.3, pp. 319 –330.
- Zienkiewicz, O.C. and R.L. Taylor (2001). *The Finite Element Method: Its Basis and Fundamentals*. 1st ed. Butterworth-Heinemann, p. 465.
- İriç, S. and A. Ayhan (2017). “Dependence of Fracture Toughness on Rolling Direction in Aluminium 7075 Alloys”. In: *Acta Physica Polonica A* 132, pp. 892–895.

Betreute studentische Arbeiten mit Bezug zur Dissertation

- Ettrich, T. (2020). *Analyse und Validierung eines Phasenfeldmodells für anisotropes Risswachstum*. Bachelorarbeit, Technische Universität Kaiserslautern

Lebenslauf

Name: Christoph Schreiber

2000 – 2004	Realschule Oberroning
2004	Mittlere Reife
2004 – 2011	Kernkraftwerk Isar
2007	Industriemechaniker (Instandhaltung)
2011	Industriemeiter Metall
2011 – 2015	Studium Bachelor, Maschinenbau HAW Landshut
2015	Bachelor (B.Eng.)
2015 – 2016	Studium Master, Simulation und Leichtbau HAW Landshut
2016	Master (M.Eng.)
2016 – 2021	Wissenschaftlicher Mitarbeiter Lehrstuhl fr Technische Mechanik, Prof. Dr.-Ing. Ralf Mller Technische Universitt Kaiserslautern